Titre: Title:	Non-Equilibrium Germanium-Tin Microstructures for Silicon-Compatible Mid-Infrared Photonics
Auteur: Author:	Étienne Bouthillier
Date:	2019
Type:	Mémoire ou thèse / Dissertation or Thesis
Référence: Citation:	Bouthillier, É. (2019). Non-Equilibrium Germanium-Tin Microstructures for Silicon-Compatible Mid-Infrared Photonics [Mémoire de maîtrise, Polytechnique Montréal]. PolyPublie. https://publications.polymtl.ca/3867/

URL de PolyPublie: PolyPublie URL:	https://publications.polymtl.ca/3867/
Directeurs de recherche: Advisors:	Oussama Moutanabbir
Programme: Program:	Génie physique

UNIVERSITÉ DE MONTRÉAL

NON-EQUILIBRIUM GERMANIUM-TIN MICROSTRUCTURES FOR SILICON-COMPATIBLE MID-INFRARED PHOTONICS

ÉTIENNE BOUTHILLIER
DÉPARTEMENT DE GÉNIE PHYSIQUE
ÉCOLE POLYTECHNIQUE DE MONTRÉAL

MÉMOIRE PRÉSENTÉ EN VUE DE L'OBTENTION
DU DIPLÔME DE MAÎTRISE ÈS SCIENCES APPLIQUÉES
(GÉNIE PHYSIQUE)
AVRIL 2019

UNIVERSITÉ DE MONTRÉAL

ÉCOLE POLYTECHNIQUE DE MONTRÉAL

Ce mémoire intitulé :

NON-EQUILIBRIUM GERMANIUM-TIN MICROSTRUCTURES FOR SILICON-COMPATIBLE MID-INFRARED PHOTONICS

présenté par : BOUTHILLIER Étienne
en vue de l'obtention du diplôme de : Maîtrise ès sciences appliquées
a été dûment accepté par le jury d'examen constitué de :

M. PETER Yves-Alain, Dr. Sc., président
M. MOUTANABBIR Oussama, Ph. D., membre et directeur de recherche
M. SELETSKIY Denis, Ph. D., membre

ACKNOWLEDGEMENTS

J'aimerais en premier lieu formuler mes plus sincères remerciements à Oussama Moutanabbir pour m'avoir accordé sa confiance et pour avoir mis sur pied des projets d'envergure en lien avec les semiconducteurs du groupe IV. J'apprécie par dessus tout ton dynamisme, ton imagination et ton dévouement envers la recherche. Je porte en haute estime ta bonne humeur permanente et ton attitude positive lors de chacune de nos interactions. Enfin, je garde un excellent souvenir de nos discussions sur la physique des solides, mais aussi la recherche en général, et même la politique et la littérature. Ce fut un réel plaisir de travailler avec toi.

Je veux également souligner l'aide précieuse que Simone m'a apportée au quotidien, que ce soit par ses conseils en laboratoire ou son partage des rouages du milieu de la recherche universitaire. De plus, ce travail n'aurait pu être possible sans une contribution majeure de sa part, soit la croissance des échantillons de GeSn. *Hero samples from a hero grower!*

D'ailleurs, les projets au sein du groupe ont grandement bénéficié de la collaboration de toute l'équipe. Je tiens à remercier tous les membres pour leur implication. Plus particulièrement, je suis reconnaissant envers Jérôme, pour ses centaines de mesures de diffraction aux rayons X, Anis, pour les analyses à l'ellipsomètre, et Alain Dijkstra, pour les mesures de photoluminescence, qui ont chacun fourni des données présentées dans ce mémoire.

En outre, je souhaite témoigner ma reconnaissance envers les membres des organisations suivantes qui ont rendu possible l'utilisation de tous ces équipements scientifiques: Marie-Hélène et Christophe du Laboratoire de microfabrication; Bill du Laboratoire des Revêtements Fonctionnels et d'Ingénierie de Surfaces, Samir du Laboratoire de caractérisation des matériaux; ainsi que Boris et Fabien du Laboratoire de micro et nanofabrication de l'Institut national de la recherche scientifique à Varennes.

Je voudrais aussi souligner l'importante contribution des organismes subventionnaires qui ont permis la réalisation de ce projet: le Conseil de recherches en sciences naturelles et en génie du Canada, le Fonds de recherche du Québec – Nature et technologies, l'Institut de l'énergie Trottier ainsi qu'Hydro-Québec. Votre soutien financier fait une réelle différence.

Je remercie également les membres du jury pour leur temps et leurs conseils suite à la lecture de ce mémoire. Merci aux membres du laboratoire ainsi qu'à mes amis de Génie physique pour les invitations à dîner renouvelées et pour toutes ces discussions, scientifiques ou non!

Enfin, je veux remercier mes parents pour leur soutien indéfectible. Vous jouez un rôle important dans toutes mes réussites. À Catherine, merci pour tout!

RÉSUMÉ

Le développement rapide de l'informatique et des technologies de la communication a eu un impact majeur sur l'économie et la société en général. Il n'a jamais été aussi facile d'échanger un message ou de discuter avec un proche habitant de l'autre côté de la planète. De plus, les nouveaux outils technologiques bousculent l'organisation du travail et ceux-ci sont à l'origine de ce qu'on a appelé la quatrième révolution industrielle, ou l'industrie 4.0. Toutefois, la croissance exponentielle du trafic Internet est la source de sérieux enjeux au niveau énergétique. En effet, la demande d'électricité liée au secteur des technologies de l'information et de la communication représentera à elle seule 21 % de la demande au niveau mondial en 2025. Pour remédier à ce problème et réduire l'impact environnemental des centres de données, la photonique intégrée sur silicium représente une solution prometteuse. En effet, contrairement au mouvement des électrons impliquant l'effet Joule, le déplacement de photons ne génère pas de chaleur. Or, le silicium qui est à la base de toute l'électronique moderne ne possède pas de bande interdite directe, le rendant inefficace pour absorber ou émettre de la lumière. En raison de leur bande interdite directe, les alliages semiconducteurs du groupe IV tels que le germanium-étain (GeSn) sont le sujet d'un vif intérêt scientifique pour relever le défi de l'intégration de circuits photoniques sur une plateforme de silicium. Le GeSn devient un semiconducteur à bande interdite directe pour des concentrations d'étain supérieures à 10 at.%, mais cette valeur est plus élevée lorsque le matériau est soumis à une contrainte en compression.

Étant donné le rôle central que jouent la contrainte et la composition chimique au niveau de la structure de bande du GeSn, il importe de mesurer ces paramètres avec précision au niveau micrométrique. Pour cette raison, une étude de spectroscopie Raman détaillée a été menée. L'utilisation d'un laser avec une longueur d'onde de 633 nm a permis d'identifier les modes Ge-Ge, Ge-Sn, "Sn-Sn like" ainsi qu'un mode supplémentaire activé par le désordre. En analysant quatorze échantillons crûs par dépôt chimique en phase vapeur et présentant une large gamme de concentrations et de contraintes, il a été possible d'isoler l'impact de ces deux paramètres sur l'énergie des modes de vibration Raman. Notamment, le nombre d'onde des quatre modes diminue pour des concentrations croissantes ou des contraintes en compression moindres. De plus, le mode Ge-Ge devient plus asymétrique pour des teneurs en étain plus élevées, alors que la contrainte n'a pas d'effet notable. Ces observations ont permis d'élaborer un modèle pour extraire la concentration en étain et la contrainte de couches ou de microstructures de GeSn à partir d'un unique spectre Raman.

En raison de sa bande interdite directe, dont la valeur peut être modifiée selon la concentration en étain, le GeSn est un candidat prometteur pour le développement de photodétecteurs. Par contre, l'efficacité de dispositifs de type planaires est limitée par la grande réflectance à l'interface air-semiconducteur ($\approx 40\,\%$). En utilisant des calculs par différences finies dans le domaine temporel, nous avons montré que la fabrication de nanopiliers de GeSn permet d'augmenter significativement le couplage dans la couche active du dispositif. En effet, des piliers d'une hauteur supérieure à 1 µm et distants de ≈ 1 µm ont un facteur d'absorption deux fois plus grand que les couches de GeSn à 10 at.% et 14 at.% d'étain desquelles ils proviennent. Ceci s'explique par l'importante réduction de la réflexion à la première interface, qui est valide pour des combinaisons spécifiques de diamètres et de longueurs d'onde. Ainsi, le facteur d'absorption spectral peut être modifié en variant la largeur des piliers. La performance des réseaux de nanopiliers a aussi été étudiée selon l'angle d'incidence. Le couplage s'avère meilleur pour la polarisation s que pour la polarisation p, alors que le comportement opposé est observé pour la géométrie planaire. Des réseaux de nanopiliers ont été fabriqués dans un échantillon de GeSn par lithographie à faisceau d'électrons et par gravure sèche dans un plasma de Cl_2. La couche de 1.1 µm de GeSn à 9 at.% d'étain a été crûe sur une couche de germanium, elle-même déposée sur une tranche de silicium polie sur les deux faces. La caractérisation au spectrophotomètre a permis de vérifier expérimentalement que le facteur d'absorption des nanopiliers est le double de celui de la couche mince dans l'infrarouge court.

Enfin, des microdisques de GeSn ont également été fabriqués selon un procédé similaire, auquel s'est ajouté une étape de gravure sèche dans un plasma de CF_4. Grâce à la méthode de mesure basée sur la spectroscopie Raman développée plus tôt, des relâchements de la contrainte de $-0.33\,\%$ à $0.05\,\%$ et de $-1.27\,\%$ à $-0.15\,\%$ ont été mesurés pour des couches de GeSn à 13.3 at.% et 16.9 at.% d'étain, respectivement. Le rétrécissement de la bande interdite associé à un relâchement de la contrainte en compression a été confirmé par des mesures de photoluminescence. Les pics d'émission ont été déplacés de 3.2 µm à 3.6 µm et de 3.3 µm à 4.0 µm, ce qui représente l'émission à la plus longue longueur d'onde observée à ce jour pour le GeSn.

L'ensemble des résultats obtenus à travers ce projet démontre la pertinence des alliages de GeSn pour la photonique intégrée sur silicium et prépare le terrain pour intégrer les microstructures de GeSn dans des dispositifs opérant dans le moyen infrarouge.

ABSTRACT

The relentless development of the information and communications technology (ICT) has had considerable and profoundly transformative economic and social impacts. The exponential growth of internet traffic now represents a major issue due to the immense power consumption and carbon footprint of data centers around the world. Indeed, it is estimated that this sector will be responsible for 21 % of the global electrical demand in 2025. To overcome this important challenge and reduce the environmental burden of ICT, integrated silicon photonics has emerged as a key solution to decrease the power consumption of electronic devices, since the generation of heat due to the motion of electrons in wires doesn't apply to photons. However, silicon, which is at the core of all modern electronics, is not an effective material for light emission and absorption due to its indirect band gap. In this regard, group IV alloys such as germanium-tin (GeSn) have attracted a great deal of interest as direct band gap materials compatible with silicon platforms. An indirect to direct band gap transition occurs when Sn is incorporated in Ge at concentrations above 10 at.%. This threshold increases (drops) as the compressive (tensile) strain in the lattice increases.

Given the fundamental role of strain and composition on the GeSn band structure, the reliable, non-destructive characterization of these two parameters down to the nanoscale is of paramount importance. With this perspective, a detailed Raman spectroscopy study was conducted using a 633 nm laser, allowing a clear identification of the Ge-Ge, Ge-Sn, Sn-Sn like modes, as well as an additional disorder-activated mode. Samples with various degrees of strain and composition were investigated, thus enabling the decoupling of these two contributions in Raman spectra. It was found that the four modes all downshift as Sn content increases and compressive strain relaxes. The Ge-Ge mode also becomes more asymmetric for higher Sn contents, while strain has no noticeable impact on the mode symmetry. Based on these observations, a model is presented to extract Sn composition and strain for GeSn layers and structures from a single Raman spectrum.

While GeSn is regarded as a promising material for light detection, standard planar photodetectors suffer from important reflection at the first interface which limits their performance. Using finite-difference time-domain simulations, the structuring of GeSn layers into nanopillars was confirmed as an effective technique to improve the coupling into the active material. The results show a two-fold increase of the absorptance when 10 at.% and 14 at.% GeSn layers are structured into ≥ 1 µm-high nanopillars spaced ≈ 1 µm apart. The enhanced absorptance results from a reduction of the ≈ 40 % reflectance normally associated to bulk,

and is valid for specific combinations of diameters and wavelengths. This means the spectral absorptance can be tuned by varying the pillar diameters. Moreover, the evaluation of angular performance showed that *s*-polarized light better couples to the nanopillar arrays than *p*-polarized light, while the opposite is observed for bulk. Such nanopillars were fabricated using electron-beam lithography followed by a Cl_2-based plasma etching. Pillars were structured in 1.1 µm-thick 9 at.% GeSn grown on a germanium virtual substrate on a double side polished silicon wafer. The two-fold increase in absorptance was experimentally verified for wavelengths in the short-wave infrared range.

Furthermore, arrays of GeSn microdisks were also fabricated via the addition of a second etching step to the process, based on a CF_4 plasma. The Raman model developed earlier confirmed the strain relaxation from $-0.33\,\%$ to $0.05\,\%$ for a 13.3 at.% GeSn top layer and from $-1.27\,\%$ to $-0.15\,\%$ for a 16.9 at.% layer. The narrower band gap associated to lower compressive strain was established by a shift of the photoluminescence peak from 3.2 µm to 3.6 µm and from 3.3 µm to 4.0 µm respectively, thus achieving the longest emission from GeSn reported so far.

The results in this thesis highlight the potential of GeSn as a powerful material system for silicon-compatible photonics and pave the way to its introduction in design and development of mid-infrared devices.

TABLE OF CONTENTS

LIST OF TABLES

LIST OF FIGURES

LIST OF SYMBOLS AND ACRONYMS

APT	Atom probe tomography
BCB	Benzocyclobutene
BFAST	Broadband fixed angle source technique
BL	Bottom layer
CMOS	Complementary metal–oxide–semiconductor
CVD	Chemical vapor deposition
DA	Disorder-activated
EBL	Electron-beam lithography
EMG	Exponentially modified gaussian
FDTD	Finite-difference time-domain
FET	Field-effect transistor
FWHM	Full width at half maximum
Ge	Germanium
HWP	Half-wave plate
ICP	Inductively coupled plasma
ICT	Information and communication technology
ITO	Indium tin oxide
LA	Longitudinal acoustical
LED	Light-emitting diode
LO	Longitudinal optical
MBE	Molecular-beam epitaxy
MIR	Mid-infrared
ML	Middle layer
MQW	Multi-quantum well
NW	Nanowire
PML	Perfectly matched layer
PL	Photoluminescence
PVD	Physical vapor deposition
RIE	Reactive ion etching
SEM	Scanning electron microscope
Si	Silicon
Sn	Tin
SRB	Strain relaxed buffer

STEM	Scanning transmission electron microscope
SWIR	Short-wavelength infrared
TA	Transverse acoustical
TEM	Transmission electron microscope
TEOS	Tetraethylorthosilicate
TL	Top layer
TO	Transverse optical
VCA	Virtual crystal approximation
VLS	Vapor-liquid-solid
VS	Virtual substrate
XRD	X-ray diffraction

LIST OF APPENDICES

CHAPTER 1 INTRODUCTION

1.1 Context

Internet of things, cloud computing, augmented reality, cryptocurrencies, 5G networks: all these emerging technologies and platforms encourage the transfer of large amounts of data over the Web, adding up to the already widespread use of internet. Sensors in industrial machines, robots, cars, cameras for home security, individuals browsing or watching videos on their mobiles, tablets and virtual reality headsets; all are connected more and more and contribute to the exponential growth of global internet traffic, which is expected to increase from 1.5 ZB/year in 2017 to 4.8 ZB/year in 2022 [1] [1].

The development of faster and smaller devices has enabled great advances in telecommunications and information technology. Calling family members across the country or sending a document to the other side of the world have never been simpler. Easier and improved communications is sometimes put forward as a solution to reduce greenhouse gas emissions [2]. For instance, videoconferencing and telecommuting could lead to fewer travels, and efficiency of industrial processes could be optimized by the real-time monitoring of operations. However, it is also the source of a major issue as the transfer and storage of data online has considerable energetic costs. Energy demand of data centers in the United States alone is estimated to 91 TWh for 2013, and this figure will grow to approximately 140 TWh in 2020 [3]. This is equivalent to the annual output of 50 large coal thermal power stations. As a reference, the total electricity consumption in Québec in 2013 was 172.5 TWh [4]. Worldwide, electricity usage of data centers is expected to go from 203 TWh in 2015 to 3390 TWh in 2025, which is more than half of the 5860 TWh expected for all of the information and communication technology (ICT) sector [5]. ICT would then be responsible of 21% of the total electricity consumption, compared to 8% 10 years before. This is a serious concern, especially considering that non-renewable energy sources still generate 75% of the electricity around the world [6], and would therefore result in an increasing pressure to extract more natural resources.

Given the staggering energy burden of data centers (an estimated 12% of the world total in 2025 [5]), sustaining the exponential increase in energy demands is not viable. Additionally, there are no signs that the internet traffic growth will slow down any time soon. The challenge therefore lies in improving and developing energy-efficient electronic devices used in the

[1] $1\,\mathrm{ZB} = 1 \times 10^{21}\mathrm{bytes}$

telecommunications industry. Current flowing in copper wires or silicon chips generates heat, as a consequence to the Joule effect. Almost all of the electricity consumed by data centers is wasted as heat in electronic devices or used in cooling systems to keep their temperature at an acceptable level. There are initiatives to harness the thermal energy and convert it into electricity again, yet reducing energy consumption at the source is another challenge which has to be tackled simultaneously.

A promising avenue is integrated photonics, where photons are used to convey information instead of electrons. While sources and detectors would still require electrical power, photons interact less and thus their propagation doesn't generate significant heat. In fact, transmission of information with photons has been used for years, as optical fibers were laid in the bottom of oceans since the mid-90s for intercontinental communications [7] and now spread across every major city. The paradigm here is to bring these advantages to progressively shorter distances, as illustrated in figure 1.1, until eventually chip-to-chip and intra-chip communications are achieved by photons. This requires the implementation of photonics at the chip-level, and the co-development of photonic and electronic devices.

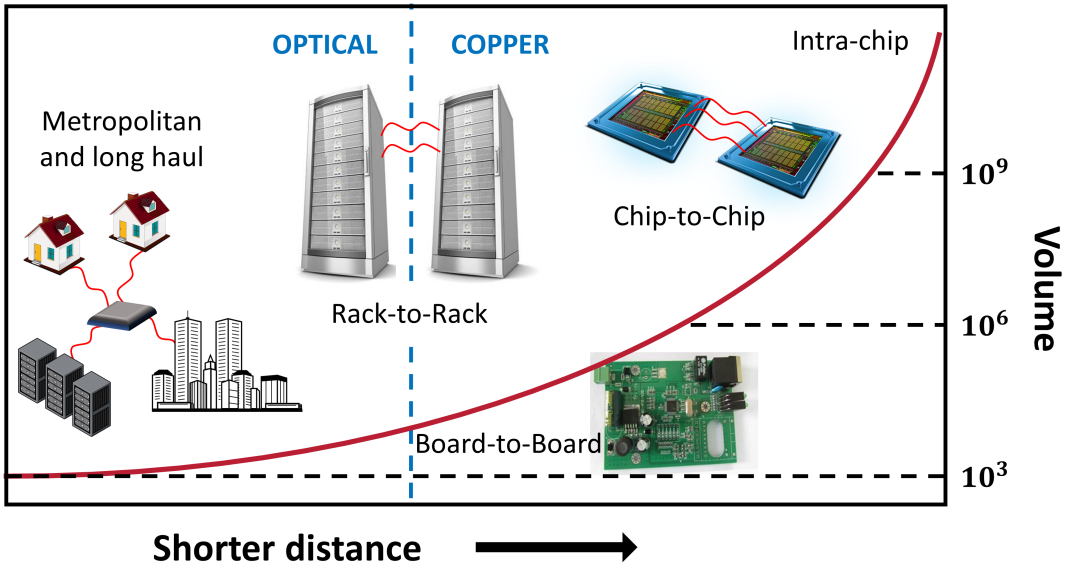

Figure 1.1 Types of interconnects in telecommunication networks

1.2 Silicon photonics

The microelectronics industry has shown a strong interest for developing optical interconnects because of their lower losses and lower dispersion, which allow faster data transmission, as well as reduced interchannel crosstalk and electromagnetic interference [8]. The realization

of optical communication at the chip-scale requires a strong level of integration and high production volumes, also highlighted in figure 1.1. This means that the fabrication of photonic devices needs to be compatible with the silicon microfabrication infrastructure and, ideally, CMOS technology. CMOS stands for *complementary metal–oxide–semiconductor* and designates the mass-production processes used nowadays to fabricate integrated circuits at the core of microprocessors, memories, etc. An example of photonic and electronic circuits integration, realized by Atabaki *et al.*, is depicted on figure 1.2. In this case, passive and active photonic components (waveguides, microring resonators, vertical grating couplers, high-speed modulators, and avalanche photodetectors) were fabricated next to the digital circuits on industry standard 300 mm wafers.

The realization of photonic circuits requires the assembly of components which are already available for the most part: waveguides, filters, multiplexers and demultiplexers, power splitters, modulators, and photodetectors [10]. Detectors can be fabricated by the hetero-epitaxy

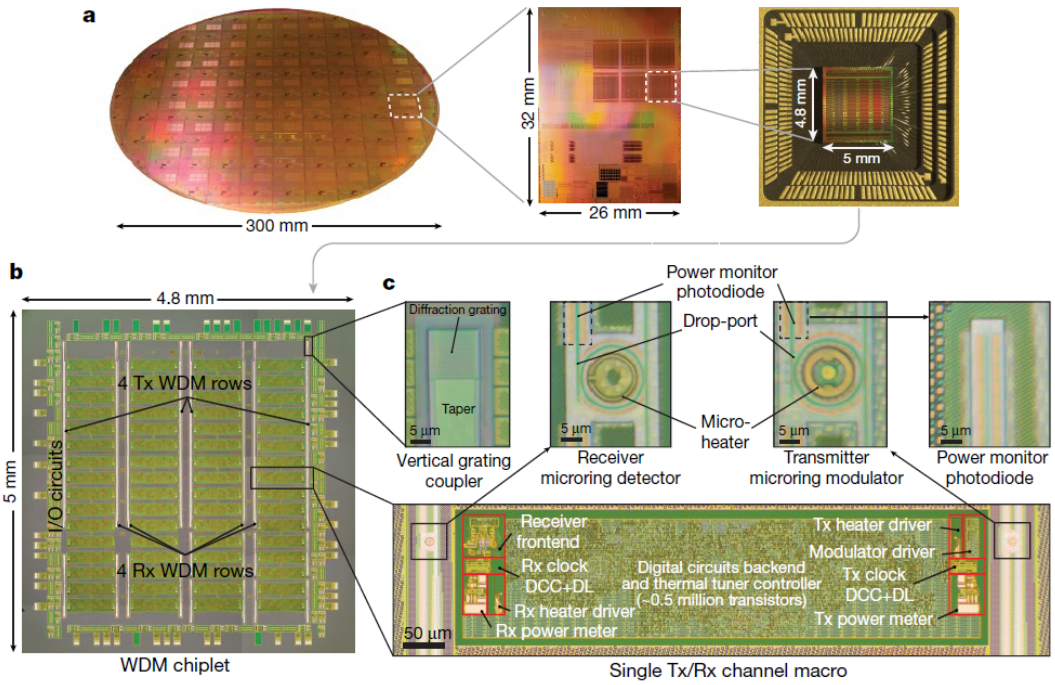

Figure 1.2 Photonic and electronic circuits fabricated on a 300 mm wafer and zoomed-in images for one die [9]. Reprinted by permission from Springer Nature Customer Service Centre GmbH: Springer Nature, Integrating photonics with silicon nanoelectronics for the next generation of systems on a chip, Amir H. Atabaki, Sajjad Moazeni, Fabio Pavanello, Hayk Gevorgyan, Jelena Notaros, Luca Alloatti, Mark T. Wade, Chen Sun, Seth A. Kruger, Huaiyu Meng, Kenaish Al Qubaisi, Imbert Wang, Bohan Zhang, Anatol Khilo, Christopher V. Baiocco, Miloš A. Popović, Vladimir M. Stojanović and Rajeev J. Ram, Copyright (2018).

of germanium over silicon, which share similar chemical properties. However, a remaining challenge is the lack of a monolithic, electrically-pumped light source fully compatible with silicon. The development of these monolithic light sources has been limited by the indirect band gap of silicon and germanium, as emission and absorption phenomena are less favorable than in direct band gap semiconductors. On the other hand, III-V semiconductors such as GaAs, InP, or GaN (formed by elements of the third and fifth columns of the periodic table) have a direct band gap. Extensive research in the last decades has led to the development of high-gain lasers, high-speed and efficient photodetectors [10]. The sources are integrated on the silicon platform via wafer bonding or butt-coupling. However, since attaching optical fibers on every device is not time- nor cost-effective, the cost of silicon photonic devices becomes dominated by packaging. Furthermore, III-V wafers are more expensive and not available in diameters as large as their silicon counterparts. It is desirable to limit packaging steps and increase the fabrication yield by achieving monolithic integration of all photonic components on a single chip. This is also mandatory for optical communication at the chip-to-chip level. In this regard, an important limitation of III-V semiconductors is their challenging growth on silicon platforms.

Best candidates for the direct growth on silicon are group IV semiconductors, which form covalent bonds and share similar chemical and physical properties. While silicon (Si) and germanium (Ge) are indirect semiconductors, alloying Ge with tin (Sn) (with the possible addition of Si) can lead to direct band gap semiconductors. This potential has motivated tremendous efforts to develop, functionalize, and integrate all-group IV photonic devices.

The development of group IV semiconductors is also of interest for other applications. An important characteristic is their wide spectral tunability from visible to terahertz radiations. Devices sensible to photons in the short-wavelength infrared (SWIR) and mid-infrared (MIR) are relevant for night-vision imaging and astronomy. They are also promising for spectroscopy and sensing applications, since absorption bands of many organic molecules and gases are included in this range [11,12]. Furthermore, band gap tunability is beneficial to photovoltaics. High-efficiency solar cells on the market are formed of InGaP/InGaAs/Ge multijonctions. It is suggested the addition of a SiGeSn fourth junction can further increase the efficiency [13] by absorbing a part of the solar spectrum which is not exploited otherwise. Knowledge acquired in growth and characterization of group IV alloys will be applicable to this field. Finally, GeSn is also studied to increase carrier mobility in field-effect transistors (FET), either as the channel material or as a stressor for Ge channels [14–17].

1.3 Research objectives

The objective of the current work is to facilitate the development of GeSn technologies by establishing a deeper understanding of the basic structural and optical properties of epitaxial layers and structures. The following scientific questions are addressed: (1) Is it possible to employ Raman spectroscopy to decouple the effects of strain and composition on GeSn vibrational modes?; (2) Can light absorption be engineered by structuring GeSn layers?; (3) What are the microfabrication processes to control GeSn patterning and structuring?; and (4) How can light emission from GeSn be achieved at longer wavelengths? The answers to these questions will establish a clear understanding of the behavior of GeSn layers, structures and devices as a function of Sn content and strain. To tackle them, this work is organized around the following main objectives:

(1) Develop a Raman spectroscopy framework to extract Sn content and strain from GeSn layers and structures down to the micro-scale;
(2) Demonstrate the relevance of top-down nanopillars to enhance and control the absorption of infrared radiation by GeSn structures;
(3) Fabricate GeSn nanopillar arrays with favorable optical properties;
(4) Demonstrate MIR light emission from underetched GeSn microdisks.

1.4 Thesis outline

This thesis is organized in seven chapters. The next chapter gives an overview of the current literature on group IV photonics, with a focus on GeSn. Chapter 3 presents the mathematical methods used to predict the properties of GeSn structures, as well as experimental methods used to fabricate and characterize them. Theoretical explanations are given along with experimental details. The main results and findings are the subject of the following three chapters. Chapter 4 presents detailed analyses of GeSn vibrational modes using Raman spectroscopy. This allowed to develop an approach to retrieve Sn content and strain of a GeSn layer from its Raman spectrum. Next, simulations of optical properties for GeSn structures are included in chapter 5. The fabrication and characterization of GeSn nanopillars and microdisks are presented in chapter 6. Chapter 7 summarizes the work and discusses research perspectives. Finally, a list of contributions is included in Appendix A.

CHAPTER 2 LITERATURE REVIEW

2.1 GeSn as a direct band gap semiconductor

Sn-containing group IV semiconductors have been attracting a great deal of interest as a versatile, silicon-compatible photonic platform. This enthusiasm notably relies on the possibility to tune the band gap by alloying Ge with Sn: first, to achieve direct gap, and second, to cover a wide range of energies in SWIR and MIR. The addition of Si provides an additional degree of freedom, allowing the independent control of band gap energy and lattice constant, an important feature normally associated to the more mature III-V semiconductors.

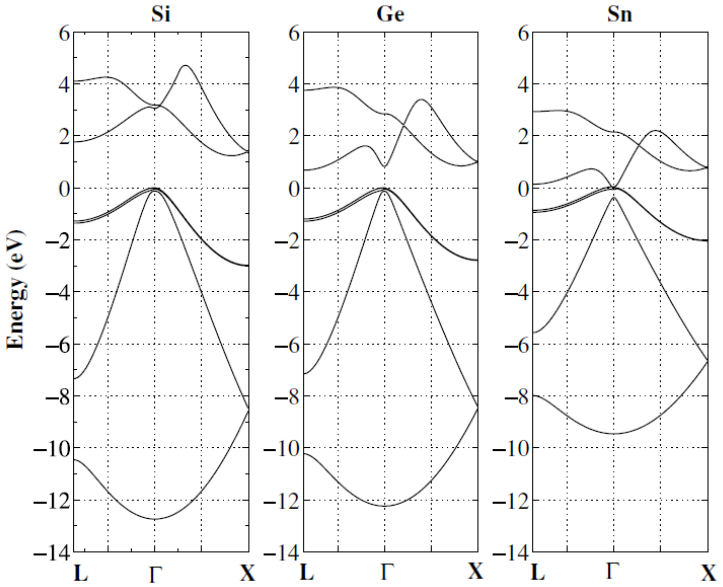

Figure 2.1 Calculated electronic band structures of group IV materials Si, Ge, and α-Sn[1] [18]. https://doi.org/10.1088/0268-1242/22/7/012

Si and Ge are indirect band gap semiconductors, as illustrated in figure 2.1. The valence band maximum is located at the Γ point, whereas the conduction band reaches its minimum at the X (for Si) or L (for Ge) points. Sn[1], on the other hand, is a semimetal, with no band gap at the Γ point.

[1]Sn has two main allotropes. The α phase, or gray tin, stable at temperatures below 13 °C [19], is a diamond-cubic crystal, and the β phase, or white tin, stable at room temperature, is tetragonal. In this document, Sn always refer to α-Sn, because group IV alloys under study follow the structure of predominant Ge, which is a diamond-cubic crystal.

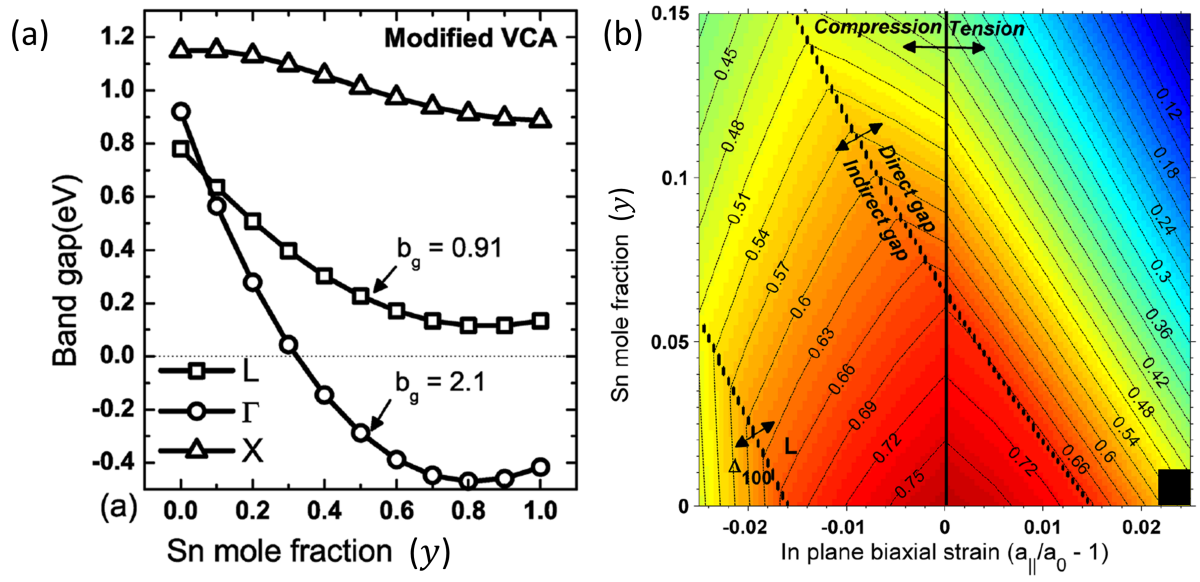

Figure 2.2 Sn incorporation in Ge to achieve a direct band gap [20]. (a) Energies of conduction band minima for high symmetry points. b_g is the band gap bowing parameter (see reference [20]). (b) Combined effect of Sn incorporation and strain on the smallest gap formed by valleys Γ, L or Δ_{100} (values in eV). Reprinted from S. Gupta, B. Magyari-Köpe, Y. Nishi, and K. C. Saraswat, "Achieving direct band gap in germanium through integration of Sn alloying and external strain," *Journal of Applied Physics*, vol. 113, no. 7, 2013., with the permission of AIP Publishing.

The incorporation of Sn in a Ge lattice lowers the conduction bands minima. However, Sn effect is more pronounced for the Γ valley than for the L valley, as shown in figure 2.2(a), meaning a direct band gap semiconductor is obtained for higher Sn contents (y). The possibility of a direct gap in $Ge_{1-y}Sn_y$ was first proposed in 1982 [19]. Few years later, Jenkins and Dow predicted the Γ and L valleys crossover at a Sn content of $y = 20$ at.% [21]. Their numerical method was based on the virtual crystal approximation (VCA), where the crystal is assumed to be formed by atoms with properties linearly interpolated from the alloy's constituent elements. In 1989, Mäder *et al.* found 26 at.% [22] by correcting energy gaps obtained by the VCA to fit empirical data. More recent investigations suggested the transition occurred at lower contents of Sn. In 2007, Moontragoon *et al.* found 17 at.% [18] using a mixed-atom method, for which calculations are performed over a supercell containing the right proportions of each atom. A crossover as low as 6 at.% was estimated from calculations based on density-functional theory [23] and modified VCA [20].

These numbers are valid for an unstrained crystal; however, achieving this experimentally is not trivial. Given the larger lattice constant of Sn (6.489 Å) compared to that of Ge (5.657 Å) [24], the growth of GeSn on Ge results in compressive strain in the layer, for which

the actual in-place lattice constant $a_{\parallel}$ is smaller than that at equilibrium a_0. An increase in compressive strain means a greater Sn incorporation is required to achieve a direct band gap, as shown in figure 2.2(b). This graph also highlights the possibility of direct band gap emission in pure Ge ($y = 0\,\text{at.}\%$) by applying $1.5\,\% - 2.0\,\%$ tensile strain. This explains why strained-Ge is also investigated for a Si-compatible semiconductor laser [25, 26].

In 2014, Attiaoui and Moutanabbir extended this kind of analysis to strained and relaxed $Si_xGe_{1-x-y}Sn_y$ using a second nearest neighbors tight binding approach [27]. They found that a direct gap is obtained for $y > 1.364x + 0.107$, where x represents the Si content. The additional degree of freedom in ternary alloys is relevant for the independent control of strain and band gap.

To summarize, growing GeSn and SiGeSn with higher Sn contents and lower compressive strains are beneficial to achieve a direct gap. These are two important challenges tackled by research in group IV epitaxy.

2.2 Growth of supersaturated GeSn alloys

In reality, the incorporation of Sn atoms at concentrations relevant for technological applications represents a major issue in GeSn epitaxy, since the equilibrium solubility of Sn in Ge is as low as 1 at.% [28], as shown in figure 2.3. In Si, Sn solubility is even smaller, reaching $y \leq 0.1\,\text{at.}\%$ [29]. GeSn and SiGeSn with $y > 1\,\text{at.}\%$ can be grown via non-equilibrium processes, but preventing Sn segregation in these metastable alloys is a challenge [30, 31].

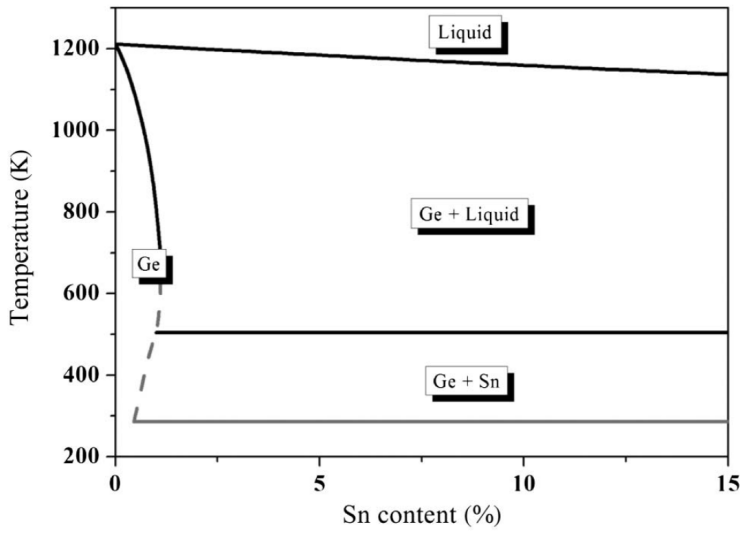

Figure 2.3 Ge-Sn phase diagram. Reprinted with permission from [28], Photonics Research.

Following the prediction of direct-gap GeSn in 1982, microcrystalline GeSn films were produced by pulsed UV laser crystallization [32], while monocrystalline layers with $y \leq 8\,\text{at.}\%$ were obtained in 1987 by sputtering [33].

Early developments of monocrystalline GeSn layers were mostly performed using physical vapor deposition (PVD) methods, including molecular-beam epitaxy (MBE) [13, 34, 35]. Compared to PVD, the development of new processes is often more complex in chemical vapor deposition (CVD) systems. On the other hand, CVD offers higher growth rates, uniform deposition over large wafers, as well as possibility of selective growth [36]. These advantages make this technique more suitable for cost-effective, scalable fabrication. However, CVD was not employed for GeSn growth before the beginning of this century due to the lack of a suitable Sn precursor. The first demonstration was achieved in 2001 using $C_6H_5SnD_3$ and Ge_2H_6 [37]. The availability of commercial tin tetrachloride ($SnCl_4$) precursor, along with either monogermane (GeH_4) [38–41] or digermane (Ge_2H_6) [14, 31, 42–44] has revived the interest in this material system in the last decade.

There is currently a world-wide race to achieve and control the growth of high crystalline quality GeSn layers and heterostructures compatible with the Si microelectronics infrastructure. Therefore, Si wafers are commonly used as starting substrates for the CVD growth of GeSn alloys. The much higher cost of Ge wafers (more than ten times) prevents their use for the development of GeSn growth processes in both industrial and academic contexts. In addition, growing GeSn on Si wafers ensures the scalability of this technology, since it is the second most abundant element in the Earth's crust. However, the direct growth of GeSn on Si is challenging because of the large lattice mismatch. Indeed, the lattice constant of Si ($a^{Si} = 5.431\,\text{Å}$) is much smaller than that of GeSn, which is between those of Ge ($a_0^{Ge} = 5.657\,\text{Å}$) and Sn ($a_0^{Sn} = 6.489\,\text{Å}$) [24] and can be interpolated using

$$a_0^{GeSn} = a_0^{Ge}\,(1-y) + a_0^{Sn} y + b^{GeSn} y\,(1-y) \tag{2.1}$$

The bowing parameter b^{GeSn} is introduced to account for deviations from the linear behavior (Vegard's law). Through the years, values of $0.65\,\text{Å}$ [45], $0.0468\,\text{Å}$ [46], $0.008\,82\,\text{Å}$ [47], $0.041\,\text{Å}$ [48] and even zero [24] were suggested for b^{GeSn}.

The introduction of a Ge virtual substrate (Ge-VS), also called strain relaxed buffer (SRB), alleviates the challenge posed by the lattice mismatch, since Ge has an intermediate lattice constant. These were notably developped by Hartmann *et al.* [49–52]. After annealing the Si wafer at a high temperature ($T > 900\,°\text{C}$), the Ge-VS growth is achieved by the decomposition of Ge precursors on the sample, kept at a temperature in the order of $400\,°\text{C} - 600\,°\text{C}$. The quality of the VS can be improved by subsequent thermal cycling in the $750\,°\text{C} -$

890 °C range [51]. Next, the GeSn layer is grown by simultaneously introducing the Sn and Ge precursors in the chamber. Sn incorporation is favored by decreasing the temperature (around 290 °C - 330 °C) and increasing the $SnCl_4$ flow [44]. When the thickness surpasses a certain critial value, strain is released via the formation of misfit dislocations (creating plastic relaxation). Thicker layers result in greater relaxation.

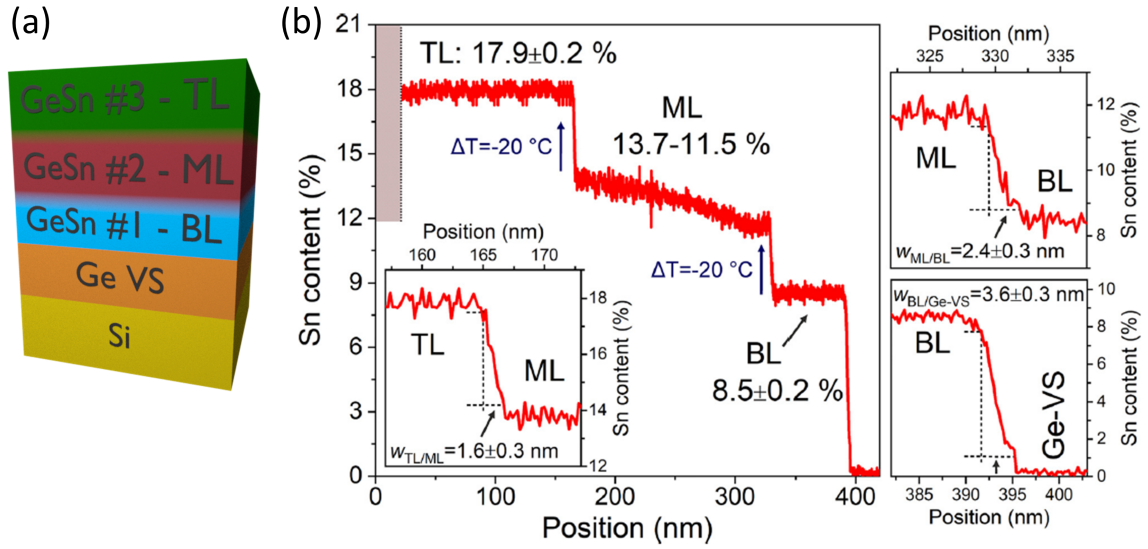

Figure 2.4 GeSn growth on buffer layers. (a) Stacking schematic for the Si substrate, Ge-VS, GeSn bottom layer (BL), middle layer (ML), and top layer (TL). (b) Composition profile measured via atom probe tomography [40]. Reprinted from S. Assali, J. Nicolas, S. Mukherjee, A. Dijkstra, and O. Moutanabbir, "Atomically uniform Sn-rich GeSn semiconductors with 3.0–3.5 µm room-temperature optical emission," *Applied Physics Letters*, vol. 112, no. 25, p. 251903, jun 2018. [Online]. Available: `http://aip.scitation.org/doi/10.1063/1.5038644`, with the permission of AIP Publishing.

Additional GeSn layers with intermediate compositions can be used to progressively expand the starting lattice constant of the next layer. An example of a multi-layer stacking is exhibited in figure 2.4. This has proven to be a successful strategy to achieve higher levels of Sn content [40, 43, 53, 54]. Films with $y \geq 16$ at.% were grown using this technique, which is the current state of the art for CVD-grown GeSn [40, 43, 54–56]. In fact, the relaxation of strain via the formation of dislocations, in combination with a lower growth temperature, were found to be crucial factors to achieve high levels of Sn incorporation [41]. This means that while control over Sn content and strain are the key to tune the band gap, they are not independent. As a matter of fact, the lattice constant depends on the Sn content, and the relaxation is a driving force for Sn incorporation. Furthermore, the introduction of buffer layers to control the strain is beneficial to prevent Sn segregation at the surface. This is highly

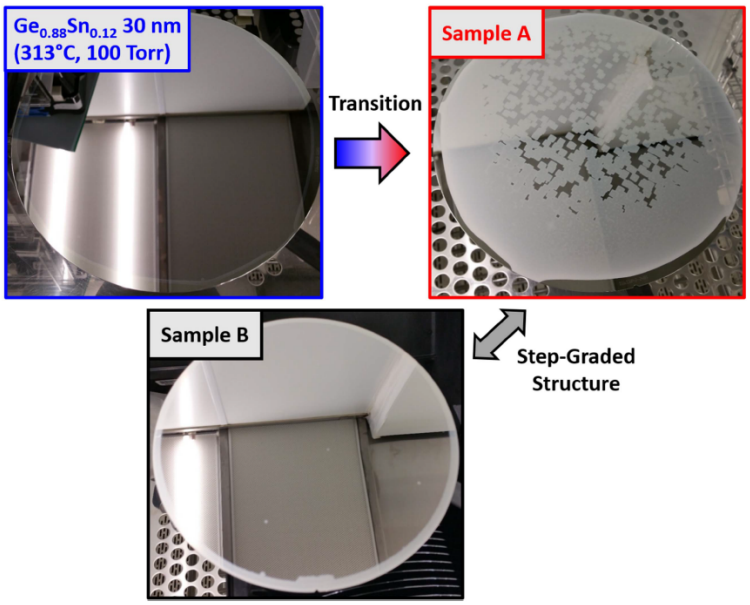

Figure 2.5 Sn segregation during the growth of GeSn layers. Pictures of 200 nm wafers with pseudomorphic (top-left) and thick (top-right) GeSn layers with $y = 12$ at.%. The addition of a step-graded structure eliminates most of the Sn segregation (bottom) [43]. https://doi.org/10.1088/1361-6641/aa8084

undesirable, since it results in the depletion of the GeSn layer back to the equilibrium content. This is accompanied by a significant increase of surface roughness, visible in figure 2.5.

To achieve optical emission or absorption at longer wavelengths, figure 2.2(b) suggests strain relaxation has similar results as Sn incorporation. One solution could then be the growth of a thick top layer (TL) above GeSn buffers to allow for relaxation. Another efficient way to release the strain is via removing the Ge-VS template altogether. In fact, the formation of GeSn membranes can be achieved by underetching [57] using conventional dry etching techniques [58, 59]. Releasing the strain to achieve emission at longer wavelengths will be the subject of section 6.2. In addition, it is possible to further reduce the band gap energy by applying tensile strain, for instance by the deposition of a silicon nitride stressor [60].

2.3 Optoelectronic devices

The CVD growth of high quality SiGeSn and GeSn structures creates new opportunities to develop group IV optoelectronic devices. In fact, direct band gap emission was demonstrated for Sn contents of 12.6 at.% [61], and the current state-of-the-art ($y \geq 16$ at.%) is sufficient to achieve direct band gap emission above 3 µm [40]. In addition to the growth of low-defect

layers, notable challenges facing the development of GeSn devices are controlling the doping level [62,63], optimizing microfabrication processes [58,59], and establishing the appropriate electric contacts [64], to name a few.

2.3.1 Light sources

Lasers

An important aspiration for group IV alloys is the fabrication of Si-compatible lasers. Theoretical studies focused on properties of GeSn as gain medium [65,66], including the design of an electrically pumped GeSn laser suggested in 2010 [67,68]. In these studies, SiGeSn was often investigated for barriers due to its higher gap [27]. However, most parameters needed for the calculations (effective masses, band gaps, deformation potentials, elastic constants, etc.) were simply interpolated from those of Si, Ge, and Sn constituents, meaning the predicted properties can vary significantly from those of experimental measurements.

One significant achievement in the field was the demonstration by Wirths *et al.* in early 2015 of lasing at 90 K from direct band gap GeSn grown on Si [61]. The sample consisted of a 560 nm-thick GeSn layer with $y = 12.6$ at.% Sn grown on a Ge-VS on a Si(100) substrate and patterned into a 5 µm-wide and 1 mm-long Fabry–Perot cavity. The device was optically pumped and the emission peak was at a wavelength of 2.22 µm.

Since then, the focus has been on achieving lasing at higher temperatures with the ultimate goal of reaching room-temperature operation. In 2016, the same group obtained lasing at both higher wavelength (≈ 2.5 µm) and temperature (130 K) using microdisks [69]. The underetching allows the relaxation of the GeSn layer with the added benefit of higher confinement due to a larger difference between refractive indices of the gain medium and the surrounding (air). Few months later, Al-Kabi *et al.* showed lasing at 2.5 µm and 110 K for a ridge waveguide [70]. In 2017, Reboud *et al.* fabricated GeSn microdisks with $y = 16$ at.% exhibiting lasing at 3.1 µm and 180 K. Similar characteristics were reported for waveguides, shown in figure 2.6, by Margetis *et al.* ($y = 17.5$ at.%) [55], and Dou *et al.* ($y = 22.3$ at.%) [56], along with lasing thresholds reduced below 137 kW cm^{-2} at 77 K. Recently, Thai *et al.* achieved lasing at 3.2 µm and 230 K for a microdisk with 16 at.% GeSn as the active medium [71]. In addition to Fabry-Pérot and microdisk cavities, photonic crystals were also investigated [72].

The intense research activity has led to a rapid growth in lasing temperature, from 90 K to 230 K in less than four years. Still, all these lasers operate with optical pumping. The Holy Grail for a Si-compatible light source is the realization of an electrically pumped group

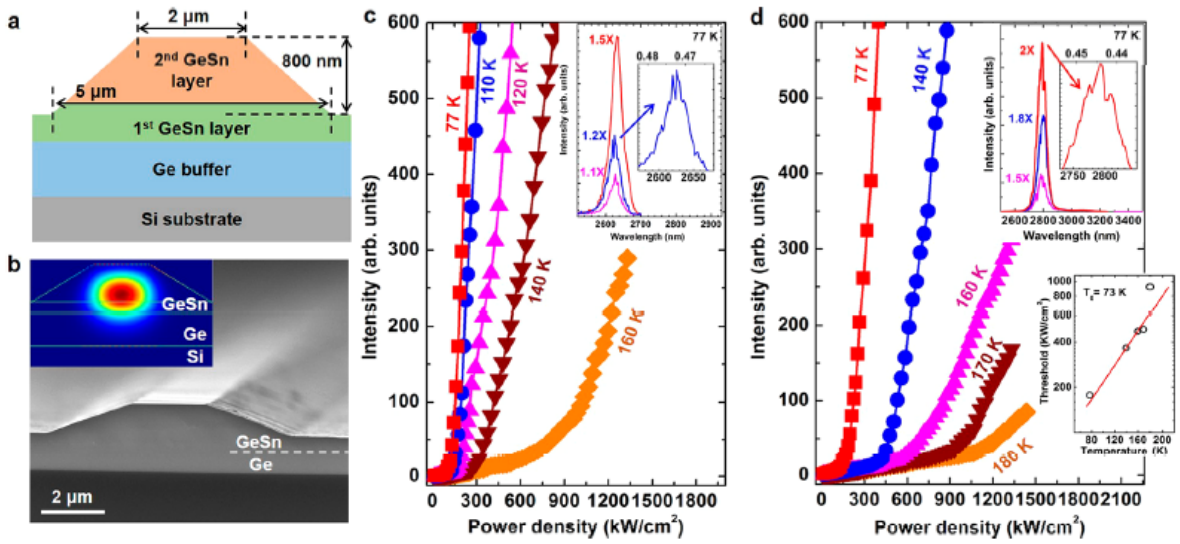

Figure 2.6 GeSn ridge waveguide laser [55]. (a) Schematic of the structure. (b) Scanning electron microscope image. Inset: Simulation of the fundamental mode. (c-d) Output power as a function of pump power for increasing temperatures. Inset: Spectra at 77 K and evolution of the threshold as a function of temperature. Reprinted with permission from (J. Margetis, S. Al-Kabi, W. Du, W. Dou, Y. Zhou, T. Pham, P. Grant, S. Ghetmiri, A. Mosleh, B. Li, J. Liu, G. Sun, R. Soref, J. Tolle, M. Mortazavi, and S.-Q. Yu, "Si-Based GeSn Lasers with Wavelength Coverage of 2–3 µm and Operating Temperatures up to 180 K," *ACS Photonics*, vol. 5, no. 3, pp. 827–833, mar 2018. [Online]. Available: `http://pubs.acs.org/doi/10.1021/acsphotonics.7b00938`). Copyright (2018) American Chemical Society.

IV laser operating at room temperature. Overcoming this challenge would be a real breakthrough.

LEDs

In the last decade, light emission from electrical injection of carriers was also demonstrated by the fabrication of GeSn [73–79], GeSn MQW [80] and SiGeSn MQW [81,82] light-emitting diodes (LEDs). These LEDs showed electroluminesence at wavelengths from 1.6 µm to 2.4 µm. Metal contacts were usually achieved by the combined deposition of either Cr, Au, Ni, and Al [77, 79, 82].

In fact, the development of light emission devices such as LEDs is closely related to that of photodiodes, with which they share important structural similarities.

2.3.2 Photodetectors

Planar photodetectors

The relevance of Sn-containing group IV photodetectors and solar cells relies on the possibility to tune the absorption in the NIR and MIR. While Si and Ge are transparent above 1.1 µm and 1.6 µm, respectively [83], Sn incorporation shifts the absorption edge to longer wavelengths.

In 2010, *p-i-n* GeSn photodiodes were demonstrated [84, 85]. The *n*-type top GeSn layer was P-doped at $1 \times 10^{20}\,\mathrm{cm}^{-3}$ and the bottom *p*-type Si was B-doped at $4.3 \times 10^{19}\,\mathrm{cm}^{-3}$. A Sn content as low as 2 at.% in the middle layer was sufficient to achieve higher quantum efficiencies than comparable Ge devices, with the additional benefit of extending the detection range to cover all telecommunication bands.

Over the years, GeSn photodetectors with a cut-off between 2.0 µm and 2.65 µm have been fabricated [17,86–91], which is beneficial for SWIR spectroscopy and sensing applications. In 2012, Gassenq *et al.* achieved photodetection up to 2.2 µm from a 9 at.% GeSn quantum well with Ge barriers [86]. They measured a $0.1\,\mathrm{A\,W}^{-1}$ responsivity for a 5 V bias. In 2014, Conley *et al.* reached a $1.63\,\mathrm{A\,W}^{-1}$ peak responsivity at 1.55 µm and a 2.4 µm cutoff from contacting a 10 at.% GeSn layer [87]. The same team improved the responsivity to $2.85\,\mathrm{A\,W}^{-1}$ in 2015 [88], and fabricated Ge/GeSn/Ge photodiodes which exhibited a $0.3\,\mathrm{A\,W}^{-1}$ responsivity at 1.55 µm and a 2.6 µm cutoff in 2016 [89]. In this case, doping levels were $1 \times 10^{19}\,\mathrm{cm}^{-3}$ and $5 \times 10^{18}\,\mathrm{cm}^{-3}$ for the *n* and *p*-Ge layers, respectively. In 2017, *p-i-n* MQW photodiodes with 10 at.% GeSn were demonstrated by Dong *et al.* [90] for light detection at 2 µm. Their main achievement is a low dark current density of $0.031\,\mathrm{A\,cm}^{-2}$ at room temperature. The doping concentrations were $2 \times 10^{19}\,\mathrm{cm}^{-3}$ and $5 \times 10^{19}\,\mathrm{cm}^{-3}$ for the *n*-Si and *p*-Ge layers, respectively. Other GeSn photodiodes with a longwave cutoff of 2.65 µm were realized in 2018 [91]. The device was made of a 11 at.% GeSn layer, *n*-doped to $2 \times 10^{18}\,\mathrm{cm}^{-3}$ on the top and p-doped to $1 \times 10^{17}\,\mathrm{cm}^{-3}$ on the bottom, sandwiched between *n*-type Ge ($2 \times 10^{19}\,\mathrm{cm}^{-3}$) and *p*-type Ge ($1 \times 10^{19}\,\mathrm{cm}^{-3}$). It exhibited a responsivity of $0.32\,\mathrm{A\,W}^{-1}$ at 2 µm and an external quantum efficiency of 20 %.

The reduction in responsivity and detectivity for increasing temperatures limits the performance of these devices. While GeSn detectors offer easier integration with the Si platform, other detector types such as III-V are still more competitive in terms of performance, as shown on figure 2.7.

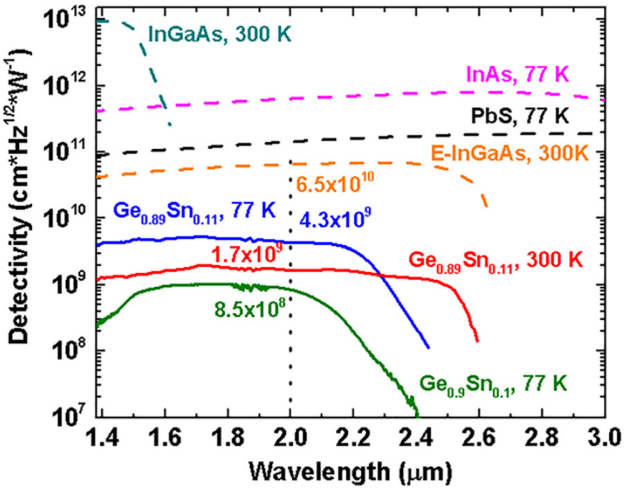

Figure 2.7 Comparison of the spectral detectivity for a 500 µm GeSn ($y = 11$ at.%) photodiode with III-V photodetectors at different temperatures [91]. Reprinted from H. Tran, T. Pham, W. Du, Y. Zhang, P. C. Grant, J. M. Grant, G. Sun, R. A. Soref, J. Margetis, J. Tolle, B. Li, M. Mortazavi, and S.-Q. Yu, "High performance $Ge_{0.89}Sn_{0.11}$ photodiodes for low-cost shortwave infrared imaging," *Journal of applied physics*, vol. 124, no. 1, p. 013101, jul 2018. [Online]. Available: `https://doi.org/10.1063/1.5020510`, with the permission of AIP Publishing.

Nanowires and nanopillars

The efficiency of semiconductor photodetectors is notably limited by the considerable reflection at the interface. In fact, refractive indices of Ge and GeSn are $n \geq 4$ in the visible and the NIR [92, 93], meaning the reflectance [94]

$$R \approx \left(\frac{n_1 - n_2}{n_1 + n_2}\right)^2 \tag{2.2}$$

is $\approx 40\,\%$ for an interface with air ($n_2 = 1$). A proven solution to decrease reflection at the interface, and therefore promote absorption in the device, is the addition of anti-reflection coatings [95, 96], which have intermediate refractive indices. Another option to increase even more the absorptance is the structuring of the active medium into non-planar geometries. For instance, GeSn [97] and Ge/GeSn core-shell nanowires (NWs) [98–100] grown via a vapor-liquid-solid (VLS) mechanism can achieve absorptance up to 98 % above the band gap [98]. In fact, absorptance in a NW is significantly enhanced for specific wavelengths corresponding to resonance modes [101–103]. This results in more absorbed power than in a bulk material of the same volume, a phenomenon known as the optical antenna effect [102, 104]. Another advantage of NWs over bulk is the relaxation of strain along the radial direction [105], which

helps in achieving a direct gap and promotes Sn incorporation.

It is also possible to obtain similar structures via top-down approaches such as reactive ion etching [59]. While bottom-up NWs are suited for fabrication of radial heterojunctions, axial heterojunctions are more easily achieved by top-down techniques. The relevance of the latter has been demonstrated by the fabrication of indium phosphide (InP) NW solar cells with a record conversion efficiency of 17.8 % [106]. In order to investigate an analogous absorptance enhancement for GeSn structures, simulations of optical properties of top-down GeSn nanopillars have been performed. The results are presented in chapter 5.

Since Sn content and strain are critical in determining device properties, they must be measured with reliable methods. The next section discusses the advances regarding Raman spectroscopy as a characterization technique to evaluate Sn content and strain down to the microscale.

2.4 Raman spectroscopy

Raman scattering spectroscopy is commonly used to investigate crystal phase and symmetry, isotopic content, electronic and phononic properties [107–109], as information-rich spectra are acquired from straightforward and non-destructive measurements. It is also one of the few characterization techniques which is sensible to both composition and strain [110, 111], together with XRD. Therefore, Raman spectroscopy is often employed to evaluate the chemical composition and lattice properties of group IV semiconductors such as strained Si [112–114], strained Ge [25, 115–117], SiGe [118–121], GeSn [35, 57, 122–130], and SiGeSn [131–134] layers. Since it uses excitation wavelengths near or in the visible, a small spot size ($\approx 1\,\mu m$) can be achieved using conventional lenses and objectives. This is an advantage over XRD, where a synchrotron is required to focus the beam on similar areas, and make it a method of choice for mapping the strain distribution in microstructures [113, 114].

Reports on the vibrational modes of GeSn mainly focused on the Ge-Ge longitudinal optical (LO) mode as the analyses relied on 488 nm [122, 123] or 532 nm [57, 124–129] excitation lines. Under these conditions, the signal-to-noise ratio is too low to clearly distinguish Sn-related vibrational modes in the vicinity of the more prominent Ge-Ge LO peak. This also applies to the study of ternary SiGeSn semiconductors [132, 133]. Oehme *et al.* [130] and D'Costa *et al.* [35] used a 633 nm and a 647.1 nm excitation laser, respectively, thus allowing a distinction of Ge-Ge and Ge-Sn modes, in addition to other features such as disorder-activated (DA) and Sn-Sn like modes. The enhanced signal-to-noise ratio is attributed to the increase in Raman scattering cross section when the excitation wavelength becomes close to

the material's E_1 gap [132,135]. This allowed them to provide a quantitative description of the evolution of peak positions as a function of the composition. However, in these studies, the investigated samples were either pseudomorphic [130] or relaxed [35]. Consequently, strain and compositional effects cannot be fully decoupled. More recently, Gassenq *et al.* addressed this issue by measuring the Raman shift for pseudomorphic layers before and after strain releasing via underetching [57], as shown in figure 2.8. However, only the Ge-Ge mode was analyzed, since the use of a 532 nm laser restrained the detection of other modes. In addition, not taking into account the DA mode [35] led to inaccurate fitting on the low-energy side of the Ge-Ge peak.

A model predicting the behavior of only one peak position is not enough to extract Sn composition and strain values from Raman measurements. Information on at least two variables is needed to decouple the two contributions. For instance, the measurement of composition and strain has been demonstrated for ternary SiGeSn alloys by tracking three distinct modes [134].

The need for measurement of both Sn composition and strain at the micrometer scale in GeSn alloys has prompted us to thoroughly investigate GeSn Raman vibrational modes, the analysis of which is presented in chapter 4.

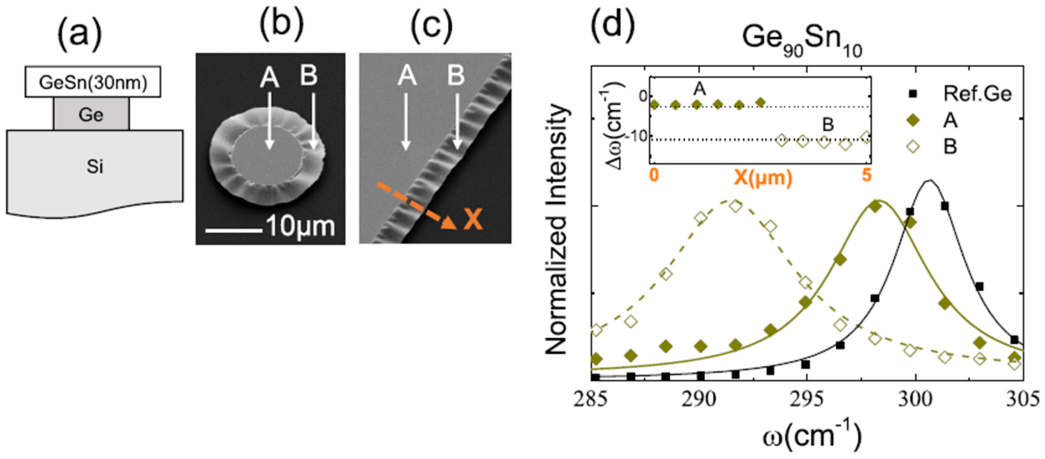

Figure 2.8 Decoupling composition and strain effects on Ge-Ge Raman shifts by Gassenq *et al.* [57]. Schematics (a) and scanning electron microscope images (b-c) of the devices. (d) Raman spectra measured on the GeSn layer along the X-axis shown in (c). Reprinted from A. Gassenq, L. Milord, J. Aubin, N. Pauc, K. Guilloy, J. Rothman, D. Rouchon, A. Chelnokov, J. M. Hartmann, V. Reboud, and V. Calvo, "Raman spectral shift versus strain and composition in GeSn layers with 6%–15% Sn content," *Applied Physics Letters*, vol. 110, no. 11, p. 112101, mar 2017. [Online]. Available: `http://aip.scitation.org/doi/10.1063/1.4978512`, with the permission of AIP Publishing.

This literature review highlights the great progress in GeSn material and devices since the first mention of its potential direct gap in 1982. The pace has accelerated in the last decade due to the availability of suitable commercial precursors, allowing the CVD growth of high-quality layers. Despite the demonstration of the major milestone that is lasing from a direct band gap and the advances regarding the development of photodetectors, many challenges are yet to be raised before a complete integration of photonic circuits on the Si platform is achieved. Important questions are the realization of an electrically pumped laser operating at room temperature and the improvement of the performance of photodetectors. Light emission at longer wavelengths would also be beneficial to cover a wider range of energies in the SWIR and MIR. The next chapters suggest possible avenues in terms of material characterization, as well as improved light emission and absorption.

CHAPTER 3 METHODS AND TECHNIQUES

This chapter presents an overview of the methods and techniques employed throughout this project. The chapter is divided in three sections. First, the analytical and numerical methods employed to calculate the optical properties of GeSn microstructures are explained. The second section describes the processes used to grow the layers and fabricate the microstructures, while the last section elaborates on the characterization techniques used to elucidate the basic properties of GeSn layers and structures.

3.1 Simulations of the optical properties of GeSn

3.1.1 Transfer matrices

Optical properties of thin films stacks can be obtained analytically via the transfer matrix method, which is notably used in the design of optical filters [136]. Each layer i from the stack in figure 3.1, of thickness d_i and of complex refractive index $N_i = n - ik$, is described by a matrix $\boldsymbol{M_i}$ [137]

$$\boldsymbol{M_i} = \begin{pmatrix} \cos\phi_i & \frac{i}{\eta_i}\sin\phi_i \\ i\eta_i \sin\phi_i & \cos\phi_i \end{pmatrix} \tag{3.1}$$

where

$$\phi_i = \frac{2\pi}{\lambda}\sqrt{N_i^2 - \alpha^2}\, d_i \tag{3.2}$$

is the phase shift, and

$$\eta_i = \begin{cases} \sqrt{N_i^2 - \alpha^2} & s\text{-polarized light} \\ N_i^2/\sqrt{N_i^2 - \alpha^2} & p\text{-polarized light} \end{cases} \tag{3.3}$$

is an effective index taking into account the angle θ_i with respect to the normal, which is defined using the constant $\alpha = N_i \sin\theta_i$. The matrix for a stacking of s layers is

$$\boldsymbol{M} = \begin{pmatrix} m_{11} & m_{12} \\ m_{21} & m_{22} \end{pmatrix} = \prod_{i=s}^{1} \boldsymbol{M_i} \tag{3.4}$$

The fraction of power reflected (the reflectance R), transmitted (the transmittance T), and

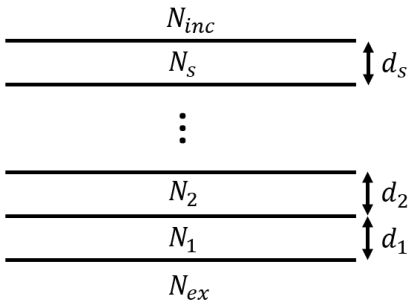

Figure 3.1 Schematic of a thin-film stack

absorbed (the absorptance A) by the whole stack are then

$$R = \left| \frac{\eta_{inc} m_{11} - \eta_{ex} m_{22} + \eta_{inc} \eta_{ex} m_{12} - m_{21}}{\eta_{inc} m_{11} + \eta_{ex} m_{22} + \eta_{inc} \eta_{ex} m_{12} + m_{21}} \right|^2 \tag{3.5}$$

$$T = \frac{\mathrm{Re}(\eta_{ex})}{\mathrm{Re}(\eta_{inc})} \left| \frac{2\eta_{inc}}{\eta_{inc} m_{11} + \eta_{ex} m_{22} + \eta_{inc} \eta_{ex} m_{12} + m_{21}} \right|^2 \tag{3.6}$$

$$A = 1 - R - T \tag{3.7}$$

This algorithm was implemented in a numerical analysis software (MATLAB) to evaluate the properties of GeSn layers grown on Ge on a Si substrate. This allowed the comparison between the initial planar geometry and top-down nanopillar arrays, for which the optical properties were evaluated via finite-difference time-domain simulations.

3.1.2 Finite-difference time-domain method

The analytical solution provided by the transfer matrix is limited to structures with a planar geometry. In the case of nanowires, for instance, numerical solutions describing the propagation of light in complex media are required to extract the optical properties. In this work, the patterning of the GeSn layer into nanopillar arrays was investigated to enhance the coupling of the light into the semiconductor region. Subwavelength structures were chosen to study this phenomenon, as larger structures display a bulk-like reflection. The simple case of cylindrical pillars was considered for the first demonstration, but a similar behavior is expected for other geometries, such as square prisms.

Finite-difference time-domain simulations (FDTD) have been employed to evaluate the performance of GeSn nanopillars. The methods takes the complex refractive index N as an input and iteratively solves Maxwell's equations discretized in space and time [138]. Being

a time-domain technique, Fourier transforms can be exploited to calculate optical properties for a range of frequencies simultaneously when using a broadband pulse as the source. However, the space and time domains are limited in size due to the finite capacity of the computer memory, meaning the accuracy of the model depends on the dimensions of the mesh and the choice of boundary conditions. Definition of the boundaries is of great importance especially for problems involving wave equations because of the oscillating nature of the solutions: Truncating the domain with hard-wall boundaries will often produce wrong results because of the reflection of the wave at the interface.

One solution is to extend the grid by adding a layer of a reflectionless absorbing material, called a perfectly matched layer (PML). Mathematically, the absorption in the PML region is introduced artificially by applying the following transformation to the wave equation [139]

$$\frac{\partial}{\partial x} \rightarrow \frac{1}{1 + i\frac{\sigma_x(x)}{\omega}} \frac{\partial}{\partial x} \tag{3.8}$$

where σ_x is a function of x and ω is the frequency of light. The same applies to y and z directions. This introduces an exponential decay of the wave, meaning it is now possible to truncate the simulation domain region and implement hard-wall conditions after the PML. PMLs are perfectly reflectionless by construction, however this applies for a continuous domain. The discretization leads to small numerical reflections. The reflected power can be reduced by using a thicker PML or a finer mesh up to the point where it is negligible.

In this work, broadband FDTD simulations have been carried out with the commercial software Lumerical. The domain consisted of a unit cell with one or two (effective) pillars, for square and hexagonal arrays respectively. Periodic boundary conditions were implemented in the x and y directions to obtain the properties of an infinite array of pillars, as illustrated in figure 3.2. In the z direction, PMLs were implemented below the Ge-VS and above the pillars. The method was benchmarked notably by reproducing results from ref. [106].

When light is injected at a non-normal incidence, electric and magnetic fields are not necessarily periodic from one unit cell to another. For this reason, the use of standard periodic boundary conditions can lead to errors. Bloch boundary conditions solve this problem by applying the correct phase shift when copying the fields. However, this is not appropriate for broadband simulations, since the phase shift causes the actual angle in the simulation to be wavelength-dependent. To overcome this problem, FDTD equations can be reformulated to remove the angular dependence [140], which is known as the Broadband Fixed Angle Source Technique (BFAST). This alternative algorithm and its own specific boundary conditions were implemented to study the absorption of broadband light from a non-zero angle

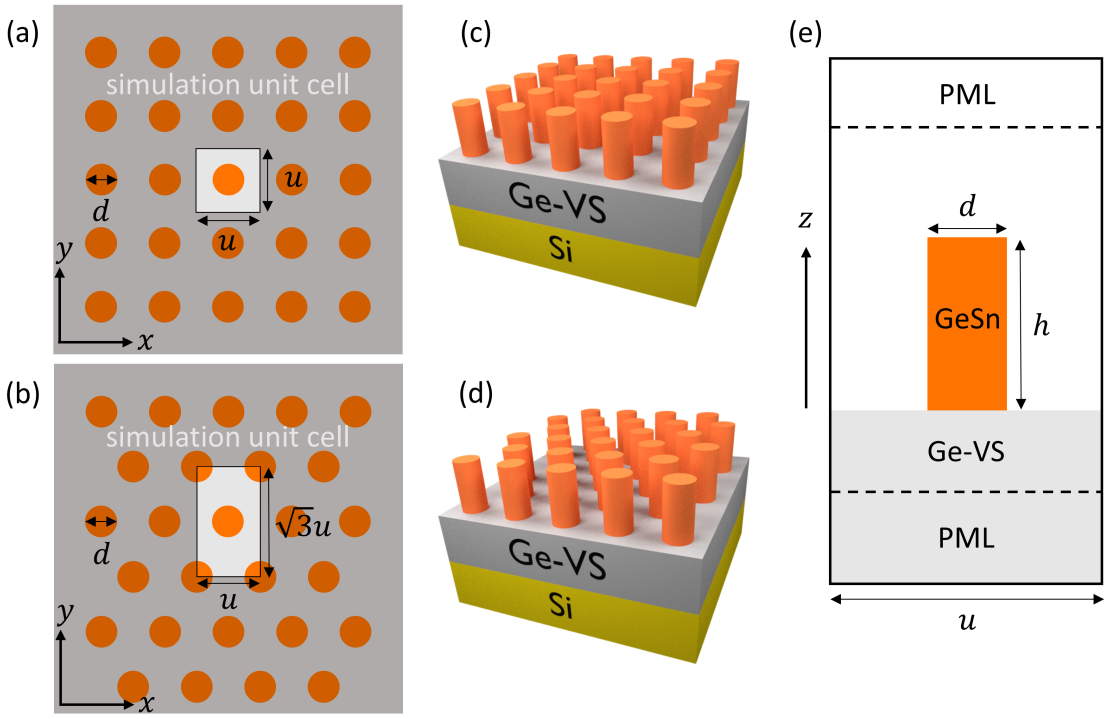

Figure 3.2 (a-b) Top-view for (a) square and (b) hexagonal arrays. (c-d) Corresponding 3D arrays. (e) Side-view of the simulation domain for square arrays.

of incidence.

The absorptance of the array is calculated from the distribution of the electric field intensity E over the unit cell of volume V and the permittivity ε of each material via [141]

$$A = \frac{1}{2}\int_V \omega\,|E|^2\,\mathrm{Im}(\varepsilon)\,\mathrm{d}V \tag{3.9}$$

3.2 Micro and nano fabrication

Microfabrication processes fall in three main categories: controlled addition of matter (deposition), pattering (lithography), and controlled removal of matter (etching) [142]. Techniques used throughout this work are presented below.

3.2.1 Growth of GeSn layers

Samples were grown in a custom-made reduced pressure chemical vapor deposition (CVD) system, for which a simplified working diagram appears on figure 3.3(a). Precursors in the gaz phase are introduced in the chamber through the showerhead and decompose on the

surface of the substrate. Residual gases are pumped to the exhaust. The sample is kept at the desired temperature by a feedback loop between the heater and a thermocouple. A susceptor favors uniformity of the temperature.

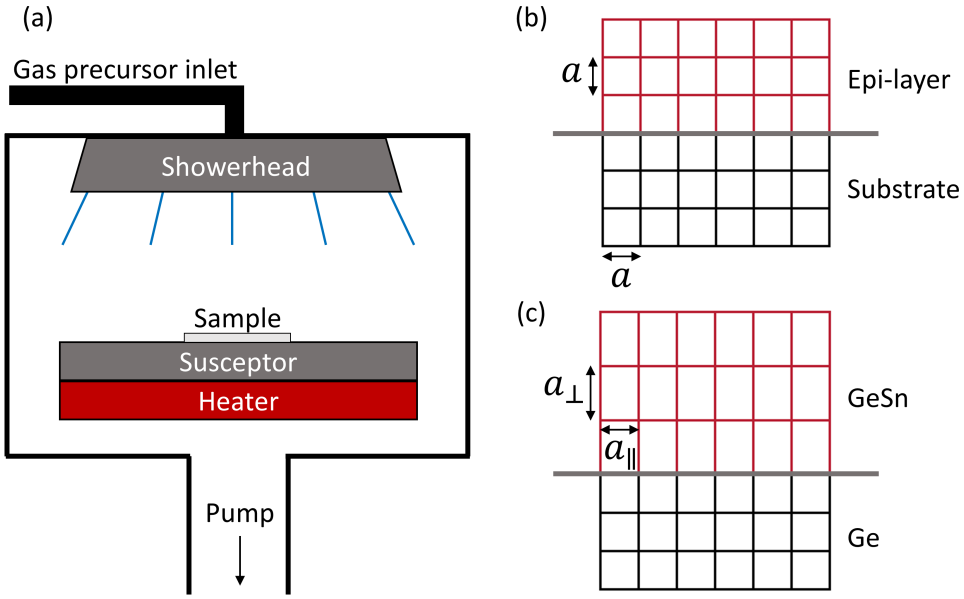

Figure 3.3 CVD epitaxy. (a) Illustration of the reduced pressure CVD. (b) Example of epitaxial growth of layers with comparable lattice constants. (c) Example of epitaxial growth of layers with a lattice mismatch.

When species are deposited following the crystallinity of underlying layers, the film is said to grow *epitaxially*, as illustrated on figure 3.3(b). The crystal symmetry is then transferred from the substrate. Epitaxial growth of materials with different lattice constants causes the films to be strained, which depending on the Poisson ratio can lead to a tetragonal distortion (opposite modifications of the in-plane $a_{\parallel}$ and out-of-plane $a_{\perp}$ lattice constants), as shown in figure 3.3(c). A layer is said to be *pseudomorphic* when its in-plane lattice constant is identical to that of the underlying layer despite of a difference in chemical composition.

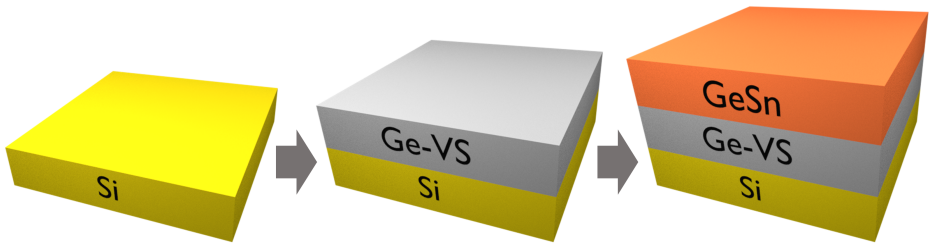

Figure 3.4 Process for the synthesis of crystaline GeSn layers on Si wafers

Samples employed in this study were grown with ultra-pure H_2 as carrier gas and 10 % monogermane (GeH_4) and tin-tetrachloride ($SnCl_4$) precursors [40, 41]. Si (100) wafers were first cleaned in a 2 % HF solution. A Ge virtual substrate (Ge-VS) was grown on the Si substrate, and $SnCl_4$ was subsequently introduced in the chamber to form a GeSn layer. Figure 3.4 illustrates the growth process.

3.2.2 Lithography

The definition of a pattern at the micro or nanoscale is achieved via lithography. A resist is first applied on the substrate by spin coating, then baked, exposed and developed. Resists are organic materials and are divided in two types. Exposition of a *positive* resist breaks the polymer into smaller segments. Exposed areas are then dissolved by a solvent (the *developer*). *Negative* resists, on the other hand, solidify by polymerization or cross-linking during exposition. Unexposed areas are dissolved by the solvent.

Exposition is achieved either with UV light, which is known as *photolithography*, or with electrons, a technique called *electron-beam lithography* (EBL). UV-exposure is performed through a photomask containing the desired pattern. EBL functions similarly to a scanning electron microscope (SEM). It uses an electron beam to pattern the resist directly without a physical intermediate mask, making it more versatile. It also allows the definition of features with an improved resolution (down to < 10 nm). On the other hand, the time required to move the beam can result in very long processing durations. In particular, the choice of resist type becomes crucial to avoid scanning very large surfaces. For instance, in the case of GeSn microdisks, only circular areas of the disks are exposed [59]. Thick negative resists such as ma-N 2410 is thus used as an etching mask. In this case, EBL is preferred over photolithography due to its flexibility. Other larger structures were also patterned via photolithography [82, 84, 86, 87, 89, 143].

In this work, lithography steps were carried out using ma-N 2400 series negative resists. Exposure was performed in a Raith e-line EBL with a beam energy of 10 kV. Processing steps are illustrated on figure 3.5.

3.2.3 Etching

Etching procedures allow the transfer of the pattern defined by lithography into the sample via selective removal of matter. They are classified as *wet* etchings, where the sample is immersed in a liquid solution, and *dry* etchings, which attack the surface via ion bombardment.

Reactive-ion etching (RIE) is a type of dry etching commonly used in both academic and

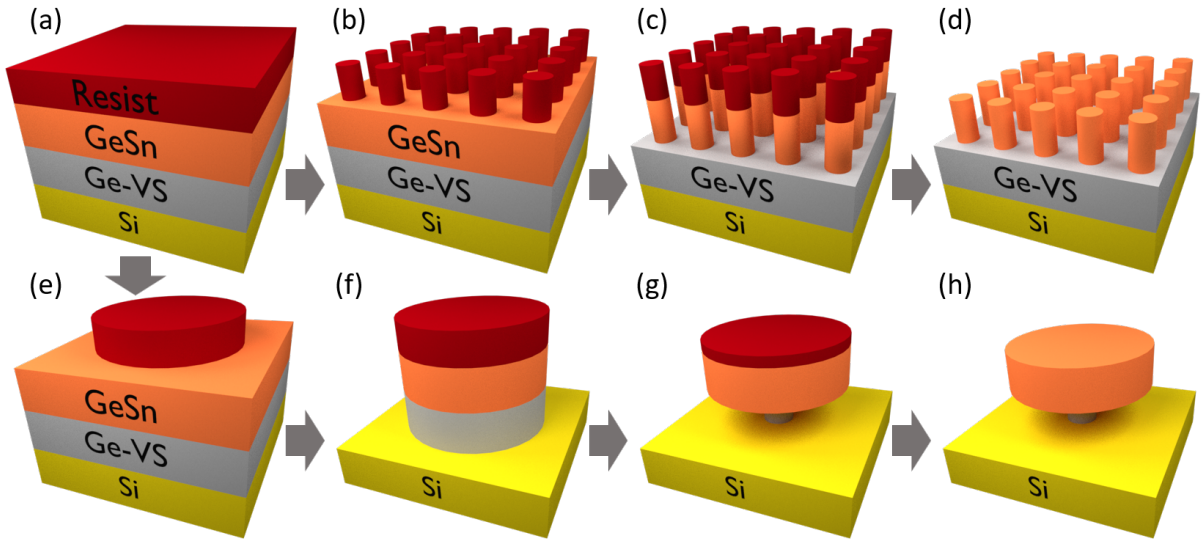

Figure 3.5 Process for patterning and etching GeSn layers. (a) Application of resist. (b) Exposition of pillars and development. (c) Cl_2 directional etch. (d) Resist removal. (e) Exposition of disks and development. (f) Cl_2 directional etch. (g) CF_4 isotropic etch. (h) Resist removal.

industrial processes. It relies on the generation of a plasma of reactive gases via a high-power radio-frequency electromagnetic field in a low-pressure environment. Etching can be both *physical*, resulting from the impact of the high-energy ions, and *chemical*, resulting from chemical reactions between the sample surface and species in the plasma.

Inductively coupled plasma (ICP) etching is a type of RIE which uses two radio-frequency generators to provide more control over the etching. The plasma density is regulated by a first generator, while a second one determines the ion energy. Typically, a dense plasma with low-energy ions yields a chemical, isotropic etching, whereas greater acceleration of fewer ions produces a physical, directional etching.

GeSn layers are sometimes etched in ammonia peroxide solutions (H_2O_2:NH_4OH:H_2O) [126, 144]. In 2013, Gupta *et al.* developed a CF_4-based dry etching recipe to selectively etch Ge over GeSn and applied it to the fabrication of GeSn microdisks [58]. To first remove the GeSn layer and expose the Ge surface, they used a wet etching. However, this isotropic etch is not suitable for thicker GeSn layers as straight sidewalls are more difficult to obtain. A Cl_2-based ICP etching was later developed for the directional etching of GeSn, allowing the fabrication of thick GeSn microdisks using two consecutive dry etchings [59, 145]. In the case of suspended structures such as microdisks, wet etchings can cause the membranes to collapse on the substrates due to the strong capillary forces. Dry processes thus represent an

important advantage for underetching.

For the present work, dry etchings were performed in a Plasmalab 100 ICP-RIE system from Oxford with parameters listed in table 3.1. Directional etchings mainly employed Cl_2, while Ge isotropic etchings are CF_4-based. These are illustrated in figure 3.5. Recipes were adapted from [59].

Table 3.1 RIE recipes

Parameters	Directional etch	Ge isotropic etch
O_2 flow (sccm)	4	2
N_2 flow (sccm)	10	0
Cl_2 flow (sccm)	40	0
CF_4 flow (sccm)	0	40
ICP power (W)	200	2500
RF power (W)	100	1
Pressure (mTorr)	20	15
Temperature (°C)	30	20

The selective etch of the Ge-VS allowed to fabricate suspended GeSn structures to investigate the effect of strain relaxation on the optical emission. An array of microdisks was chosen as the pattern to achieve an uniform relaxation. Diameters were inferior to 8 µm to prevent damage to the GeSn layer that could occur during longer etches.

The techniques presented in this section were used to microfabricate GeSn nanopillars and microdisks. In this work, EBL was employed for all structures, meaning the process was completed without a single mask. Note that the larger dimensions of the microdisks mean they can also be defined using photolithography.

3.3 Characterization techniques

3.3.1 Ellipsometry

The calculations and simulations of optical properties of GeSn structures require a prior knowledge of the complex refractive index N. To this end, ellipsometry has been extensively used to characterize the as-grown GeSn layers. It is a powerful technique to measure n and k of thin films while also providing valuable information about thicknesses and an approximation of surface roughness.

The working principle of an ellipsometer is depicted in figure 3.6 [146]. Light with known polarization is sent on the sample. Since the components of the electric field parallel (e_p)

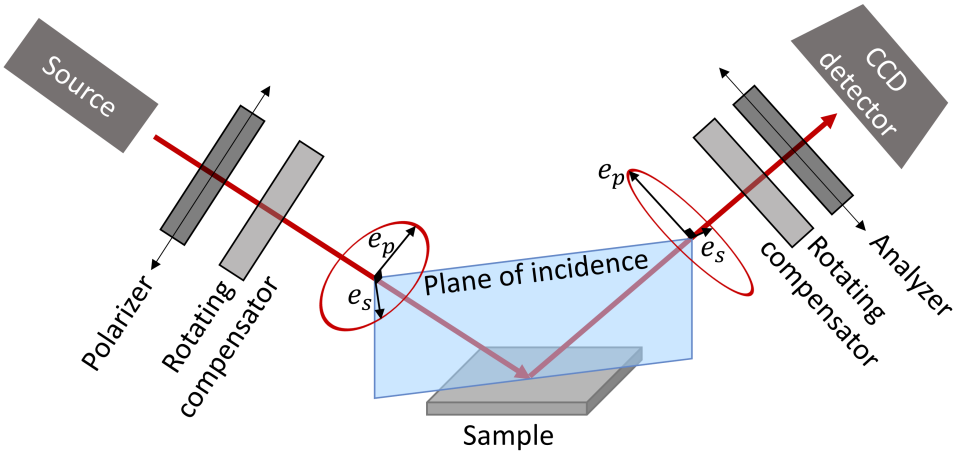

Figure 3.6 Diagram of an ellipsometer with dual rotating compensators

and perpendicular (e_s) to the plane of incidence interact differently with the sample, there is a change of the overall polarization. The rotation of polarizers or compensators allows the selection of incident and reflected polarization. The detector records the ratio between Fresnel reflection coefficients for both s (r_s) and p (r_p) polarizations, which can be expressed as an amplitude ratio Ψ and a phase difference Δ via

$$\frac{r_p}{r_s} = \tan(\Psi)\, e^{i\Delta} \tag{3.10}$$

n and k cannot be derived directly from ellipsometry raw data. An optical model needs to be implemented, and the optical constants and the thicknesses of the films are iteratively adjusted to reproduce the experimental (Ψ,Δ). Since optical constants are not measured directly, their accuracy is highly dependent on the quality of the model.

Measurements of GeSn optical constants used in this work have been performed on a pair of variable angle spectroscopic ellipsometers from J.A. Woollam, operating on wavelength ranges from 200 nm to 2500 nm and 2 µm to 30 µm.

3.3.2 Photoluminescence spectroscopy

The measurement of photoluminescence (PL) spectra of semiconductors is crucial to investigate their band structure, as the emitted light conveys important information about the material's optical transitions.

The working principle is illustrated in figure 3.7. The sample is first illuminated by an excitation light source. The energy of the incident photons has to be greater than the band

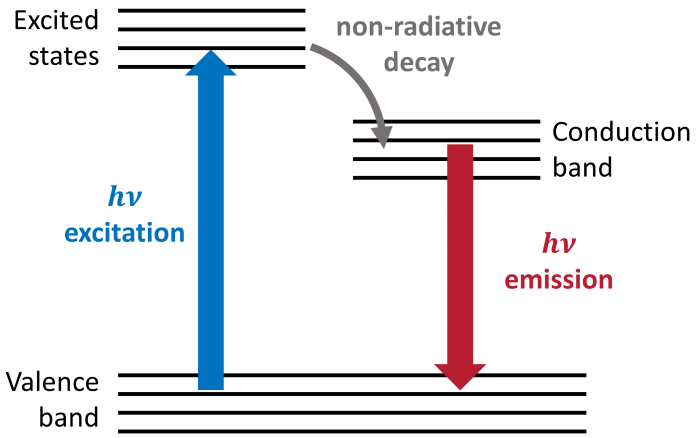

Figure 3.7 Energy transitions involved in a PL experiment

gap of the material in order to promote electrons to excited states. Electrons then thermalize via non-radiative transitions to the conduction band. If electrons and holes recombine by a radiative process, a photon is emitted with an energy corresponding to the optical transition.

In this study, a PL setup with a lock-in technique was used, the schematics of which is illustrated in figure 3.8. The excitation consisted of a continuous-wave 976 nm laser. The emission energy was spectrally resolved by a Thermo Fisher Nicolet iS50R FTIR spectrometer and recorded by a liquid nitrogen cooled HgCdTe detector. The system is confined in a nitrogen environment to prevent absorption from water molecules.

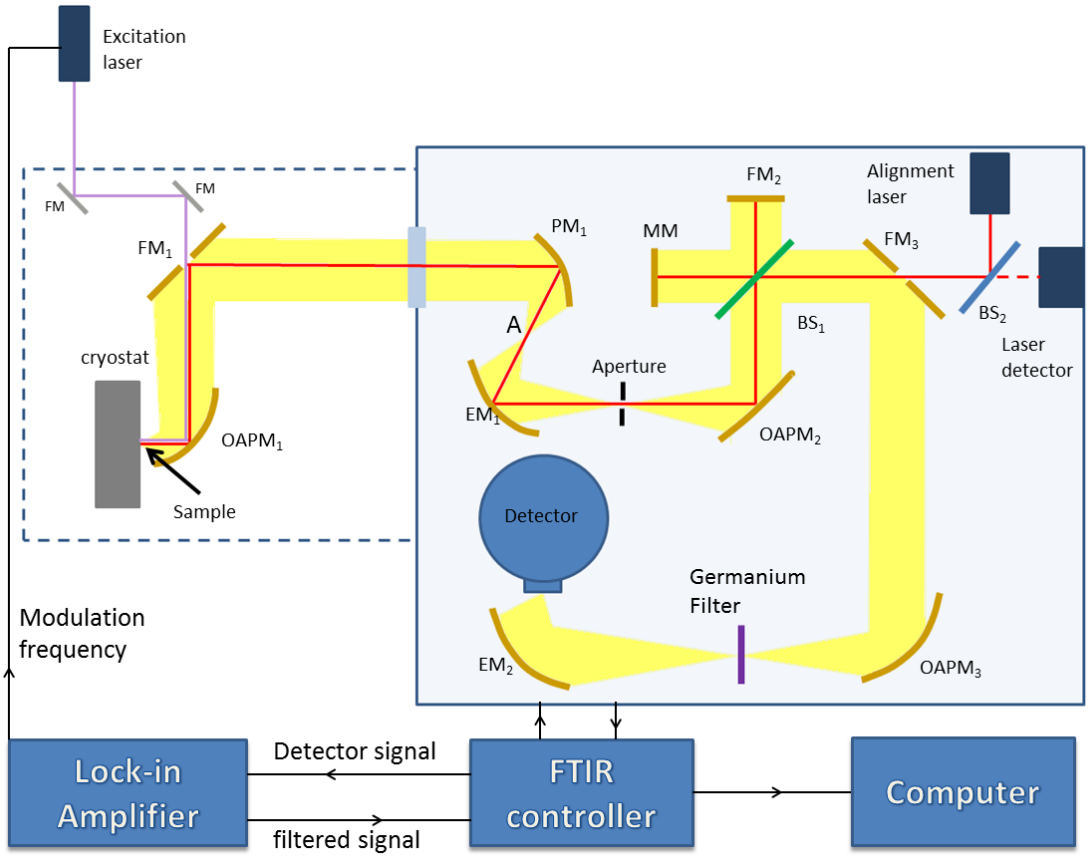

Figure 3.8 Schematics of the PL setup. The emission is collected by the optical path drawn in yellow, and the red line represents the path of the alignment laser [40]. Reprinted from the supplementary material of S. Assali, J. Nicolas, S. Mukherjee, A. Dijkstra, and O. Moutanabbir, "Atomically uniform Sn-rich GeSn semiconductors with 3.0–3.5 µm room-temperature optical emission," *Applied Physics Letters*, vol. 112, no. 25, p. 251903, jun 2018. [Online]. Available: `http://aip.scitation.org/doi/10.1063/1.5038644`, with the permission of AIP Publishing.

3.3.3 Raman spectroscopy

Raman spectroscopy relies on the inelastic scattering of light with a material to give information on its vibrational and rotational modes. In the case of solids, the energy difference between the incident and scattered photons, called the Raman shift, corresponds to energy absorbed (Stokes scattering) or emitted (anti-Stokes) via interaction with one or two phonons. These scattering phenomena are depicted in figure 3.9, in addition to the elastic Rayleigh scattering.

By analogy with photons, which are elementary oscillations of electromagnetic waves, phonons are elementary mechanical waves *and* particles underlying the quantized nature of vibrations

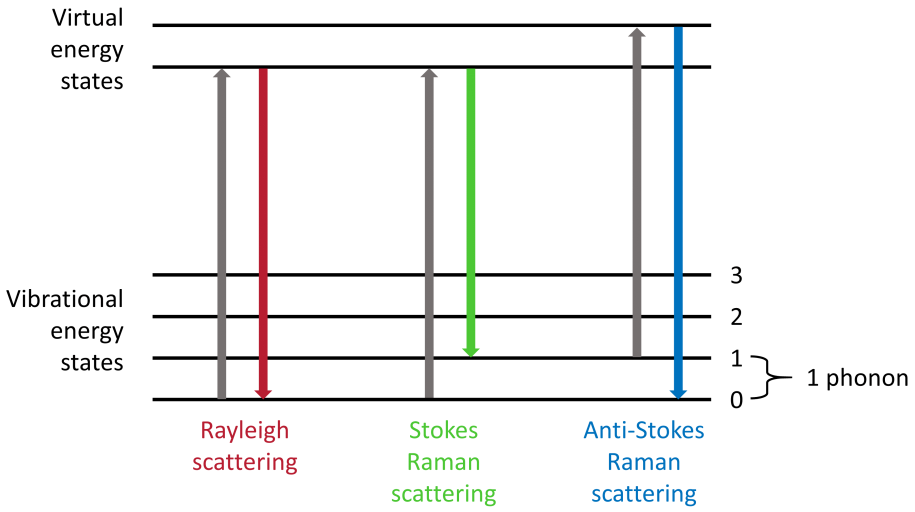

Figure 3.9 Energy diagram of light scattering phenomena

in solids. Their energy levels are discrete and characteristic to the material. For this reason, the measure of phonon energies using Raman spectroscopy results in spectra providing a wealth of information for the material under study. An example of the phonon dispersion bands (the relation between their wavevector $\vec{q}$ and frequency ω) is illustrated for Ge in figure 3.10, along with their distribution in energy (density of states).

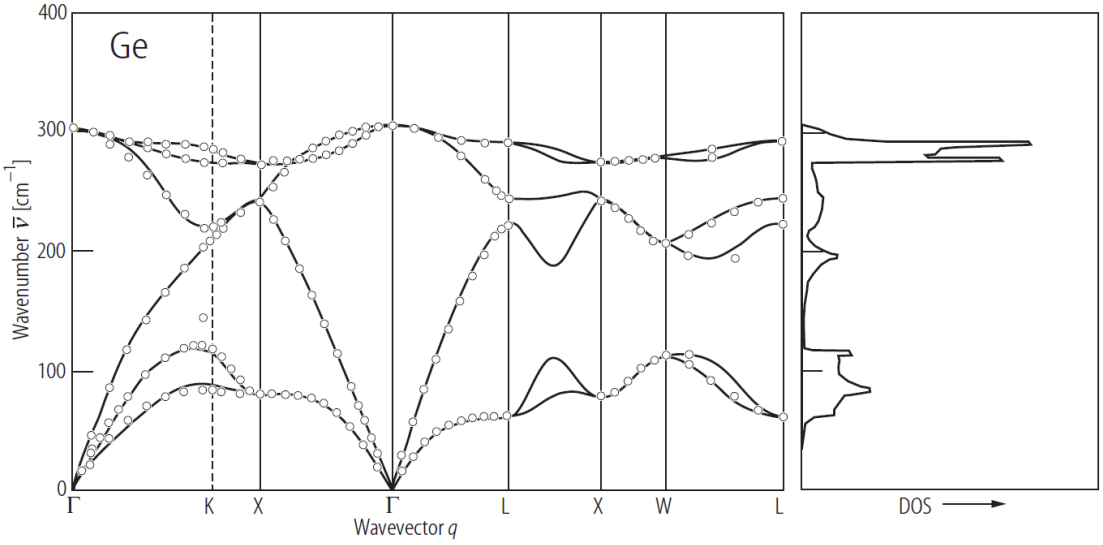

Figure 3.10 Phonon band diagram of Ge (left) and corresponding phonon density of states (right) [147]. Reprinted by permission from Springer Nature Customer Service Centre GmbH: Springer Nature, Group IV Elements, IV-IV and III-V Compounds. Part a - Lattice Properties by Collaboration: Authors and editors of the volumes III/17A-22A-41A1a, Copyright (2001).

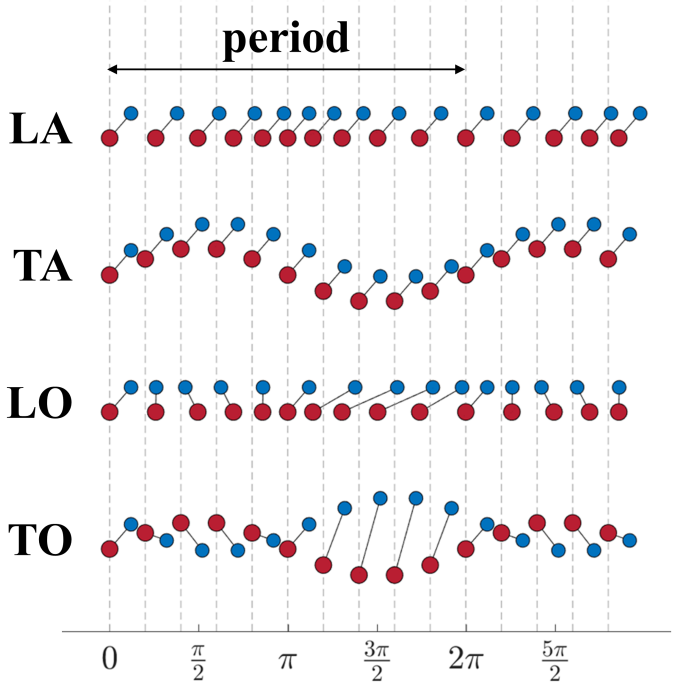

Figure 3.11 Phonon types in solids: (a) LA, (b) TA, (c) LO, and (d) TO

Phonons are either *acoustical* (A) or *optical* (O), as illustrated in figure 3.11. The first case describes a wave for which neighboring atoms in the unit cell move in phase. For infinitely long wavelengths, this corresponds to a translation of the crystal: No energy is carried, and the three acoustical branches reach $0\,\mathrm{cm}^{-1}$ at the $\Gamma(\vec{q} = \vec{0})$ point. For optical phonons, neighboring atoms move out of phase, which results in a finite energy for $\vec{q} = \vec{0}$.

A band diagram of a crystal with N atoms in the primitive unit cell has $3N$ branches. The first three branches are for acoustical phonons, whereas the next $3N - 3$ are optical branches. For Ge, a diamond-cubic crystal with 2 atoms in the primitive unit cell, there are three acoustical branches, degenerate at the Γ point ($0\,\mathrm{cm}^{-1}$), and three optical branches, also degenerate at the Γ point ($300\,\mathrm{cm}^{-1}$). Phonons are additionally classified as *longitudinal* (L) or *transverse* (T), depending on whether the displacement of atoms is parallel or perpendicular to the propagation of the wave.

Not all phonons can be observed in the first-order Raman spectrum. In addition to energy conservation (apparent in figure 3.9), interaction between photons and phonons must respect momentum conservation. If $\vec{k} = \frac{2\pi n}{\lambda}$ is the wavevector of the incident ($\vec{k_i}$) and scattered ($\vec{k_s}$) photons, then

$$\vec{k_i} = \vec{k_s} \pm \vec{q} \tag{3.11}$$

which means $\vec{q}$ is approximately

$$0 \leq |\vec{q}| \leq \frac{4\pi n}{\lambda} \tag{3.12}$$

The incident light is usually produced by a laser in the visible or the near infrared. Consequently, the wavelength λ is much greater than a, and $\vec{q}$ is very close to the center of the Brillouin zone. (For instance, the L point on the edge of the Brillouin zone corresponds to a wavevector $\vec{q} = [\frac{\pi}{a}, \frac{\pi}{a}, \frac{\pi}{a}]$). For this reason, only optical modes near the Γ point appear in the first-order (single phonon) Raman spectra. The observation of other modes require processes involving at least two phonons. Since the probability of such event is reduced, the intensity of second-order peaks is usually much weaker.

It is possible to further investigate the nature of phonons by performing polarized Raman measurements, where a set of polarizers is added on the optical path to select the incident $\vec{e_i}$ and scattered $\vec{e_s}$ polarizations. The intensity of the scattered light is given by [107]

$$I_s \propto |\vec{e_i} \cdot \boldsymbol{R} \cdot \vec{e_s}|^2 \tag{3.13}$$

where

$$\boldsymbol{R} = \frac{\partial \chi}{\partial \boldsymbol{Q}}_0 \hat{\boldsymbol{Q}}(\omega_0) \tag{3.14}$$

is the Raman tensor. χ is the electric susceptibility and $\boldsymbol{Q}$ is the vector displacement of an atom induced by a phonon. $\boldsymbol{R}$ holds information about the crystal symmetry, and can therefore be calculated by means of group theory. Si, Ge, α-Sn and their alloys belong to the O_h space group. The Raman matrices for the normal modes are then

$$\begin{aligned}
\boldsymbol{R_{A1}} &= \begin{pmatrix} a & 0 & 0 \\ 0 & a & 0 \\ 0 & 0 & a \end{pmatrix} & \boldsymbol{R^x_{T2}} &= \begin{pmatrix} 0 & 0 & 0 \\ 0 & 0 & c \\ 0 & c & 0 \end{pmatrix} \\
\boldsymbol{R_E} &= \begin{pmatrix} b & 0 & 0 \\ 0 & b & 0 \\ 0 & 0 & -2b \end{pmatrix} & \boldsymbol{R^y_{T2}} &= \begin{pmatrix} 0 & 0 & c \\ 0 & 0 & 0 \\ c & 0 & 0 \end{pmatrix} \\
\boldsymbol{R_{E'}} &= \begin{pmatrix} -\sqrt{3}b & 0 & 0 \\ 0 & \sqrt{3}b & 0 \\ 0 & 0 & 0 \end{pmatrix} & \boldsymbol{R^z_{T2}} &= \begin{pmatrix} 0 & c & 0 \\ c & 0 & 0 \\ 0 & 0 & 0 \end{pmatrix}
\end{aligned} \tag{3.15}$$

where a, b, c are constants.

The combination of setup geometry and crystal symmetry determines whether the modes are *allowed* (or *Raman-active*), if $I_s \neq 0$, or *forbidden*, if $I_s = 0$. The axes convention is illustrated

in figure 3.12. The scattering configuration is completely described by the direction and the polarization of the incident and scattered photons, commonly written in the Porto notation: $\hat{k_i}\,(\hat{e_i},\hat{e_s})\,\hat{k_s}$.

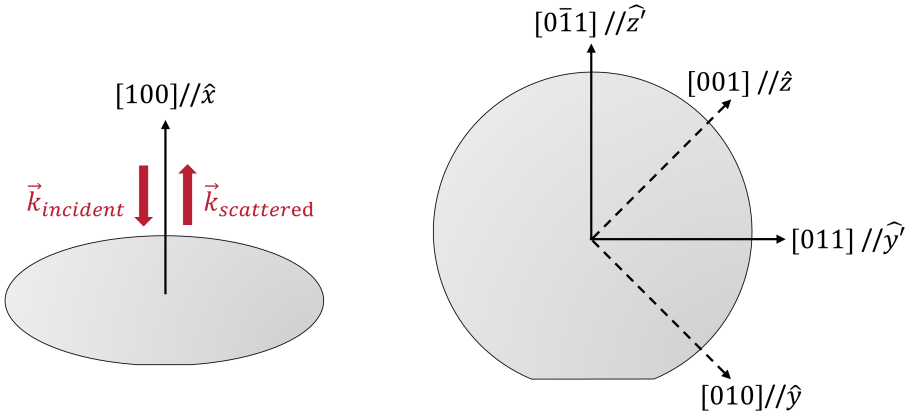

Figure 3.12 Definition of the coordinate system with respect to the main cristallographic axes. (GeSn layers are grown on Si (100) wafers). Incident and scattered beams are both oriented along $\hat{x}$. Note that all measurements were performed in the backscattering geometry.

Instrumentation

Measurements are performed using an InVia Raman Microscope from Renishaw with a 633nm laser and an 1800/mm grating. The wavelength choice is based on the enhanced signal-to-noise ratio observed when the excitation energy is close to the material's E_1 gap. A simplified diagram of the setup is illustrated on figure 3.13. A polarizer is added in the optical path for polarized Raman measurements. Moving an half-wave plate (HWP) in and out of the path rotates the polarization by 90 °, which determines the component eliminated by the polarizer.

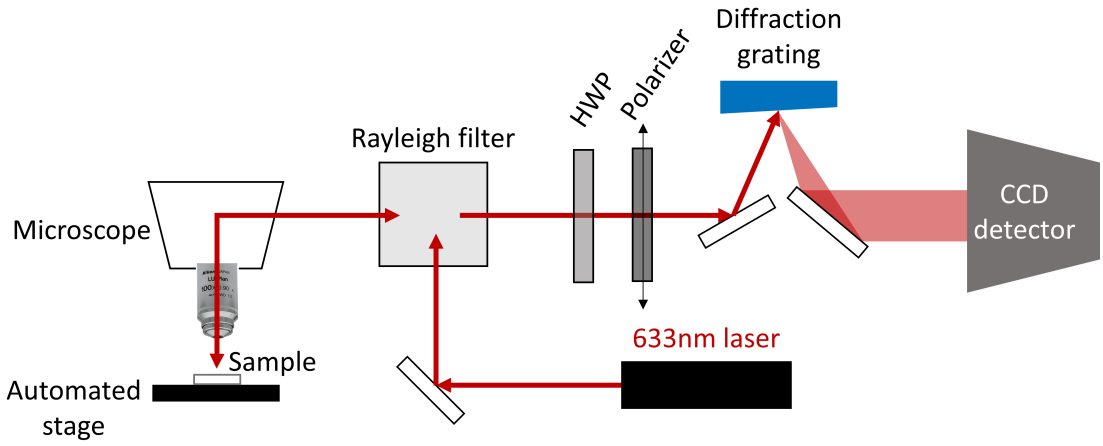

Figure 3.13 Diagram of the Raman setup used in this study. Light is directed on the sample and to the detector via a Rayleigh filter instead of a conventional beamsplitter.

3.3.4 Scanning electron microscopy

Visual inspections are important to assess the quality of the microfabrication process. However, structures of such small size cannot be observed with a conventional optical microscope. In this work, the inspection of nanopillars and microdisks is performed using a scanning electron microscope (SEM).

The working principle of a SEM is illustrated in figure 3.14(a). Electrons are thermionically emitted from an electron gun and accelerated by an electric field. One or several condenser lenses focuses the beam to a spot size of the order of 1 nm. The interaction of electrons with the sample generates backscattered electrons, secondary electrons, auger electrons, X-rays, and photons via cathodoluminescence. The current measured by the secondary electrons detector (a common imaging mode) corresponds to the signal for one pixel. Finally, deflection coils move the beam to scan a rectangular area on the sample surface, which forms an image. The constrast is due to topography, chemical composition, or local charging of the surface.

The main advantage of an SEM is the fine spatial resolution. Even for state-of-the-art optical microscopes, with numerical apertures $NA \approx 1$, the resolution

$$Res = \frac{\lambda}{2NA} \tag{3.16}$$

is limited by the relatively large wavelength of the incident light in the visible ($\lambda \approx 500\,\text{nm}$). Using electrons as the probe results in a much shorter wavelength. For instance, an electron accelerated in a 5 kV field has a DeBroglie wavelength of 0.017 nm. This means the resolution of an SEM is limited by the spot size rather than the electrons wavelength.

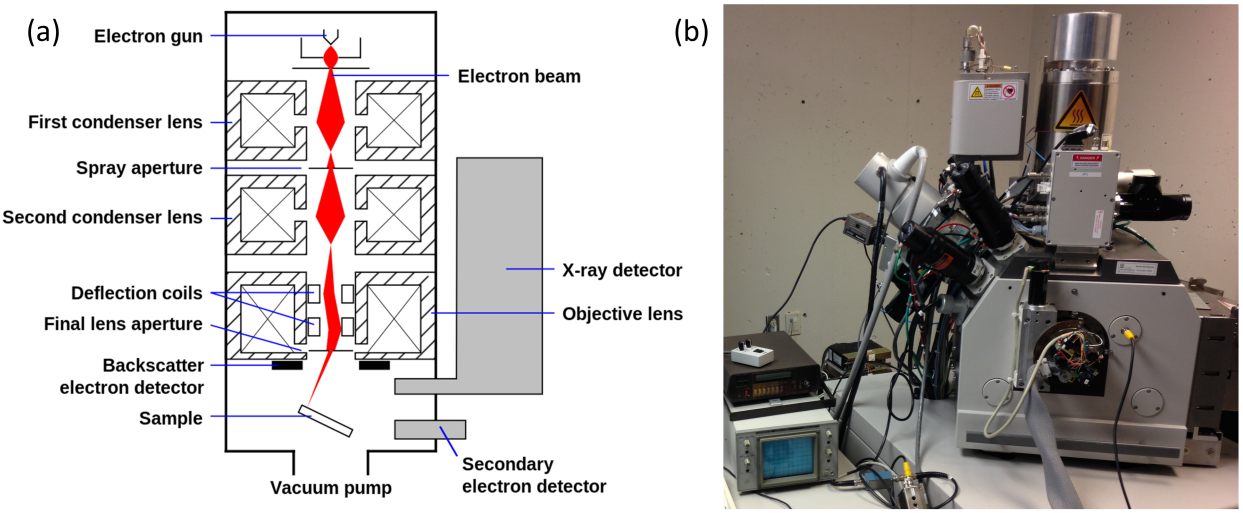

Figure 3.14 (a) SEM schematics. Reproduced with permission from `https://commons.wikimedia.org/wiki/File:Schema_MEB_(en).svg`. (b) The SEM used in this work.

Focusing electrons into a narrow beam makes for a long depth of field, which is useful for rendering three-dimensional features. Furthermore, SEM imaging allows a very large range of magnifications, often from 100 to 300 000 times. For these reasons, SEM is widely used to acquire images of micro and nano-sized structures. The electron beam of an FEI Strata DualBeam-235, shown in figure 3.14(b) was used for most SEM images in this work.

3.3.5 Spectrophotometry

Spectrophotometry allows the quantitative measurement of optical properties, notably reflectance and transmittance of thin films stacks. It relies on the comparison of light intensities measured after interaction with the sample and a known reference, typically in a range of wavelengths. For simple stacks, optical constants and films thicknesses can be retrieved from the interference fringes visible on the spectrum.

A Lambda 1050 spectrophotometer from PerkinElmer was used to measure reflectance and transmittance of microstructured GeSn samples. The absorptance could then be retrieved using equation (3.7). The schematic of the instrument is exhibited in figure 3.15. The combination of deuterium and tungsten-halogen sources allows to cover the 175 nm to 2500 nm range. A single wavelength is selected via a pair of monochromators, and a chopper (**BS**) sends the monochromatic light successively on the sample (**S**) and the reference (**R**). For both reflection and transmission configurations, light is collected by either a photomultiplier tube

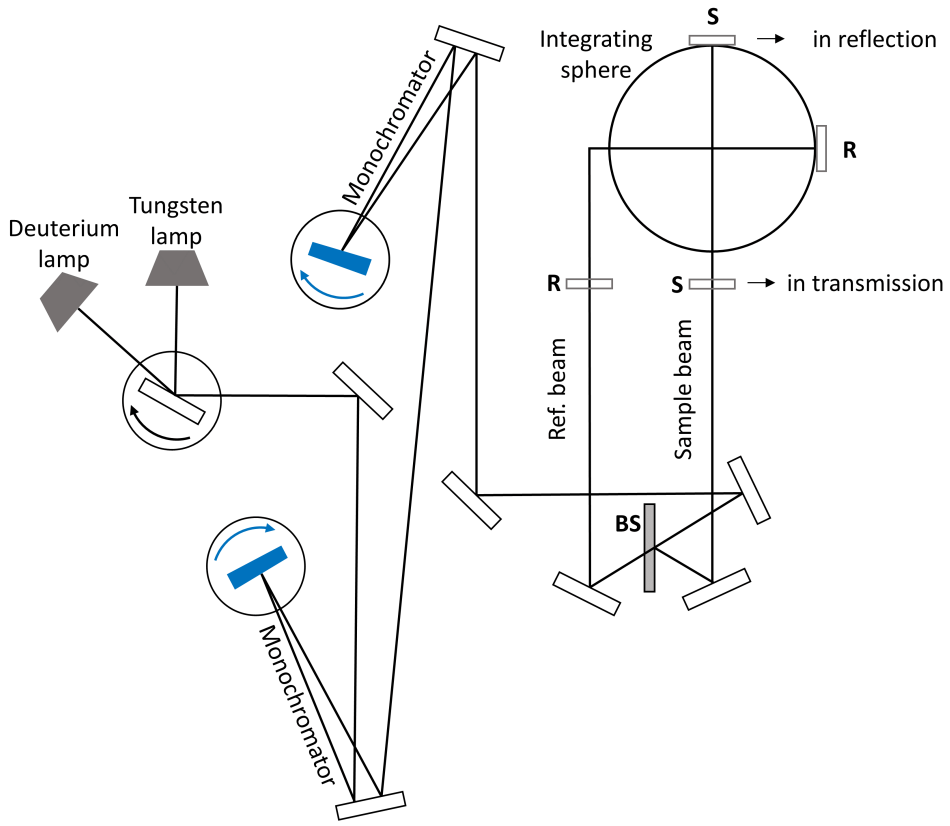

Figure 3.15 Diagram of a PerkinElmer Lambda 1050 spectrophotometer

or an InGaAs detector inside an integrating sphere. A scan of over the wavelength range is accomplished by rotation of the monochromators. A removable port in the sphere is placed in the direction of specular reflection, allowing the quantification of specular and diffused components. For reflectance measurements, the sphere internal material (Spectralon®) is used as a reference, whereas air (i.e. no sample) is used as a reference for transmittance.

3.3.6 X-ray diffraction

X-ray diffraction (XRD) allows direct measurement of the interatomic lattice constant [148]. This is useful for the characterization of crystals, especially thin films grown via epitaxy, as information such as strain, degree of crystallinity and composition can be deduced from the diffraction spectrum. This explains why XRD is widely used for the characterization of group IV materials [39, 41, 44, 61, 71, 72, 149–153].

The technique relies on the interference between an incident X-ray beam and elastically scattered photons from the sample, as illustrated in figure 3.16. Signal is maximized for

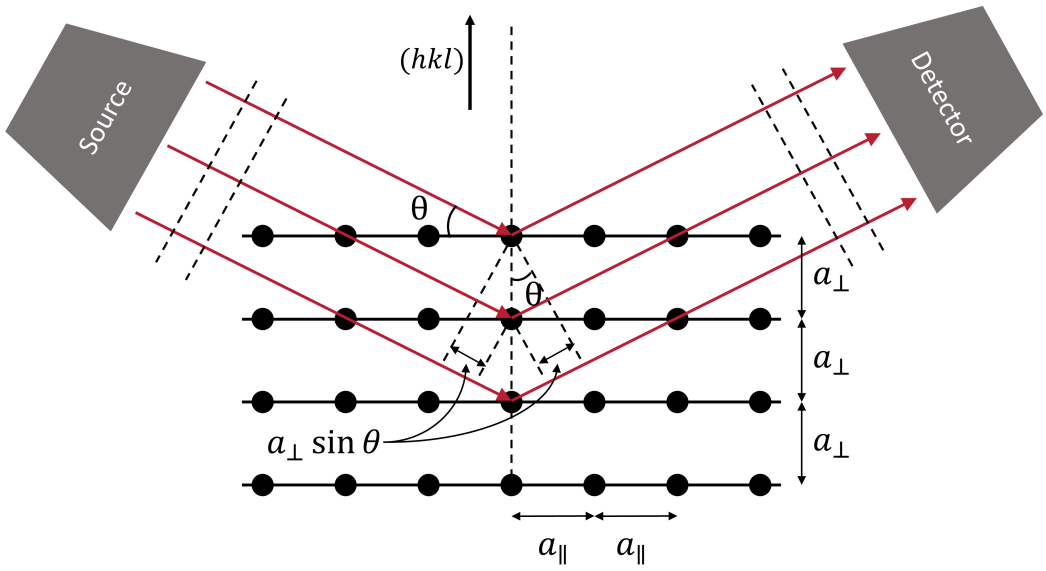

Figure 3.16 Condition for constructive interference for the plane (hkl)

constructive interference which occurs for specific angles θ described by Bragg's law,

$$m\lambda = 2a_\perp \sin\theta \tag{3.17}$$

where $m \in \mathbb{N}^*$ and $a_\perp$ is the out-of plane lattice constant. Scanning over a range of angles results in a diffraction spectrum. In a standard $2\theta - \omega$ scan, the sample and the detector both rotate so that the angle of the scattered beam entering the detector remains equal to the angle of incidence. Reciprocal space maps (RSM), obtained by scanning over two distinct orientations, allow to decouple contributions to the diffraction peaks. In the case of substitutional solids such as GeSn, composition and strain (y,ε) can be extracted from two coordinates of the peak position in the reciprocal space (q_x,q_z). While the lattice constant is measured directly, the determination of y and ε is based on assumptions for the Poisson coefficient, the ratio of elastic constants C_{12}/C_{11}, and the equilibrium lattice constant in equation (2.1). XRD measurements presented in this work were performed on a Bruker D8 Discovery, using the $K_{\alpha 1}$ line ($\lambda = 1.5406\,\text{Å}$) of a copper source. y and ε were calculated from peak positions in RSM using a bowing parameter of $b^{GeSn} = 0.041\,\text{Å}$ [48]. While this technique is highly beneficial for bulk material, the millimeter-size spot in conventional XRD makes it less suitable to the study of micro and nanostructures. Smaller spot sizes ($< 100\,\text{nm} \times 100\,\text{nm}$) can be obtained with a synchrotron [154], which is known as nano-beam XRD.

Characterization techniques presented in this section are commonly used to evaluate material

properties of semiconductors. In particular, XRD is central to evaluate the chemical composition and strain of GeSn alloys, which are crucial parameters affecting the band structure. The next chapter demonstrates that these two parameters can also be extracted for films and microstructures by employing Raman spectroscopy.

CHAPTER 4 GERMANIUM-TIN RAMAN VIBRATIONAL MODES

A deep understanding of the vibrational modes is required to consider using Raman spectroscopy as a reliable characterization technique for GeSn alloys. However, almost all previous studies focused on the effect of either Sn composition or strain for the main Ge-Ge peak. The objective of the current chapter is to thoroughly investigate the behavior of Ge-Ge, DA, Ge-Sn, as well as Sn-Sn like vibrational modes as a function of both Sn composition and strain. The decoupling of the two contributions was made possible using both pseudomorphic and relaxed layers with Sn contents in the $5\,\text{at.\%} - 17\,\text{at.\%}$ range.

4.1 Growth of GeSn samples

The investigated GeSn samples were grown on $0.6\,\mu\text{m} - 1.1\,\mu\text{m}$-thick Ge-VS on 4-inch Si (100) wafers. The Sn content (y), the residual in-plane strain

$$\varepsilon = \frac{a_{\parallel} - a_0}{a_0} \tag{4.1}$$

and the degree of strain relaxation

$$r = \frac{a_{\parallel}^{GeSn} - a_{\parallel}^{Ge-VS}}{a_0^{GeSn} - a_{\parallel}^{Ge-VS}} \tag{4.2}$$

for all layers listed in table 4.1 were estimated from high-resolution XRD RSM measurements. Two sets of pseudomorphic and relaxed GeSn layers were investigated in this study, in addition to layers with intermediate strain relaxation. For the pseudomorphic GeSn series, a 4.0 at.% BL was first grown at 350 °C, then the temperature was decreased to grow the TL at a higher Sn content in the $9\,\text{at.\%} - 13\,\text{at.\%}$ range (samples A-D). The other parameters were kept constant during growth. Figure 4.1(a) exhibits a typical scanning TEM (STEM) image for sample D with a 50 nm-thick TL (13 at.%) on a 45 nm-thick BL (4 at.%). The corresponding RSM map in figure 4.1(b) shows that GeSn BL and TL are pseudomorphic with respect to the Ge-VS, corresponding to a relaxation below 5 %. Similar relaxations were estimated for all samples regardless of growth temperature. The presence of interference fringes in figure 4.1(b), also observed in the $2\theta - \omega$ scan around the (004) XRD order[1], indicates a high degree of crystallinity.

[1]The planes are grown parallel to the (001) substrate, and lower orders (001), (002) and (003) produce no diffraction peak because the structure factor is zero (systematic extinctions).

Table 4.1 List of samples investigated in this work. The growth temperature T, the composition and strain values as estimated from XRD and Raman measurements are shown, as well as parameters extracted from the fits.

Sample		T (°C)	y_{XRD} (at.%)	y_{Raman} (at.%)	ε_{XRD} (%)	ε_{Raman} (%)	ω_{Sn-Sn} (cm^{-1})	ω_{Ge-Sn} (cm^{-1})	ω_{DA} (cm^{-1})	ω_{Ge-Ge} (cm^{-1})	t_{Ge-Ge} (cm^{-1})
Pseudo-morphic	A	310	8.8	9.3	-1.17	-1.30	182.9	260.2	290.7	299.0	1.59
	B	300	10.6	10.1	-1.39	-1.40	181.5	259.4	291.2	298.8	1.65
	C	290	12.0	11.8	-1.60	-1.64	180.8	258.8	291.4	298.6	1.76
	D	280	13.0	13.3	-1.79	-1.84	179.8	258.6	291.7	298.3	1.86
Relaxed	E	330	6.8	7.1	-0.14	-0.19	181.9	256.6	288.9	295.4	1.41
	F	320	8.8	8.3	-0.25	-0.13	179.7	255.5	288.0	294.1	1.48
	G	310	10.9	11.4	-0.30	-0.41	178.1	254.8	287.0	292.9	1.68
	H	300	13.2	13.2	-0.39	-0.51	176.3	254.5	286.6	291.9	1.79
Other	I	340	4.6	4.1	-0.23	-0.03	183.2	259.2	289.4	297.2	1.22
	J	300	13.3	13.2	-0.33	-0.36	175.1	254.3	286.1	291.1	1.78
	K	280	15.4	16.1	-1.17	-1.32	175.6	254.9	287.9	293.4	2.00
	L	280	16.0	16.1	-1.41	-1.25	175.2	254.8	287.8	293.1	2.00
	M	280	16.1	17.2	-1.16	-1.38	175.0	254.5	287.4	292.8	2.07
	N	280	16.9	14.9	-1.27	-0.85	173.7	254.1	287.4	292.1	1.90

For the relaxed series, 500 nm − 700 nm-thick GeSn layers were grown at a fixed temperature in the 330 °C − 300 °C range, leading to a composition in the 7 at.% − 13 at.% range (samples E-H). In the TEM image for a 13 at.% Sn layer (figure 4.1(c)) dislocations are mainly observed within the first 200 nm − 300 nm of the GeSn layer [41]. The associated RSM map shows strong broadening along q_X resulting from plastic relaxation (figure 4.1(d)), with an estimated relaxation exceeding 75 % in all samples (figure 4.1(e)). The reduced compositional grading at thicknesses above 300 nm leads to a uniform strain and composition profile. The Sn content for pseudomorphic and relaxed sets are plotted in figure 4.1(f) as a function of growth temperature T. An increase in Sn content of 1.3 ± 0.3 at.% for every 10 °C decrease in growth temperature is observed for pseudomorphic samples, while a higher rate of 2.1 ± 0.2 at.%/ − 10 °C is estimated for relaxed layers, resulting from enhanced strain minimization during growth [41, 53]. In addition to pseudomorphic and relaxed sets of samples described above, Raman analysis was extended to six other samples of various values of strain and composition (table 4.1).

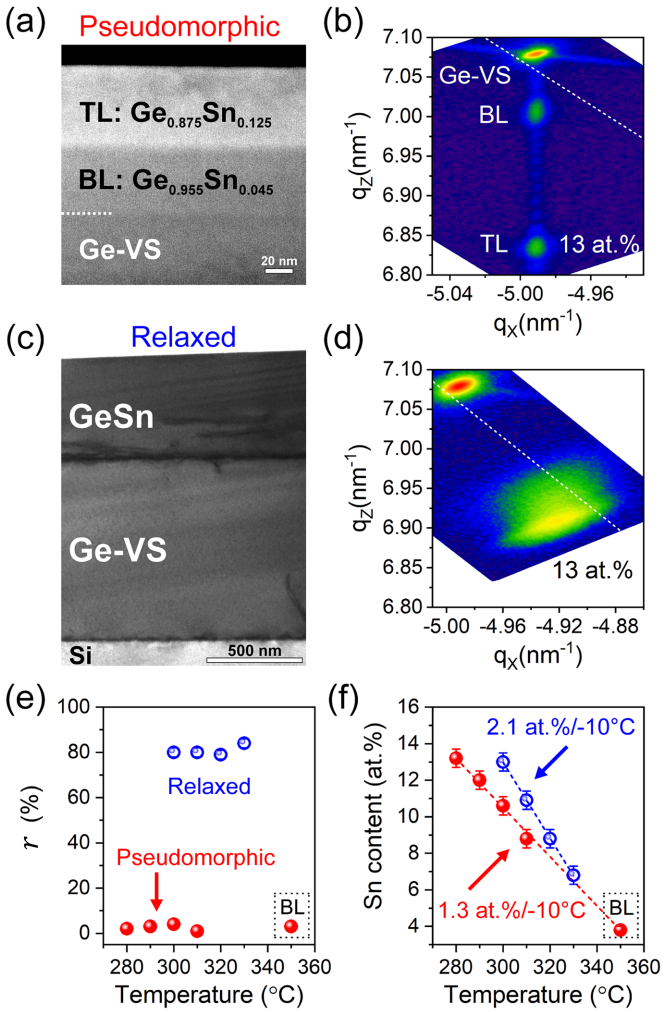

Figure 4.1 Pseudomorphic and relaxed GeSn sets of samples. (a-b) STEM image (a) and RSM around the asymmetrical (224) reflection (b) for the pseudomorphic sample D. (c-d) TEM image (c) and RSM map (d) for the relaxed sample H. (e-f) Relaxation ratio (e) and Sn content (f) as a function of the growth temperature.

4.2 Fitting procedure

While Voigt or Lorentzian [57] functions are commonly used to fit Raman peaks, they cannot reproduce the asymmetric behavior that is typical to Raman modes of semiconductor alloys [134, 155]. This asymmetry is due to alloying as the substitution of Sn atoms in the lattice breaks the translational symmetry and leads to a relaxation of the $\vec{q} = \vec{0}$ momentum selection rule [156]. To better reproduce the line shape of LO modes, exponentially modified

gaussian (EMG) functions [35, 157]

$$I(\omega) = I_0 + \frac{A}{2t} \exp\left(\frac{1}{2}\left(\frac{W}{t}\right)^2 + \frac{\omega - \omega_c}{t}\right)\left(\mathrm{erf}\left(-\frac{\omega - \omega_c}{\sqrt{2}W} - \frac{W}{\sqrt{2}t}\right) + 1\right) \tag{4.3}$$

were employed. Here, I_0 is an offset, A represents the peak area, W its width and t is related to its asymmetry. For an asymmetric profile, the central frequency ω_c is different than the frequency at which the peak reaches its maximal value. Note that extracted peak positions correspond to wavenumbers of maximal intensity. For the Ge-Ge, Ge-Sn and DA modes, the fitting procedure was performed on the $200\,\mathrm{cm}^{-1} - 360\,\mathrm{cm}^{-1}$ range. After removal of the baseline, the line shape was fitted with three EMG functions. The Sn-Sn like mode was fitted with a single EMG.

4.3 Identification and quantitative behavior of the Raman modes

Micro Raman scattering spectroscopy was performed with a 633 nm laser. In other studies, the use of shorter wavelength laser was sometimes justified by the need for a shallower penetration depth to avoid the background signal from underlying Ge or GeSn buffer layers [132]. This is not a concern here even when a 633 nm excitation laser is used. Indeed, thicknesses measured from transmission electron microscopy (TEM) are larger than the laser penetration depth estimated from ellipsometry ($\approx 30\,\mathrm{nm}$ for $y = 10\,\mathrm{at.\%}$), meaning that a negligible contribution from the underlying layers to the measured Raman signal is expected. Thus, in partially relaxed layers only the top region of the sample with a uniform composition is probed by the laser.

Figure 4.2(a-b) displays representative polarized Raman spectra, recorded for sample F ($y = 8.8\,\mathrm{at.\%}$, $\varepsilon = -0.25\,\%$). For comparison, polarized Raman spectra of a Ge-VS are also displayed in figure 4.2(c). For both samples, the main Ge-Ge mode ($\approx 300\,\mathrm{cm}^{-1}$) is much stronger under $x(z'z')\bar{x}$ and $x(zy)\bar{x}$ configurations as compared to $x(zz)\bar{x}$ and $x(z'y')\bar{x}$ configurations, which is consistent with the selection rules of LO phonons. For the GeSn layer, the Ge-Sn LO mode [35, 130] (dotted vertical line) shows the same behavior. The shoulder visible on the low wavenumber side of the Ge-Ge peak (dashed vertical line) is related to a DA mode attributed to a maximum in the one-phonon density of states in Ge [35, 158, 159]. Its presence becomes more apparent under $x(zz)\bar{x}$ configuration because of the low intensity of both adjacent LO modes. This additional contribution is accounted for in the fit of Raman spectra, which provides an accurate identification of the characteristics of each mode. An example of a fitted unpolarized spectrum is displayed in figure 4.2(d). In addition, second-order Ge-Ge modes are also detected in $x(z'z')\bar{x}$ and $x(zz)\bar{x}$ configurations

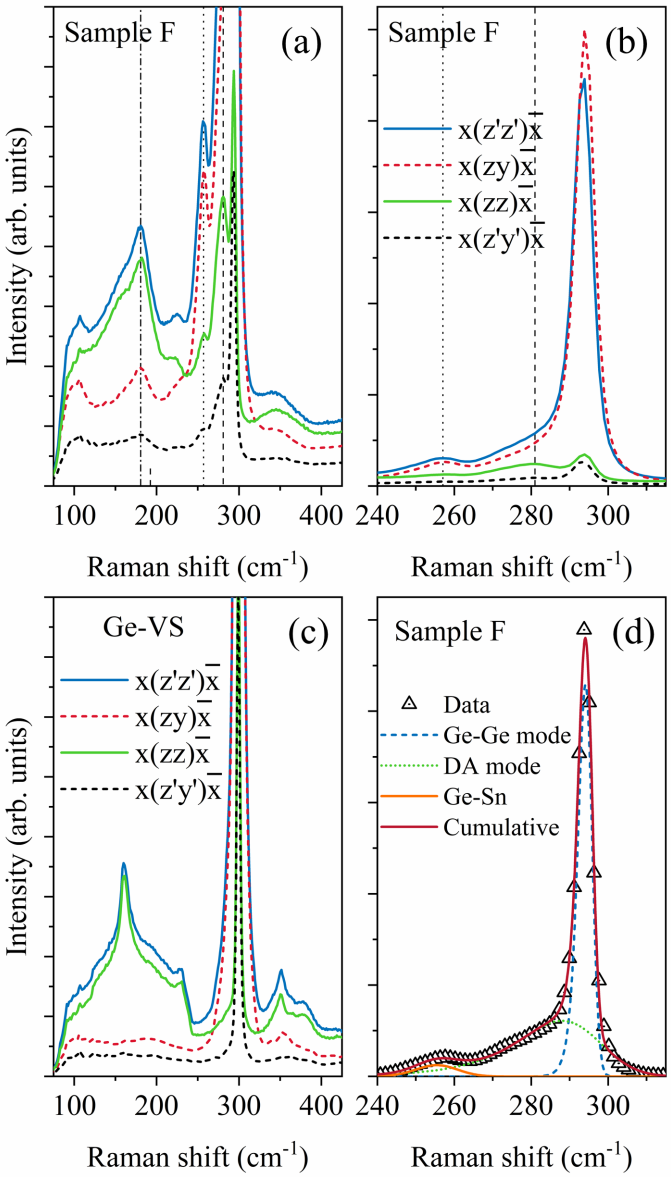

Figure 4.2 (a-b-c) Raman signal of GeSn (sample F) (a-b) and Ge-VS (c) for different polarizations. (d) Fit of the Ge-Ge, DA, and Ge-Sn modes for sample F. The coefficient of determination R^2 is between 0.9962 and 0.9994 for all samples.

for the Ge-VS (2TA between 100 cm^{-1} and 250 cm^{-1} [130, 160], TO+TA near 350 cm^{-1} and 2LA near 380 cm^{-1} [161]). These modes also appear with the same selection rules in the GeSn sample, as well as an additional mode near 180 cm^{-1} (dash-dotted vertical line). Since this peak doesn't follow the selection rules of a LO mode, it cannot be straightforwardly assigned to the Sn-Sn mode expected near this frequency [162, 163]. The small intensity of Sn-Sn vibrations, if present, is believed to be hindered by another mode, attributed to a DA peak, because its frequency coincides with a maximum in the phonon density of states of

Ge [35, 159, 164] and its intensity for the different polarizations changes in a similar fashion as for the DA peak near 280 cm^{-1}. For this reason, we refer to this mode as Sn-Sn like, in concordance with references [35, 130].

Raman spectra of pseudomorphic and relaxed GeSn samples with variable Sn compositions are displayed in figure 4.3. Interestingly, as Sn content increases, the peak positions in pseudomorphic layers remain almost unaffected by the change in Sn content (4.3(a)), whereas a progressive shift to lower wavenumbers is observed for both modes in relaxed layers (4.3(b)). Due to the relatively larger atomic mass of Sn, when a significant amount of Sn atoms is incorporated into the Ge lattice, a downshift of the Ge-Ge and Ge-Sn modes is expected. This behavior is visible in relaxed layers, while in pseudomorphic layers this anticipated downshift is counterbalanced by the upshift associated with the increased compressive strain due to the higher Sn content in the lattice.

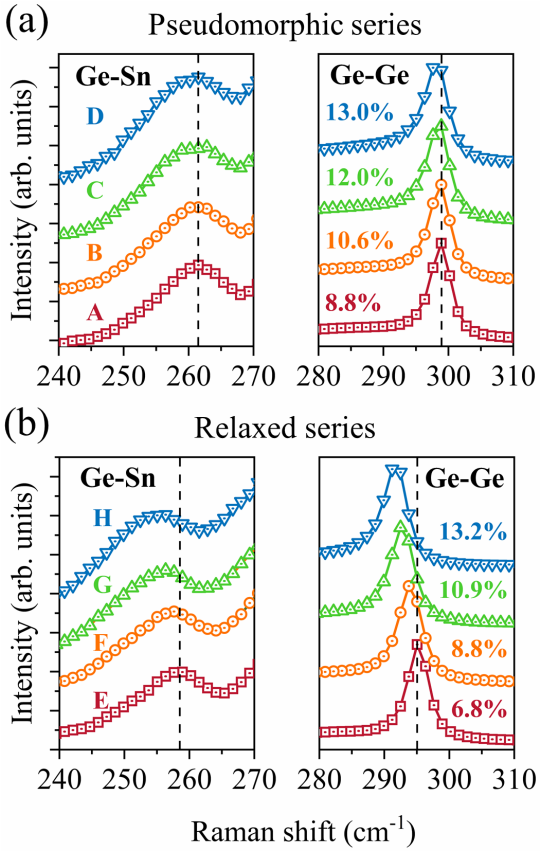

Figure 4.3 Ge-Sn and Ge-Ge modes recorded for pseudomorphic (a) and relaxed (b) series

4.4 Decoupling of strain and composition effects

Examples of three-dimensional plots of the Raman shifts ω (black spheres) for Ge-Ge and Ge-Sn modes as a function of Sn content and strain are shown in figure 4.4(a-b). The measured data points belong to the same planes, which can be described by two-dimensional linear regressions

$$\omega = \omega_0 + ay + b\varepsilon \tag{4.4}$$

where ω_0 is a characteristic wavenumber, and a and b are fitting parameters. The linear behavior is expected from phonon deformation potential theory [111]. Resulting fits, superimposed on the scatter plots, and the projections on the 2D space in figure 4.4(c-d) confirm

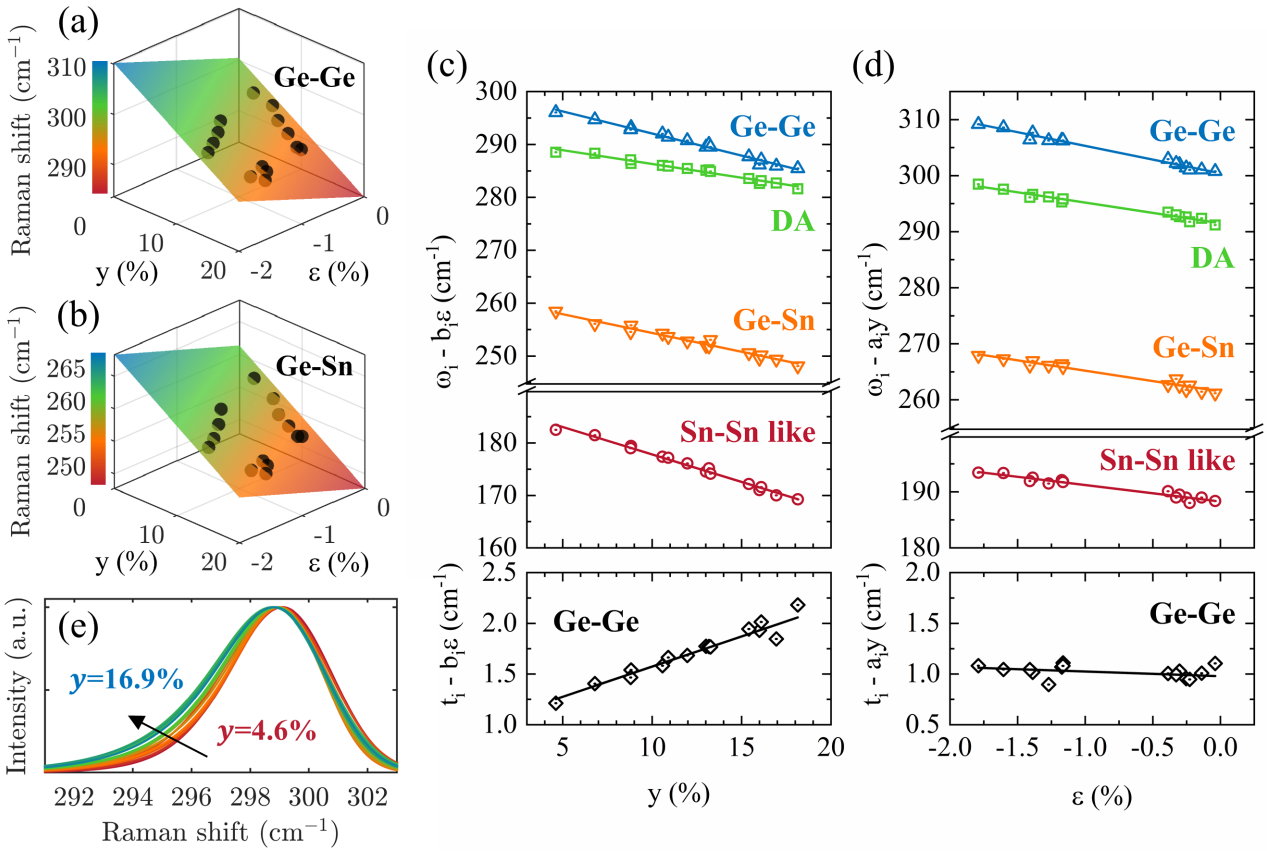

Figure 4.4 Fit results. (a-b) Planar regressions for the position of Ge-Ge (a) and Ge-Sn (b) modes. (c-d) Projections of planar regressions for the four modes in a 2D space. The vertical axis corresponds to the Raman shift (or the asymmetry parameter) corrected with the effect of strain (c) or composition (d). The subscript i is a placeholder for the names of the modes. The lines correspond to side views of the planes. (e) Normalized Ge-Ge modes for increasing Sn contents. All functions were plotted with $\omega_c = 300\,\mathrm{cm}^{-1}$ for comparison purposes.

that the linear regressions accurately represent the behavior of the four peaks in all studied samples. Fitting coefficients are listed in table 4.2 and errors are calculated considering 95 % confidence intervals. R^2 being larger than 0.94 and the relatively small errors on both a and b slopes indicate that the planar fits describe adequately the modes distributions. Furthermore, the calculated $\omega_{0,Ge-Ge}$ is equal to the value obtained for bulk Ge and a and b slopes are comparable to those found in earlier studies for the Ge-Ge mode [57, 134]. As for the Ge-Sn mode, a and b values are slightly higher than those of Ge-Ge mode. However, the slopes of all four peaks are remarkably close and sometimes overlap when considering the uncertainties.

The behavior of the integrated intensity, width, and asymmetry of each one of these vibrational modes was also evaluated. We found that an increase in Sn content is associated with an increase in the relative integrated intensity of the Ge-Sn and DA modes. The latter also increases as layers become more compressively strained. Furthermore, we also noticed that the full width at half maximum (FWHM) of both Ge-Ge and Ge-Sn peaks increase with higher Sn content and higher relaxation, as expected from the increase in lattice disorder. As for t of the Ge-Ge peak, included in table 4.2, it increases with Sn content with a relatively strong correlation ($R^2 = 0.9533$), as shown in figure 4.4(c). The strain, however, has no measurable impact on t (figure 4.4(d)). The increasing asymmetry of the Ge-Ge mode due to Sn incorporation is visible in figure 4.4(e). This explains why the DA peak is less prominent for samples with high Sn contents. The increase of the Ge-Ge peak asymmetry, together with a shift of the peak position to lower wavenumbers, results in a larger superimposition of the two contributions. Nevertheless, this superimposition remains partial and it is still possible to discriminate them, as confirmed by the high R^2 obtained in the two-dimensional linear regressions.

Table 4.2 Results of the two-dimensional linear regressions performed for the position of each mode and for the asymmetry parameter of the Ge-Ge peak.

Regression	ω_0 or t_0 (cm^{-1})	a (cm^{-1})	b (cm^{-1})	R^2
ω_{Ge-Ge}	300.4 ± 0.9	-84 ± 8	-491 ± 52	0.9820
ω_{DA}	291.3 ± 0.7	-49 ± 7	-347 ± 45	0.9685
ω_{Ge-Sn}	261 ± 1	-68 ± 11	-347 ± 69	0.9485
ω_{Sn-Sn}	188 ± 1	-104 ± 9	-292 ± 59	0.9822
t_{Ge-Ge}	1.0 ± 0.1	6 ± 1	-5 ± 7	0.9533

4.5 Framework for the extraction of Sn composition and strain

Any pair of equations describing peak positions as a function of y and ε would technically be sufficient to estimate composition and strain of a GeSn layer based on its Raman spectrum. However, since positions of all modes evolve similarly, this becomes challenging based solely on peak positions. In fact, due to comparable a and b slopes, the strain and composition estimation obtained when solving equations (4.4) for a pair of peaks will be highly dependent on small changes in the input parameters ω. However, as previously stated, composition and strain also affect peak areas, widths, and asymmetry. For instance, the two-dimensional linear regression of t_{Ge-Ge} results in a and b coefficients that are very different from those obtained for peak positions (table 4.2). Therefore, composition and strain of GeSn alloys can be extracted directly by solving a set of two equations describing the behavior of the peak position and asymmetry of the main Ge-Ge mode

$$\omega_{Ge-Ge} = \omega_{0,Ge-Ge} + a^{\omega}_{Ge-Ge} y + b^{\omega}_{Ge-Ge} \varepsilon \tag{4.5}$$

$$t_{Ge-Ge} = t_{0,Ge-Ge} + a^{t}_{Ge-Ge} y + b^{t}_{Ge-Ge} \varepsilon \tag{4.6}$$

This approach allowed to retrieve values which are close to those measured by XRD, as shown in table 4.1. This is a clear demonstration that combining peak position and asymmetry is sufficient for an accurate analysis of strain and composition in GeSn semiconductors using Raman spectroscopy. To test this approach, Raman line-scans were carried out on under-etched GeSn microdisks (not shown). The model enabled the evaluation of the bulk composition with an accuracy of 5 at.% in addition to providing the local residual strain across the microdisks, thus clearly demonstrating the relevance of micro Raman spectroscopy to probe local composition and strain in individual GeSn micro-structures.

CHAPTER 5 MODELING OF THE OPTICAL PROPERTIES OF GERMANIUM-TIN NANOPILLAR ARRAYS

Engineering light absorption in GeSn structures is crucial to enhance their basic device performance for a variety of applications such as photodetectors and solar cells. With this perspective, this chapter outlines our effort to understand the interplay between dimension and light absorption. It is well-established that texturing a surface to reduce its reflectivity is a key strategy to tune the optical properties. For instance, etching Si to form nanostructured black Si allows to increase the conversion efficiency of photovoltaic devices [165]. Similarly, the fabrication of vertically aligned carbon nanotube arrays results in record-breaking low reflectance materials (0.045 %) [166]. Moreover, tapered nanostructures are even found on moth eyes to maximize the amount of detected light [167].

Incident light on a surface is either reflected or transmitted. According to equation (2.2), a larger difference between refractive indices at the interface results in a greater reflection. Since semiconductors typically have large refractive indices [92], this limits the efficiency of planar photodetectors. The central idea of this chapter is to improve the coupling of the incident light into the GeSn active region and therefore to increase its absorptance. However, since GeSn layers have finite thicknesses, optimizing the performance requires a balance between removing matter to structure the interface while still preserving enough of the absorbing material. In this regard, the effect of key geometrical parameters on the overall absorptance of GeSn nanopillar arrays is studied via FDTD simulations. Their properties are compared with those of GeSn thin films obtained analytically by the transfer matrix method. More specifically, the nanopillars diameter (d), pitch (u), height (h) will be addressed, as well as the dependence on wavelength (λ) and angle of incidence (θ), for samples of different Sn contents. Note that the Si wafer was ignored in the simulations at this point, since it is transparent above $\lambda = 1.1\,\mu m$. Interference fringes associated with a thick Si layer would impede the detection of trends.

5.1 GeSn n and k

Simulations were conducted using optical constants n and k of GeSn layers with $y = 10\,\text{at.}\%$ and $y = 14\,\text{at.}\%$ Sn contents. These were extracted from ellipsometry measurements and are displayed in figure 5.1. As expected, a higher Sn content is associated with an increased absorption ($\propto k$) and slightly shifted to longer wavelengths. Constants for Ge are from Palik [168]. Simulations focused on the region of higher absorption $1.6\,\mu m - 3.2\,\mu m$ given

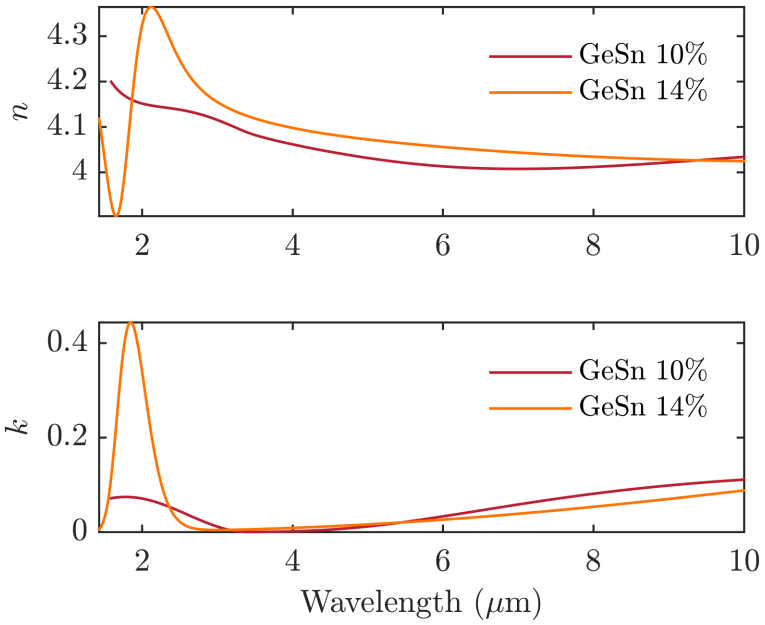

Figure 5.1 Measured refractive indices of GeSn layers in the infrared range

its relevance for applications mentioned in section 2 and the availability of characterization techniques for comparison with experimental data.

Figure 5.2 shows the optical properties of 1 µm-thick GeSn films calculated using optical constants of figure 5.1. Reflectance is constant at almost 40 % throughout the range in both cases. Unsurprisingly, the absorptance is reduced for longer wavelengths, which translates as an increased transmittance. Fundamentally, the idea of structuring the layer into nanopillars

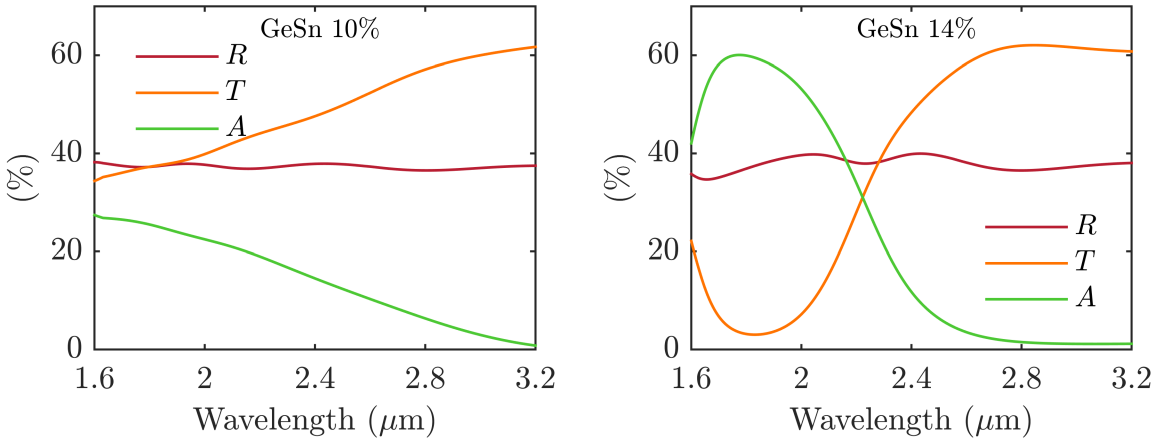

Figure 5.2 Optical properties of 1 µm-thick GeSn films deposited on Ge

is to lower the reflectance so that a larger fraction of the light passes through the layer and interacts with the absorbing material.

5.2 Effect of pattern geometry for 10 at.% GeSn

The pattern geometry is defined on the EBL mask before the etching procedure. This includes parameters such as the nanopillars shape and size, as well as the array type and nanopillars spacing (the pitch). In this section, we consider 1 µm-long cylindrical pillars of various diameters forming square and hexagonal arrays with a large range of pitches.

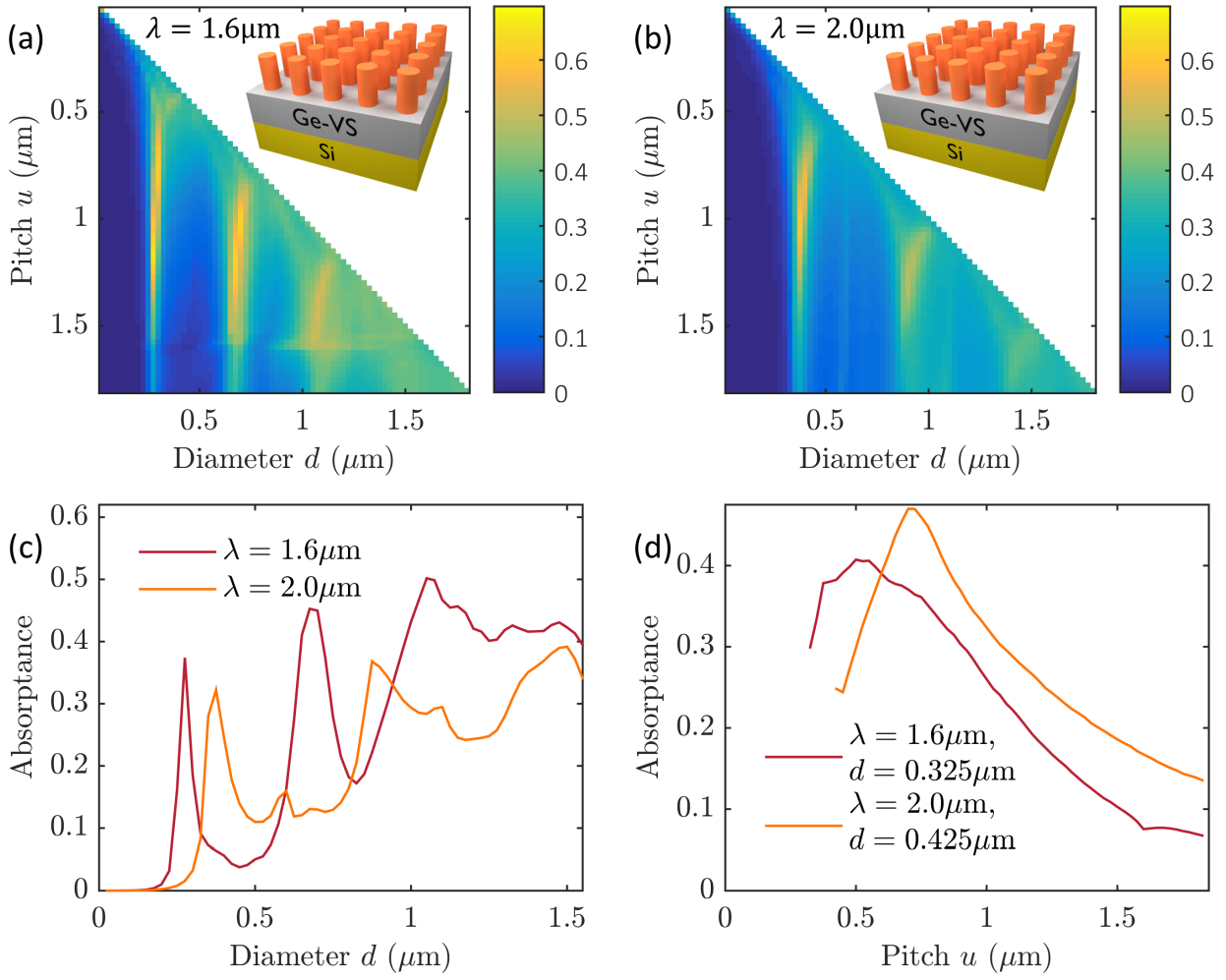

Figure 5.3 Effect of diameter and pitch on the absorptance of 1 µm-long 10 at.% GeSn pillar square arrays. 2D mapping for (a) $\lambda = 1.6\,\mu$m and (b) $\lambda = 2.0\,\mu$m incident light. (c) Diameter dependence ($u = 1.55\,\mu$m). (d) Pitch dependence.

First, the combined effect of diameter and pitch has been studied for square arrays of figure 3.2(a-b). The absorptance maps obtained are displayed in figure 5.3(a-b). The validity of calculations can be assessed notably by analyzing both $d \ll u$ and $d \gg u$ regimes. FDTD yields respectively $A = 7.946 \times 10^{-5}$ and $A = 0.269$ at $\lambda = 1.6\,\mu\text{m}$, whereas the transfer matrix method gives $A = 0.0128$ for a single Ge layer and $A = 0.274$ for a GeSn/Ge stack. While the agreement is very good in the second regime, the difference observed between absorptance values in the first regime are due to distinct interpolation methods used in FDTD and analytical calculations. Since the wavelengths in the Ge dataset from Palik are $\approx 100\,\text{nm}$ apart in the SWIR, the interpolation method can affect k values which are close to 0. However, this has a very limited impact on the overall absorptance of the arrays since k values of GeSn are larger by many orders of magnitude. The pillars are responsible for practically all the absorption, while Ge is virtually transparent over $\lambda = 1.6\,\mu\text{m}$.

Maximal absorptances of 65.9 % and 59.6 % are achieved at $\lambda = 1.6\,\mu\text{m}$ and $\lambda = 2.0\,\mu\text{m}$ respectively. This is more than twice the values obtained for GeSn thin films (27.4 % and 22.1 %), which demonstrates the relevance of structuring to improve the performance of optical devices. However, one key observation is that the absorptance is enhanced for specific diameters only, for which light couples more effectively into the array. These resonance modes occur for diameters separated by $\lambda/4$, as highlighted in figure 5.3(c). Following this argument, one would then expect to find an additional peak near $d = 1.5\,\mu\text{m}$ for $\lambda = 1.6\,\mu\text{m}$. In reality, the improved coupling is hindered by an increased reflection at the interface when the diameter becomes comparable to the pitch. The $\lambda/4$ spacing of resonance modes also means they appear at larger d for longer λ, as illustrated on figure 5.3(c). This has important consequences for spectral tunability, as discussed below. Peaks for $\lambda = 2\,\mu\text{m}$ reach lower absorptances because of the decrease in absorption coefficient ($\propto k$) with increasing wavelengths. As for the pitch, it has a minor impact on resonance modes, since they occur at similar d for increasing u. Still, the pitch has an important influence on the absorptance. For longer u, there is a smaller volume of GeSn, resulting in a progressive diminution of the absorptance, as shown in figure 5.3(d). In addition, simulations show a slight absorptance enhancement when $u = \lambda$, as observed in figure 5.3(a).

The resonance modes diameter-dependence means larger pillars absorb light at proportionally longer wavelengths, as exhibited in figure 5.4. For instance, the absorptance peak for 450 nm pillars reaches its maximum at 2.3 µm, or 0.6 µm further than for 300 nm pillars. This behavior could allow the design of tunable wavelength photodetectors. For even larger 575 nm diameters, the absorptance enhancement due to better coupling with the pillars compensates the reduction in k for longer wavelengths. This results in a leveling of the absorptance profile compared to bulk, which is more suited for broadband detection.

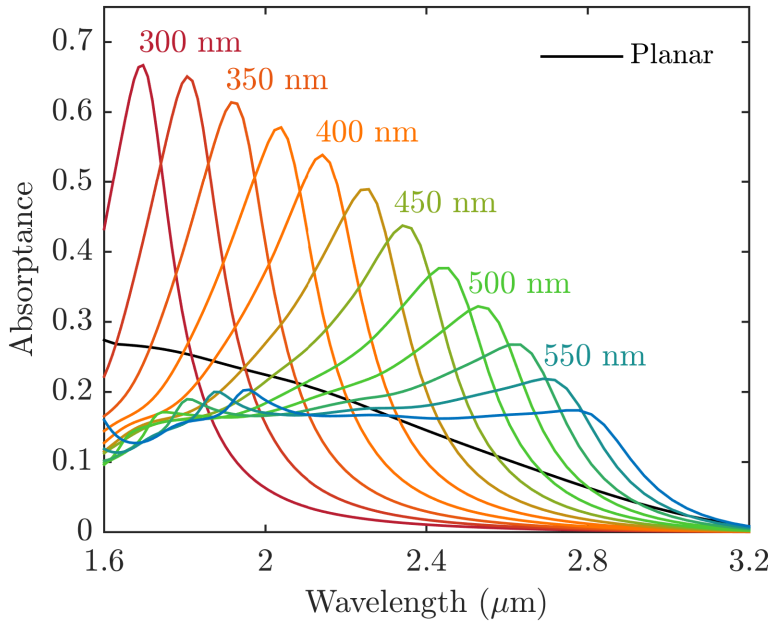

Figure 5.4 Spectral absorptance of 10 at.% GeSn pillar square arrays ($u = 1.1$ µm) compared with a thin film (planar geometry). Numbers refer to the pillars diameters.

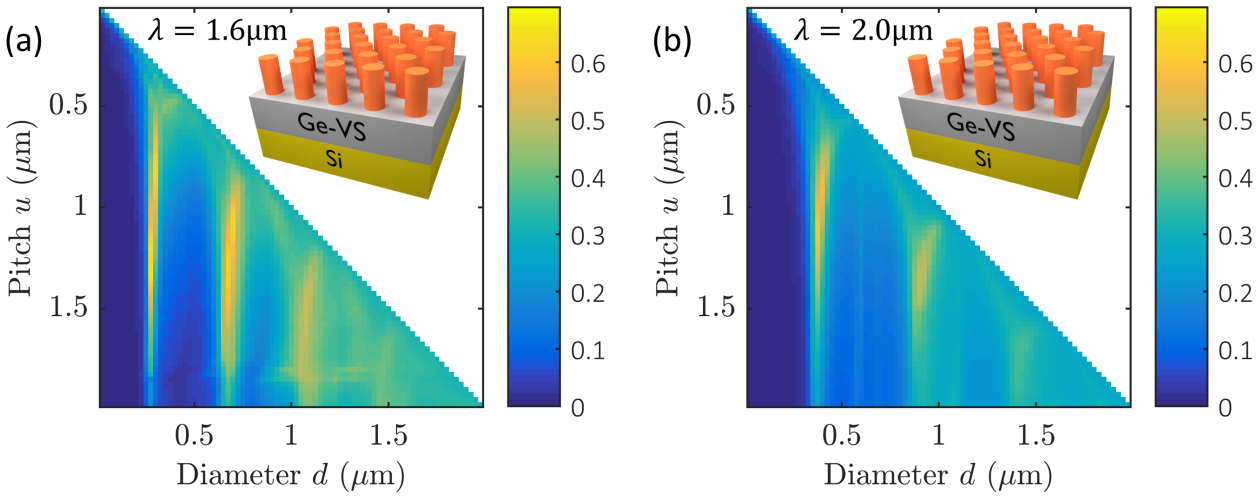

Figure 5.5 Effect of diameter and pitch on the absorptance of 1 µm-long 10 at.% GeSn pillar hexagonal arrays. 2D mapping for (a) $\lambda = 1.6$ µm and (b) $\lambda = 2.0$ µm incident light.

The aforementioned results were obtained considering square arrays. However, simulations performed over hexagonal arrays (figure 5.5) yield very similar values. For instance, resonance modes occur for identical diameters and absorptance maximums are within a 1 % margin.

In fact, this is consistent with the resonance modes low-dependence on the pitch. While the plane symmetry group doesn't have a major impact on the absorptance, the importance of the distance between pillars and the fill factor still apply.

5.3 Effect of pattern geometry for 14 at.% GeSn

Optical properties of 14 at.% GeSn nanopillar arrays were also calculated to evaluate the impact of Sn content. Absorptance maps in figure 5.6 show a similar behavior as those of 10 at.% GeSn pillars in figures 5.3 and 5.5, i.e. peaks corresponding to resonance modes and a decrease in intensity for longer pitches. Again, square and hexagonal arrays yield comparable results.

The main difference between 10 at.% and 14 at.% arrays is the wavelength dependence. For the latter, the absorptance maximum at $\lambda = 2.0\,\mu m$ (87.2 %) is higher than at $\lambda = 1.6\,\mu m$ (78.4 %). The opposite was observed in the case of 10 at.% nanopillars. This is consistent with the optical properties of thin films displayed in figure 5.2, where the maximal absorptance of 14 at.% GeSn is higher and reached at longer wavelengths than for 10 at.% GeSn. Absorptance values are summarized in table 5.1.

Table 5.1 Maximal absorptance of nanopillar arrays compared with thin films

Material	Wavelength	Thin film	Nanopillars	Difference	Ratio
GeSn 10 at.%	$\lambda = 1.60\,\mu m$	27.4%	65.9%	+38.5%	×2.41
	$\lambda = 2.03\,\mu m$	22.1%	59.6%	+37.5%	×2.70
GeSn 14 at.%	$\lambda = 1.60\,\mu m$	42.1%	78.4%	+36.3%	×1.86
	$\lambda = 2.03\,\mu m$	51.3%	87.2%	+35.9%	×1.70

Interestingly, the maximum improvement is between $36\,\% - 39\,\%$ in all cases, which corresponds to the reflectance of thin films in figure 5.2. While absorptances achieved are greater for 14 at.% than for 10 at.% GeSn pillars, the enhancement factor is slightly inferior ($< 2\times$) for the former, since the absolute gain in absorptance cannot surpass the loss of reflectance. This shows that structuring the layer into nanopillars is an effective way to absorb the power otherwise reflected by bulk layers.

The spectral absorptance of 14 at.% GeSn pillars arrays is displayed in figure 5.7. As opposed to 10 at.% GeSn pillars in figure 5.4, changing the diameter doesn't lead to a clear spectral tunability. In fact, the absorptance enhancement due to resonance modes is hindered by considerable changes of the absorption coefficient. A shift of peaks as observed in the case of

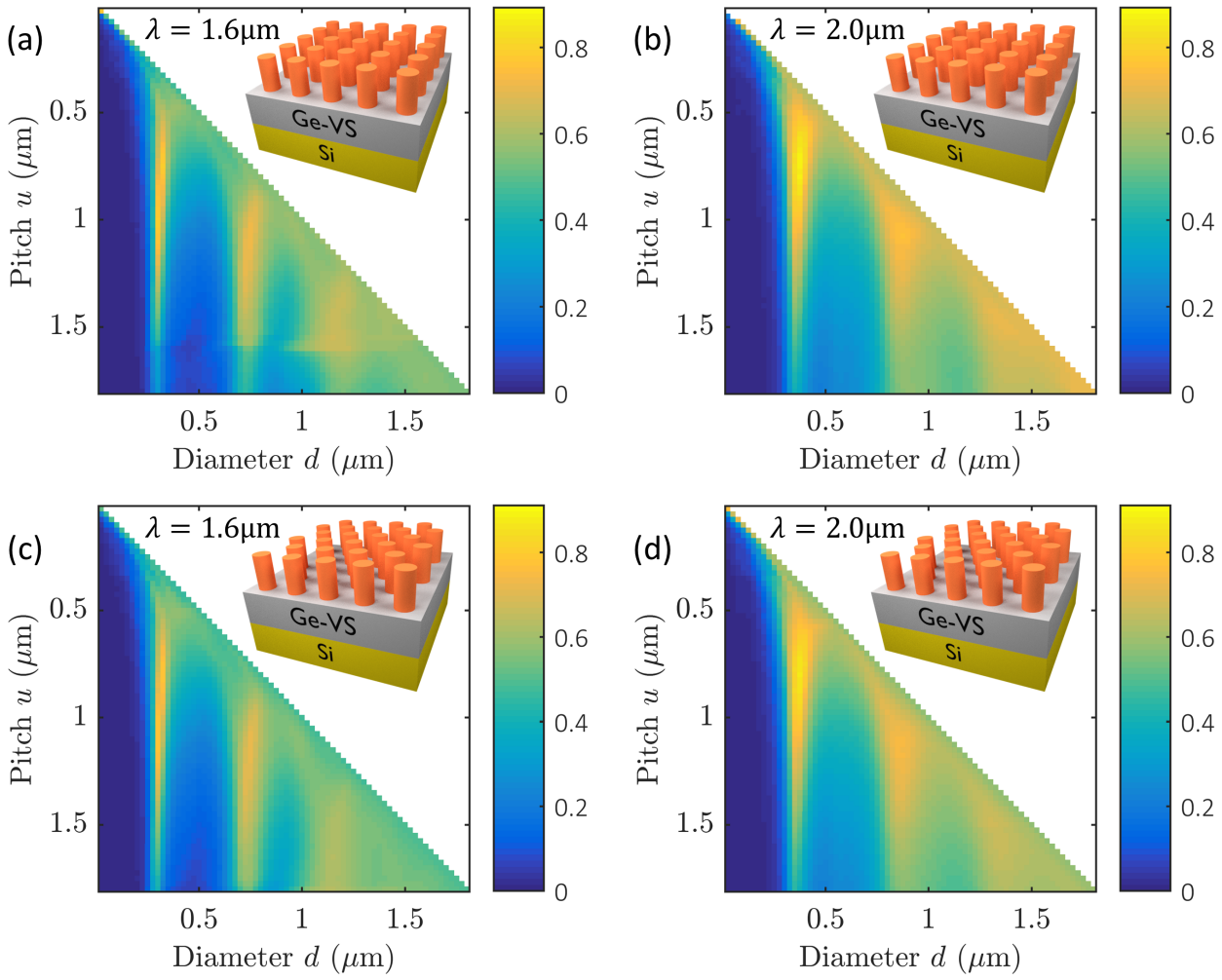

Figure 5.6 Effect of diameter and pitch on the absorptance of 1 µm-long 14 at.% GeSn pillar (a-b) square and (c-d) hexagonal arrays. 2D mapping for (a-c) $\lambda = 1.6$ µm and (b-d) $\lambda = 2.0$ µm incident light.

10 at.% GeSn pillars require constant or slowly varying k over the wavelength range. Nevertheless, structuring the layer into pillars is still relevant to increase the overall absorptance.

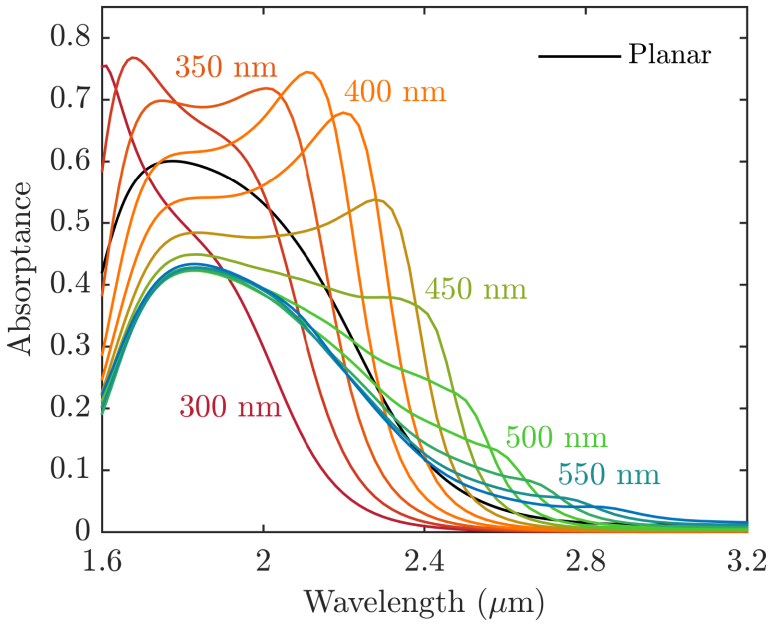

Figure 5.7 Spectral absorptance of 14 at.% GeSn pillar square arrays ($u = 1.1$ µm) compared with a thin film (planar geometry). Numbers refer to the pillars diameter.

5.4 Effect of height

Simulation results in previous sections showed a considerable absorptance enhancement when a 1 µm-thick GeSn layer is structured into cylindrical nanopillar arrays. The present section will address the impact of pillars height. Whereas the array pattern is defined by lithography, the pillars height is determined by the initial GeSn layer thickness and the etch depth.

5.4.1 Complete etch of the GeSn layer

The absorptance was evaluated for square arrays with pillars up to 4 µm-high. A pitch of 1.1 µm and a diameter of 350 nm were chosen to extend the analysis of resonance modes shown in figures 5.4 and 5.7. The progressive increase in absorptance is visible in figure 5.8, along with a comparison with a planar geometry.

As the thin film becomes thicker, the reflectance remains constant, while a progressively larger proportion of the light transmitted at the interface is absorbed in GeSn. This ultimately results in a practically null transmittance and a saturation of the absorptance at $\approx 60\,\%$. In the case of nanopillars, the progressive increase in height leads to a quick rise of the absorptance below $h \approx 1$ µm for both 10 at.% and 14 at.% GeSn. The augmentation rate diminishes above 1 µm and eventually a plateau is reached. The reduced reflectance means the

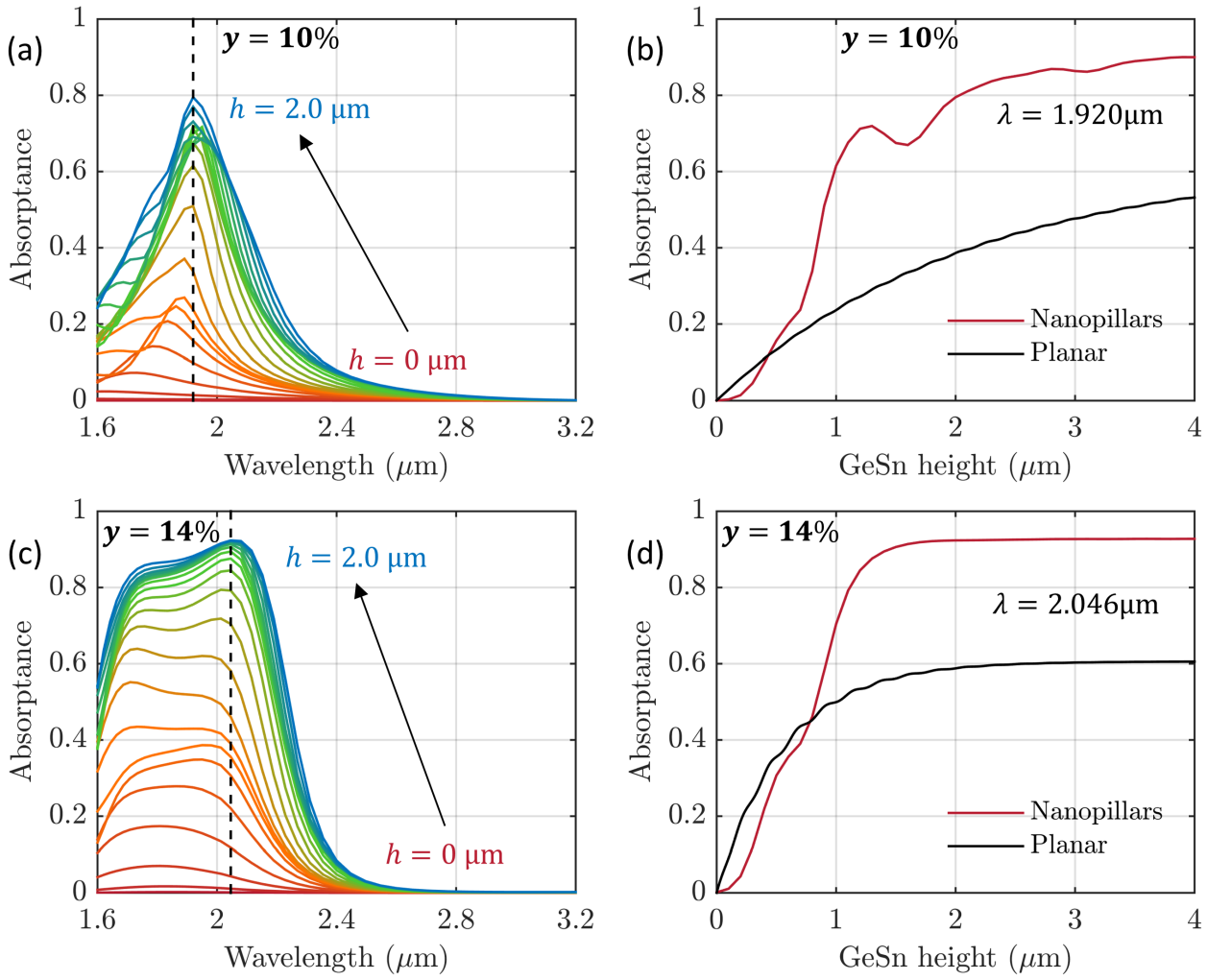

Figure 5.8 Absorptance as a function of pillars height ($u = 1.1\,\mu m$, $d = 350\,nm$). (a) Spectral absorptance of 10 at.% GeSn pillars. (b) Comparison with bulk at $\lambda = 1.920\,\mu m$ (dotted line in (a)). (c) Spectral absorptance of 14 at.% GeSn pillars. (d) Comparison with bulk at $\lambda = 2.046\,\mu m$ (dotted line in (c)).

saturation of the absorptance occurs at higher values of 90 %. While the maximal absorptance is the same for 10 at.% and 14 at.% GeSn, the plateau is reached for shorter pillars for the latter.

The rise of absorptance for nanopillar arrays can be better understood by analyzing its behavior for lower k, longer wavelengths regimes, such as $\lambda = 2.229\,\mu m$ in figure 5.9. For nanopillars, local maxima separated by $\approx 0.8\,\mu m$ are observed. This local enhancement presumably corresponds to the excitation of Fabry-Pérot modes in the vertical cavity. Indeed,

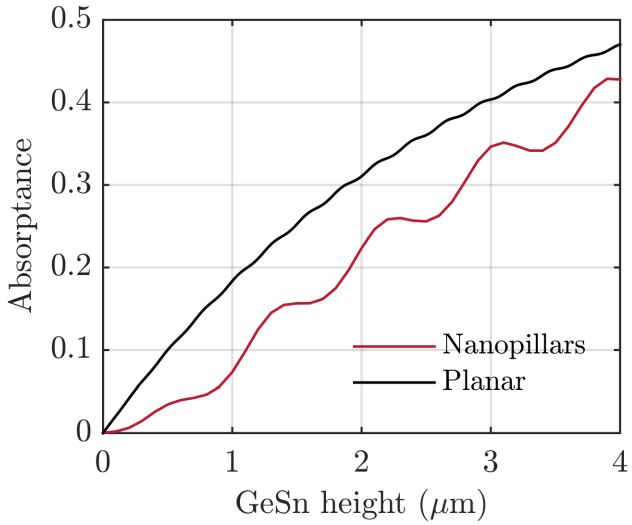

Figure 5.9 Absorptance of 10 at.% GeSn structures as a function of height at $\lambda = 2.229\,\mu\text{m}$ ($u = 1.1\,\mu\text{m}$, $d = 350\,\text{nm}$)

a new mode is allowed when the following condition is met

$$h = m\frac{\lambda}{2n_{eff}} \tag{5.1}$$

where $m \in \mathbb{N}^*$ and n_{eff} is the effective refractive index. For instance, modes located preferentially in air ($n = 1$) would be

$$\Delta h = \frac{\lambda}{2n_{eff}} = 1.11\,\mu\text{m} \tag{5.2}$$

apart. It is likely n_{eff} is in fact slightly higher, which would explain features observed in figures 5.9. The behavior of the nanopillars absorptance in figure 5.8(b,d), and especially the local maximum near $h = 1.3\,\mu\text{m}$ for 10 at.% GeSn then result from combination of Fabry-Pérot cavity modes and increased absorptance due to a larger absorption volume.

A similar reasoning can be applied to the interpretation of interference fringes observed for bulk 10 at.% GeSn layers ($n = 4.145$ at $\lambda = 2.229\,\mu\text{m}$). This yields $\Delta h = 0.269\,\mu\text{m}$, which corresponds to the shorter period mesured for oscillations on figure 5.9.

To sum up, structuring layers into nanopillars is thus relevant for thicknesses $\geq 1\,\mu\text{m}$, but this is only the case for combinations of (λ,d) corresponding to resonance modes. In other regimes (such as the one depicted in figure 5.9), higher h also improves the absorptance, but the performance of pillars doesn't necessarily surpass that of thin films. In addition,

structuring a layer with $h < 1\,\mu m$ does not improve significantly the absorptance.

5.4.2 Partial etch of the GeSn layer

Until now, pillars such as those in figure 3.2 have been considered, i.e. for which no GeSn remains between the pillars. In this section, the partial etching of the GeSn layer, as illustrated in figure 5.10(a), will be addressed. Simulations were performed for an initial 1 µm-thick GeSn layer. In the case of 10 at.% GeSn pillars, the partial etch of the layer results in intermediate

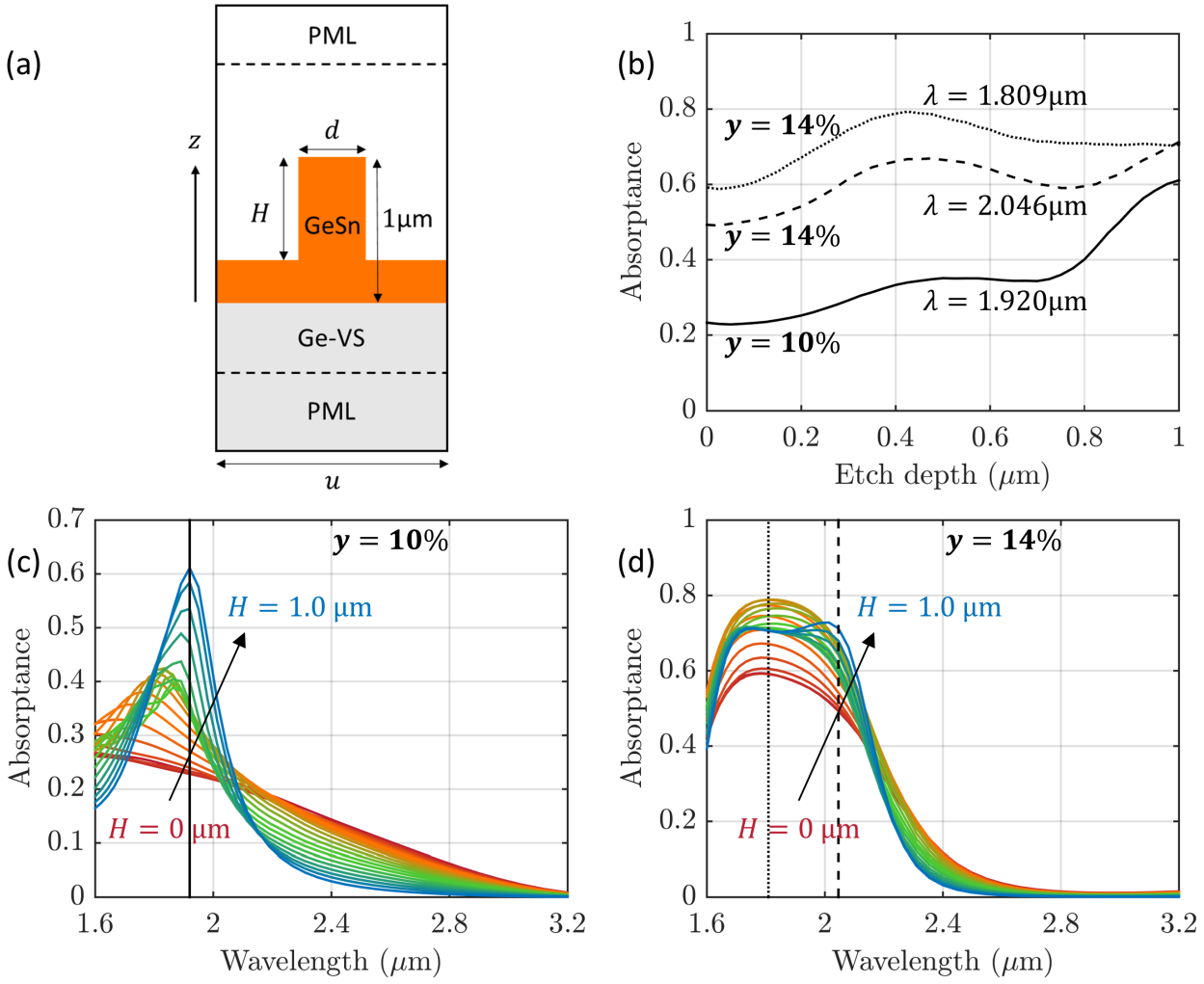

Figure 5.10 Absorptance as a function of etching depth for a 1 µm-thick film ($u = 1.1\,\mu m$, $d = 350\,nm$). (a) Side-view of the simulation domain. (b) Absorptance as a function of etching depth for specific wavelengths. (c-d) Spectral absorptance of (c) 10 at.% GeSn and (d) 14 at.% GeSn pillars. Vertical lines correspond to wavelengths indicated in (b).

absorptance between that of a 1 µm-thick film and 1 µm-high pillars, as shown in figure 5.10. The complete removal of GeSn between the pillars still offers the higher performance. The peak shift to longer wavelengths, also observed in figure 5.8(a), is thought to be only a matter of peak intensities: for increasing depths H, the absorption occurs preferentially at the resonance wavelength, and the loss of material diminishes the contribution of bulk to the overall absorptance.

For 14 at.% GeSn, the same behavior is observed at the resonance wavelength (dashed line for $\lambda = 2.046\,\mu m$), i.e. the absorptance maximum is reached for the deepest etch. However, this is not the case for off-resonance wavelengths (dotted line for $\lambda = 1.809\,\mu m$). This means a partial etch can be relevant to reduce reflection at the interface and increase the absorptance of a thin film.

5.5 Angular performance

As demonstrated above, structuring a GeSn layer into nanopillars is beneficial for the absorptance of light at a normal incidence. The impact of non-zero angles of incidence θ will now be addressed for the same specific geometry, i.e. a square array of pillars with a 350 nm diameter and a 1.1 µm pitch.

One could expect the pillars to preserve their advantage over bulk for steeper angles, since photons can be reflected towards other pillars. In reality, figure 5.11 shows the absorptance is highly dependent on the polarization. s-polarized light couples better with the nanopillar arrays than p-polarized light, whereas the opposite is observed for thin films. In this case, the absorptance of p-polarized light increases progressively until it reaches its maximum near the Brewster angle

$$\theta_B = \arctan\left(\frac{n_{GeSn}}{n_{air}}\right) \tag{5.3}$$

which is approximately $\theta_B = 77^\circ$ for both 10 at.% and 14 at.% GeSn near $\lambda = 2.0\,\mu m$. On the other hand, the absorptance of s-polarized light continually decreases from $\theta = 0^\circ$ to 90°. As a result, the advantage of pillars over bulk remains valid for increasing angles in the case of s-polarization, whereas a crossover is observed near $\theta = 40^\circ$ for p-polarization.

Numerical simulations presented in this chapter suggest a dramatic increase of the absorptance when a GeSn layer is structured into an array of nanopillars. In the next chapter, such arrays are microfabricated and their optical properties are measured to experimentally confirm this behavior.

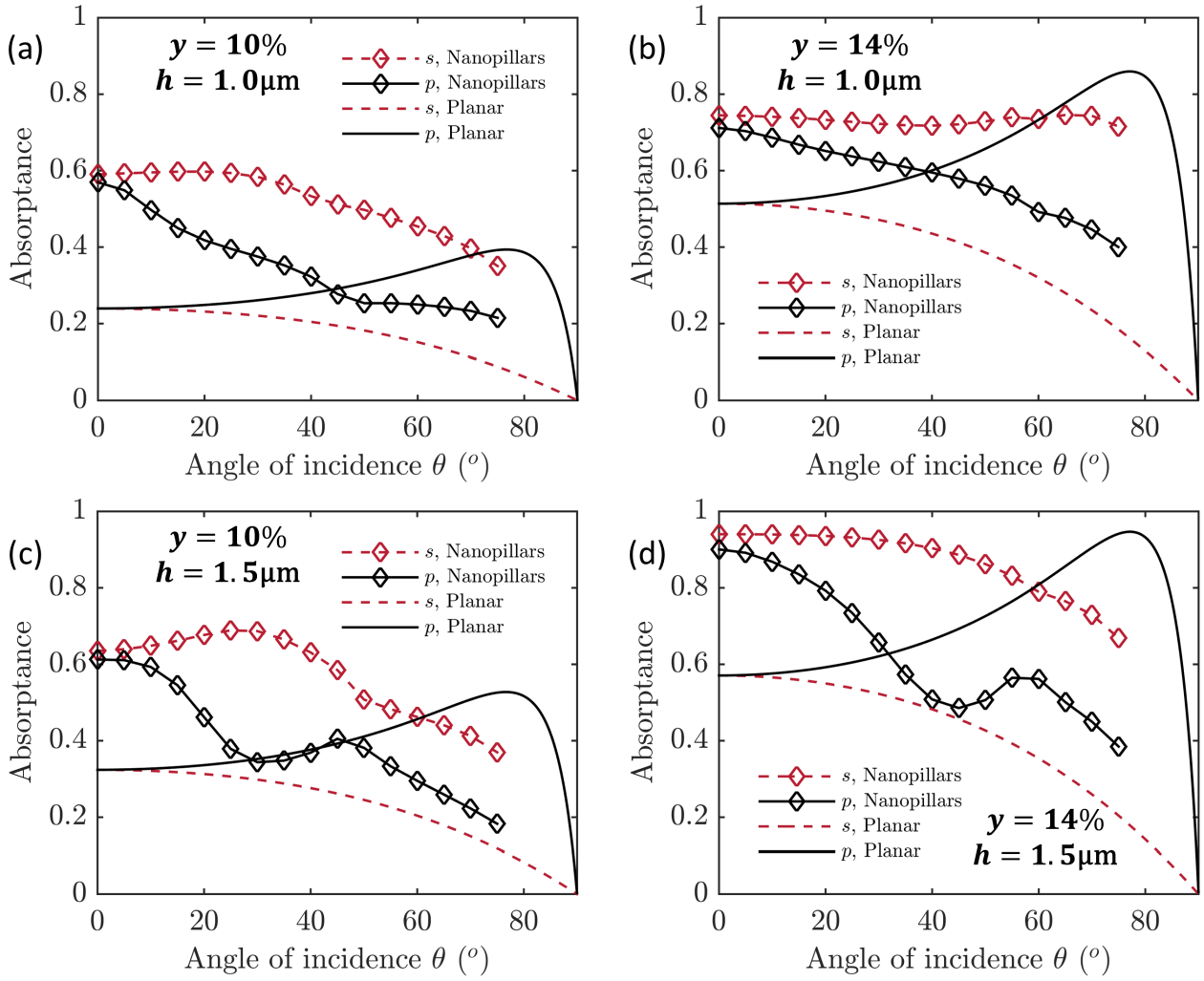

Figure 5.11 Absorptance as a function of angle of incidence ($u = 1.1\,\mu m$, $d = 350\,nm$). (a) 1.0 µm pillars in 10 at.% GeSn. (b) 1.0 µm pillars in 14 at.% GeSn. (c) 1.5 µm pillars in 10 at.% GeSn. (d) 1.5 µm pillars in 14 at.% GeSn.

CHAPTER 6 FABRICATION OF GERMANIUM-TIN MICROSTRUCTURES

In previous chapters, the microstructuring of GeSn layers was suggested to improve their optical properties. For instance, calculations in section 2.1 propose emission at even longer wavelengths can be achived via the release of strain. In this chapter, suspended microdisks are developed for this purpose. In addition, nanopillar arrays are fabricated to experimentally confirm the absorptance enhancement predicted in chapter 5.

6.1 GeSn nanopillars

6.1.1 Starting material

To allow for subsequent characterization with the spectrophotometer, both sides of the sample should be optically smooth to ensure specular reflection at the back interface. A double side polished Si(100) 4 inch wafer was thus used as a substrate for the epitaxy. A thick GeSn layer was grown at a constant temperature of 320 °C on a 1.3 µm Ge-VS. The progressive expansion of the lattice constant during the growth resulted in a grading of the Sn content, visible as a broadened GeSn peak at 65 ° in the XRD scan on figure 6.1(a). Two main regions of 6.8 at.% and 9.2 at.% were identified based on peak positions extracted from the RSM map on figure 6.1(b).

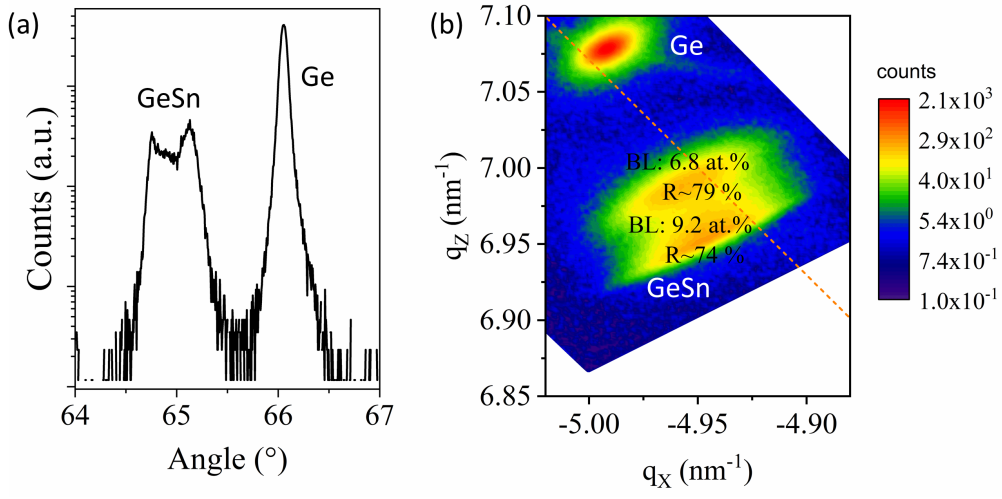

Figure 6.1 XRD scan (a) and RSM (b) for a thick GeSn layer on Ge on double side polished Si wafer

Table 6.1 Ellipsometry optical model and extracted thicknesses (†not measured)

Modeled layer	Thickness
Surface roughness	10.0 nm
GeO_2	1.49 nm
GeSn	1146 nm
Ge	1280 nm
Si	500 µm†

Ellipsometry characterization was performed to extract the optical constants of the GeSn layer and the thicknesses of the stack, displayed in table 6.1. This information, coupled with optical constants of Ge and Si from ref. [168], allowed the calculation of the sample's optical properties, showed in figure 6.2. There is quite a good agreement with those measured directly via spectrophotometry. The reflectance oscillates around 40 %, a value similar to

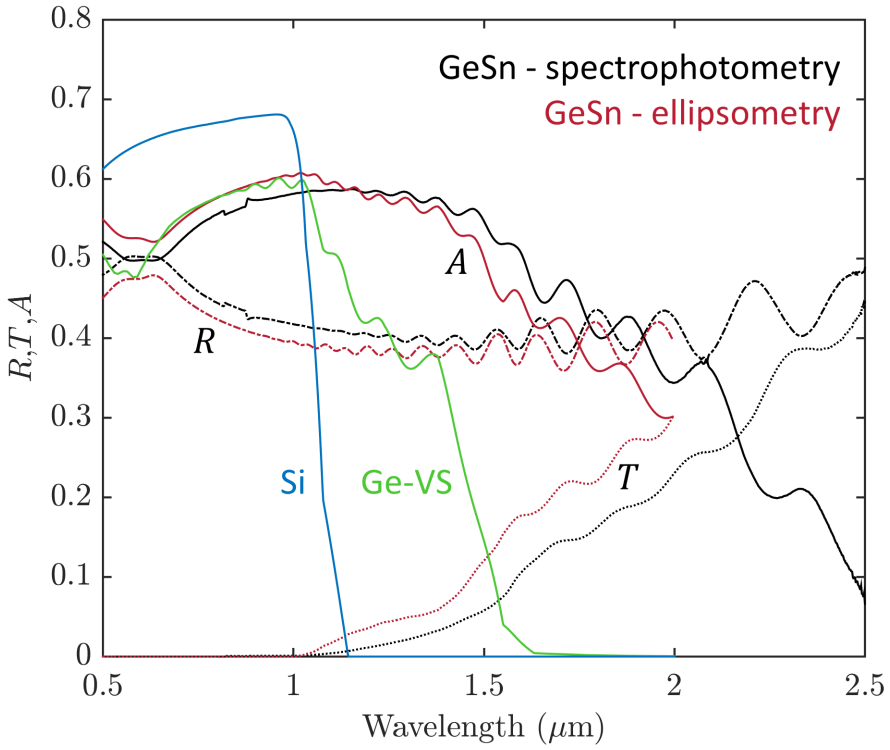

Figure 6.2 Optical properties of the bulk sample compared with those of a Ge-VS on Si and a Si wafer. GeSn properties were measured via spectrophotometry (black curves) and calculated from ellipsometry data (red curves). The absorptance of the Ge-VS on Si (green curve) and the Si wafer (blue curve) were calculated with the data from ref. [168]. Solid curves represent absorptance, dotted curves, the transmittance, and dashed-dotted curves, the reflectance.

that of the other samples calculated in chapter 5. The Si substrate absorbs all the light below 1.0 µm, resulting in null transmittance. Figure 6.2 also presents a comparison with the absorptance of a Ge-VS on Si and a bare Si wafer. Above 1.6 µm, neither Si or Ge absorb light, and the absorptance all occurs in the GeSn layer. The progressive diminution of k for longer wavelengths results in an increase of T and a decrease of A for GeSn. Note that the bare Si wafer has the highest absorptance below 1.0 µm because its lower n is associated with a reduced reflectance.

Furthermore, the oscillations with a period in the order of 100 nm are interference fringes which arise from reflection at the Ge/Si interface. Note that the very short period oscillations (in the order of 1 nm) corresponding to interference fringes of the Si wafer are not resolved by the spectrophotometer. This may be due to the finite spectral resolution of the monochromators. To allow for a better comparison, the backside reflection was not considered in the calculation of optical properties based on ellipsometry measurements. Possible explanations for the differences observed between both sets of curves include the integrating sphere configuration, where light could escape by entry ports and not be collected, and slight non-uniformities on the sample in terms of thicknesses and composition.

6.1.2 Nanopillars fabrication

Nanopillar arrays were fabricated in the GeSn layer described above. Only hexagonal arrays were considered since simulations in section 5 suggest the plane symmetry group doesn't have a significant impact on the absorptance. Small cylinders of ma-N 2403 resist were first defined via EBL with parameters detailed in table 6.2. 2.5 mm × 2.5 mm regions were patterned, which is large enough for optical characterization with the Lambda 1050 spectrophotometer. Different exposition doses and mask designs were used to assess the effect of pillar diameter on the resonance modes. After EBL, the sample underwent 9 min of Cl_2-based RIE. The detailed recipe is included in table 3.1. The etching produces slightly tapered pillars with

Table 6.2 Parameters of 5 nanopillar arrays

Region	Pattern type	Pitch (µm)	Designed diameter (nm)	Dose (µC cm^{-2})	Measured diameter (nm)
R1	Hexagonal	1.1	200	50	250 to 400
R2	Hexagonal	1.1	300	40	400 to 550
R3	Hexagonal	1.1	400	12.5	225 to 325
R4	Hexagonal	1.1	400	25	425 to 575
R5	Hexagonal	1.6	1050	15	1200 to 1300

smooth sidewalls, as shown in figure 6.3. An etch depth of 1.4 µm was estimated from SEM images.

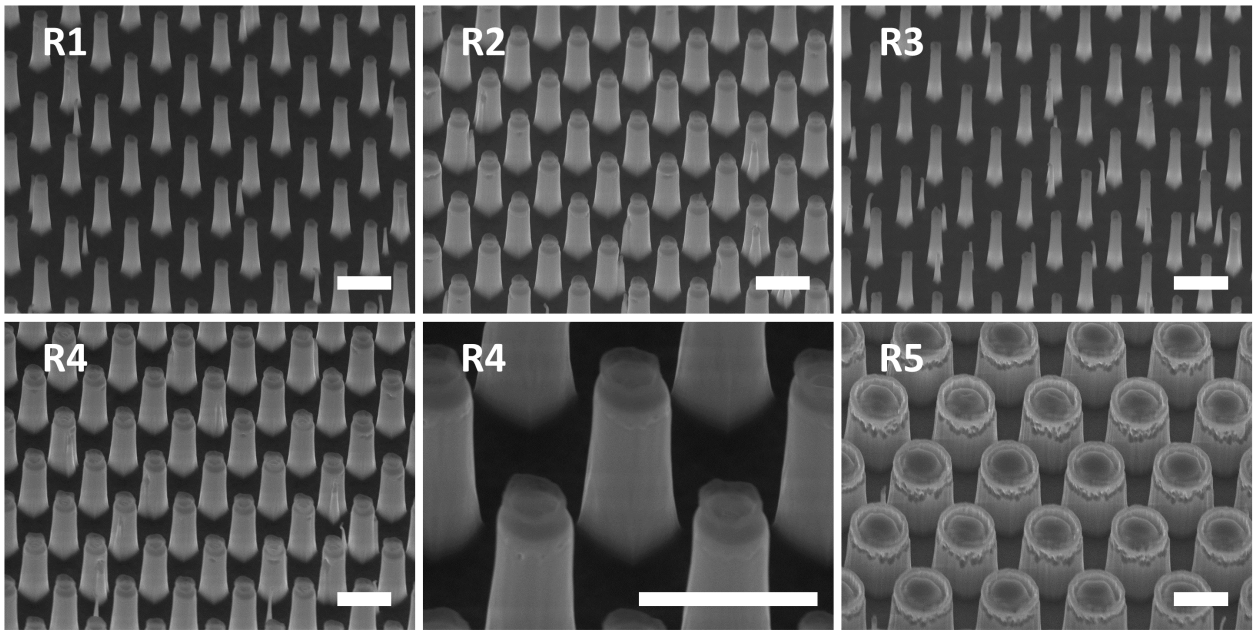

Figure 6.3 SEM images of nanopillar arrays acquired after RIE. Numbers refer to regions of table 6.2. R4 is also shown with a larger magnification to highlight the structure of single pillars, notably the sidewall smoothness. The scale bars are 1 µm and the sample is tilted 37° from the vertical.

Despite the distinct designed diameter of pillars in R2 and R4, their actual size is similar. This is explained by the larger dose used for R2, which can lead to solidification of the resist over a larger surface than exposed. Similarly, the thinnest pillars (R3) are obtained for a large designed diameter (400 nm), but with the smallest dose (12.5 µC cm^{-2}).

6.1.3 Absorptance enhancement

Both reflectance and transmittance of nanopillar arrays were measured with the Lambda 1050 spectrophotometer. Since the integrating sphere takes all specular and diffuse components into account, the absorptance was simply deduced from equation (3.7). Results are plotted in figure 6.4. In all cases, there is a significant increase of the absorptance compared to bulk. The enhancement (up to $\times 2$) mostly comes from the reduced reflectance, which dropped from $\approx 40\,\%$ for bulk to $< 20\,\%$, and even $< 5\,\%$ in some regimes. The improved coupling at the first interface allows a greater portion of the light to be absorbed in GeSn, even if the active volume is up to five times smaller.

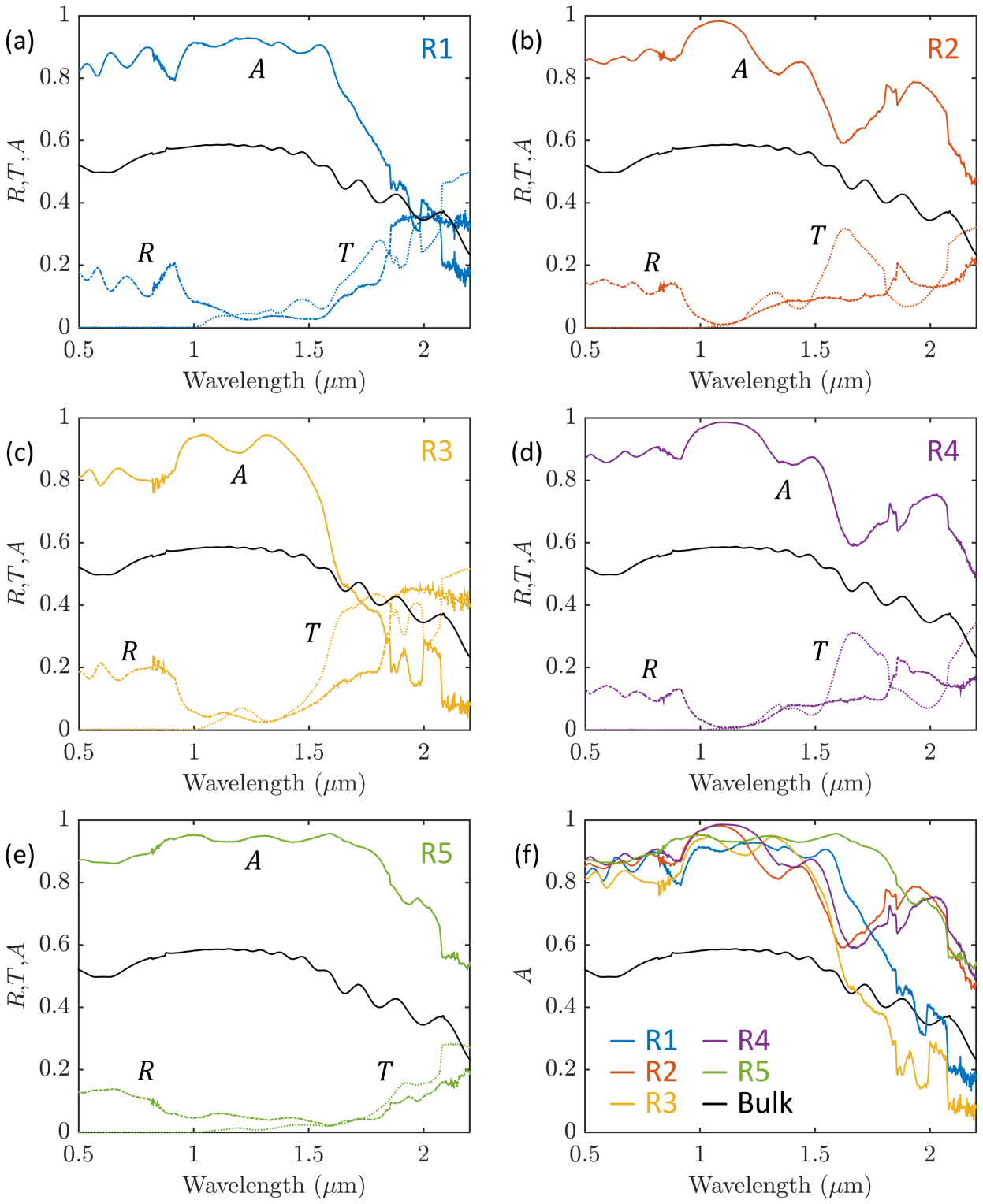

Figure 6.4 Optical properties of nanopillar arrays measured via spectrophotometry. (a-e) Reflectance, transmittance, and absorptance for each array. (f) Comparison of absorptances.

Above $\lambda = 1.7\,\mu m$, only larger pillars (R2, R4, R5) still show a significant enhancement over bulk. This is consistent with the spectral tunability observed on figure 5.4, where larger diameters are required to absorb at longer wavelengths. Furthermore, pillars in R2 and R4 have similar sizes, which lead to comparable absorptance spectra. Otherwise, a change of diameter results in a shift of the resonance modes. While this phenomenon can be observed on figure 6.4, the peaks are not defined as clearly as on figure 5.4. This can be explained by imperfections induced in the fabrication process. For instance, smaller parasite nanowires appear between few pillars on figure 6.3 and sidewall roughness is visible for pillars in R5. Furthermore, small residues from the GeSn growth are found on the backside of the sample. This could lead to diffuse reflection back to the pillars, meaning more absorption being detected than what would occur with a perfectly specular rear interface. Another source of deviation from simulations is the resist that remains after lift-off. While it is expected to be transparent over the wavelength range considered, its presence can modify the propagation of light.

Overall, the fabrication of nanopillars allowed the experimental verification of the absorptance enhancement predicted in chapter 5. As a matter of fact, this enhancement remains valid for wavelengths above 2 µm, Sn alloying being an effective way to push the absorption edge of Ge further in the SWIR. Indeed, arrays R2, R4, and R5 capture more than 50 % of the incident light in this regime, whereas Ge is essentially transparent above 1.6 µm. In addition to Sn alloying, the relaxation of compressive strain will be investigated in the next section as a second mechanism to engineer shallow band gap in group IV semiconductors.

6.2 GeSn microdisks

GeSn devices exhibiting PL activity in the SWIR regime have been demonstrated (see section 2.3.1). However, bandgap calculations of section 2.1 suggest emission at even longer wavelengths can be achieved. Here, GeSn structures with high Sn contents and low strain are fabricated to demonstrate light emission at wavelengths well above 3 µm.

6.2.1 Microdisks fabrication

To study completely relaxed GeSn layers, microdisk arrays were fabricated in samples J and N from table 4.1. 7 µm-wide disks were first defined in ma-N 2410 resist with EBL. Disks were patterned with a 10 µm period over 2.5 mm × 2.5 mm arrays. This was followed by two successive RIE steps. First, a Cl_2-based plasma was used to vertically etch the GeSn layer and transfer the resist pattern to the Ge-VS. Second, Ge was selectively etched in a CF_4-based

plasma, resulting in suspended GeSn microdisks. RIE recipes are detailed in table 3.1.

SEM images of the disks appear in figure 6.5(a-b). The underetching length was assessed via Raman spectroscopy. Indeed, the relaxation of compressive strain induces a shift of the vibrational modes to lower wavenumbers, as discussed in chapter 4. Raman mappings in figure 6.5(c-d) confirm the strain uniformity and the complete underetching. The slight distortion of disks visible in (c) is due to undesirable movement of the stage during the mapping. Ge-Ge mode positions included in table 6.3 are extracted from fitting the Raman spectra displayed in figure 6.5(e-f). Using equation (4.4), strain values close to 0 % are calculated (0.05 % and −0.15 % for samples J and N, respectively).

Table 6.3 Ge-Ge mode position and strain estimation for disks compared with bulk

Sample	Ge-Ge mode		Strain	
	Bulk	Disk	Bulk (XRD)	Disk (Raman)
J	$291.13\,\mathrm{cm}^{-1}$	$288.96\,\mathrm{cm}^{-1}$	−0.33 %	0.05 %
N	$292.14\,\mathrm{cm}^{-1}$	$286.95\,\mathrm{cm}^{-1}$	−1.27 %	−0.15 %

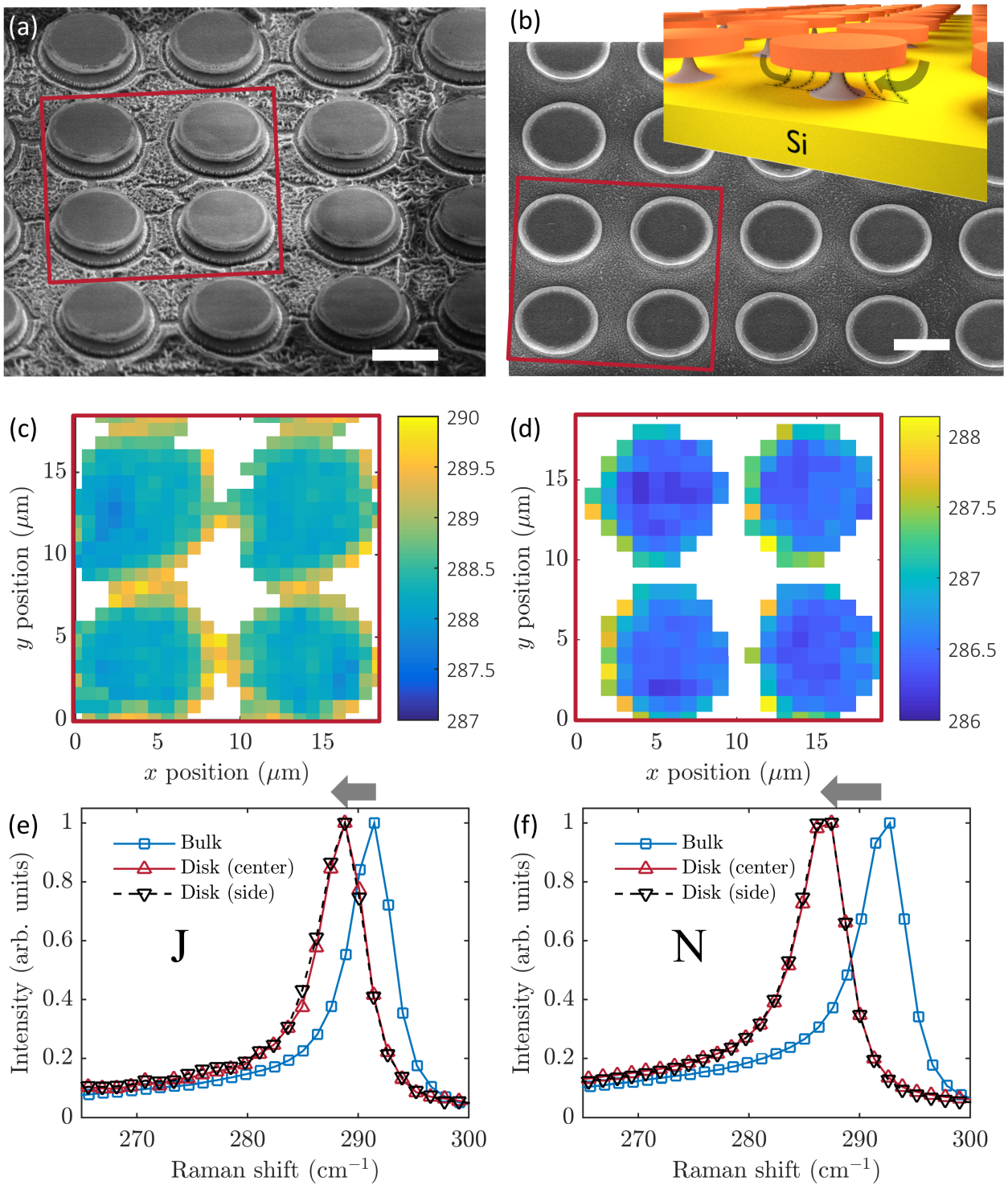

Figure 6.5 Fabrication of GeSn microdisks. (a-b) SEM image of the arrays in samples J (a) and N (b). The scale bars are 5 µm. Inset: Schematic of the CF_4 isotropic underetch. (c-d) Ge-Ge Raman mode position (in cm^{-1}) for four disks on samples J (c) and N (d). (e-f) Raman spectra acquired in the center and on the side of a disk, and comparison with the inital layers J (e) and N (f).

6.2.2 Shift of the emission energy

To evaluate the impact of strain relaxation on the emission energy, PL measurements were conducted for both planar and microdisks geometries. Spectra exhibited in figure 6.6 show a clear shift of the emission to lower energies (i.e. longer wavelengths). For sample J (13.3 at.% in the TL), releasing −0.33 % strain shifted the emission from 3.2 µm to 3.6 µm. As for sample N, the PL measured on bulk (3.3 µm) is similar to that of J, since the higher Sn content (16.9 at.% in the TL) is counterbalanced by the greater compressive strain (−1.27 %). In this case, underetching results in even longer wavelengths, up to 4.0 µm. To our knowledge, this is the longest emission reported for GeSn.

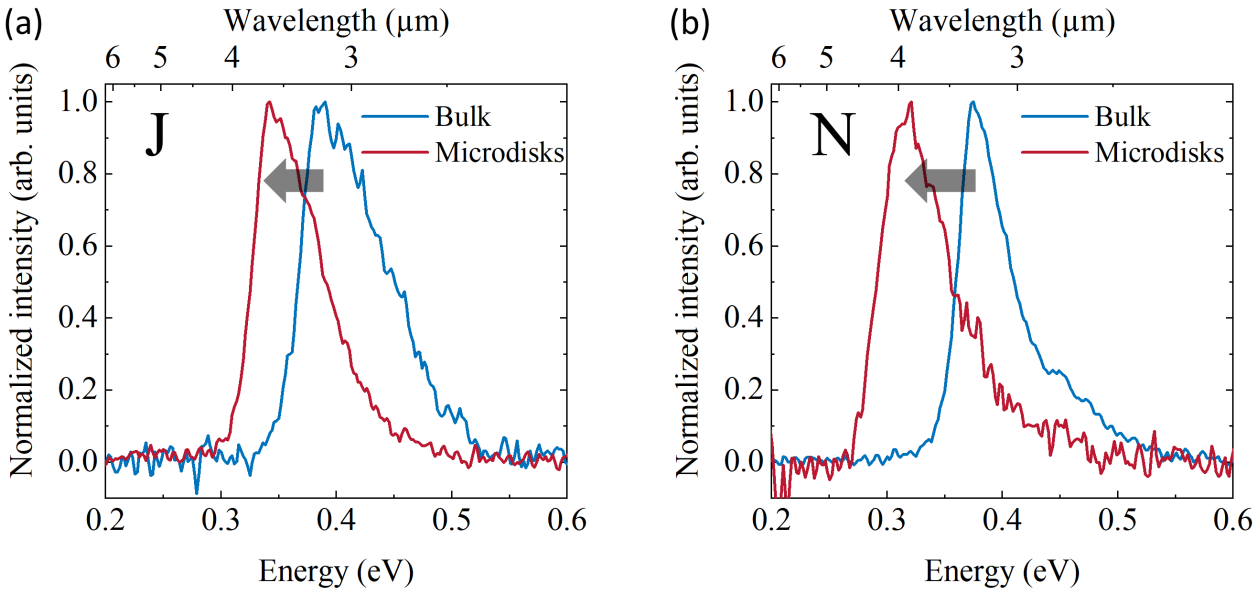

Figure 6.6 Room temperature PL spectra of microdisks compared with bulk for samples J (a) and N (b)

In this chapter, GeSn micro and nanostructures were fabricated to demonstrate the engineering of light absorption and emission. Microfabrication techniques such as EBL and RIE allowed the structuring and underetching of a GeSn layer to form nanopillars and microdisks, which open new doors for the design of devices with enhanced optical properties.

CHAPTER 7 CONCLUSION

Group IV semiconductor alloys such as GeSn are promising for optoelectronic applications. Their interest mainly lies in their compatibility with silicon platforms, which would lead to the monolithic integration of both electronic and photonic devices on the same chip. Sn incorporation in Ge allows to tune the band gap energy in the short-wave and mid infrared and to achieve a direct band gap, making GeSn suited for efficient, Si-compatible light emission and detection. This long-sought-for technology in the semiconductor industry would notably enable the realization of the optical inter-chip and intra-chip communications, which are envisioned to drastically reduce the power consumption of data centers and lessen the burden in large integration chip processing. Potential impacts of this emerging class of group IV semiconductors extend beyond integrated photonics and microelectronics to create a wealth of opportunities in solar energy harvesting, night-vision imaging, as well as spectroscopy and sensing applications.

7.1 Summary of works

The present work contributes to GeSn development by establishing a Raman spectroscopy analysis protocol to decouple the individual effects of strain and composition on different vibrational modes. The work also demonstrates the effect of GeSn structuring for light absorption engineering. Main findings are summarized in this section.

First, a comprehensive investigation of GeSn vibrational modes was conducted using Raman spectroscopy. The higher signal-to-noise ratio associated with a 633 nm excitation laser allowed the clear identification of Ge-Ge, Ge-Sn, disorder-activated (DA), and Sn-Sn like modes. The decoupling of chemical composition and strain effects on the Raman modes was consequently made possible by analyzing a large set of CVD-grown samples with various degrees of Sn content and relaxation. It was found that all four modes downshift as Sn content increases or compressive strain relaxes. Furthermore, the impact on the intensity, width, and asymmetry of peaks was also evaluated. Given their similar behavior, peak positions alone are not sufficient to estimate the content and strain from Raman spectra. This limitation is circumvented by measuring both the position and asymmetry of the main Ge-Ge mode. This model can be used to evaluate the Sn content and strain of GeSn structures from a single Raman spectrum. These results lay the groundwork to employ Raman spectroscopy for a non-destructive characterization of GeSn-based structures and devices.

Second, FDTD simulations were performed to demonstrate the relevance of structuring GeSn layers into nanopillar arrays to increase the absorption of incident light. Their optical properties were compared to those of thin films, calculated analytically with a transfer matrix method. The results show a considerable increase of the absorptance, up to 2.7× for 10 at.% GeSn and 1.9× for 14 at.% GeSn pillars. This is a consequence of a reduction of the $\approx 40\,\%$ reflectance due to a better coupling into the high-index semiconductor layer. This substantial enhancement is valid for specific combinations of wavelengths and pillar diameters corresponding to resonance modes, meaning the spectral absorptance can be tuned by varying the pillar diameters. This behavior is notably achieved with 10 at.% GeSn pillars, as the k dispersion curve is more constant than for higher contents in the considered wavelength range. The strong enhancement of absorptance is preserved for steeper angles of incidence in the case of s-polarized light, whereas p-polarized light is more easily absorbed by a planar layer at larger angles due to a better coupling near the Brewster angle. Nanopillars were fabricated in a 1.1 µm-thick 9 at.% GeSn layer grown on a Ge-VS on a double side polished Si wafer. This allowed the experimental observation of the absorptance enhancement up to a factor two in the SWIR. The ultimate intended use of nanopillar arrays is in high-performance photodetectors. To fabricate such devices, electrical contacts will have to be added, which is more challenging than contacting bulk-like devices. One solution is to add a material to fill the space between pillars and then deposit a transparent electrode. In both cases, low-k materials will have to be used to ensure absorption occurs in the active semiconductor region and to preserve the benefits of structuring the layer into pillars. The change in n between air and the filling material will affect the mode effective refractive index, meaning resonance peaks could occur at different geometries than those presented in this document. Still, trends should be the same provided the filling material has very low k.

Finally, light emission from GeSn microdisks was investigated. Microfabrication protocols were established to develop a variety of GeSn microdisks by EBL patterning followed by two steps of dry plasma etching. The underetching allowed the relaxation of the GeSn layer, confirmed using the Raman spectroscopy model developed in chapter 4. The PL peak shifted to longer wavelengths and reached 3.6 µm and a record 4.0 µm for 13.3 at.% and 16.9 at.% GeSn, respectively.

7.2 Perspectives

This work demonstrated the improved optical performance of GeSn micro and nanostructures. Future research directions should focus notably on the development of new Si-compatible MIR devices using this material system as the building block.

For instance, in order to fabricate nanopillar detectors with an enhanced efficiency, benzocyclobutene (BCB) is often used for filling the space between NWs for devices operating in the visible [106, 169, 170]. However, its high thermal expansion coefficient results in significant stress affecting the structural stability during fabrication. An attractive alternative candidate is tetraethylorthosilicate (TEOS), which exhibits no absorption below 2.5 µm [171]. It also has the advantage of process compatibility with group IV materials and a similar thermal expansion coefficient. As for the top contact, indium tin oxide (ITO) is commonly used [106] because it is mostly transparent in the visible. However, its absorptance increases above $\lambda = 1\,\mu m$ and it becomes opaque in the NIR [172]. Other types of transparent conducting films will thus have to be considered for the top contact. The suggested design is shown in figure 7.1. These concerns confirm that the fabrication of nanopillar photodetectors is more challenging than planar counterparts. Nevertheless, the foreseen increase in efficiency make it an appealing research avenue for group IV compatible devices.

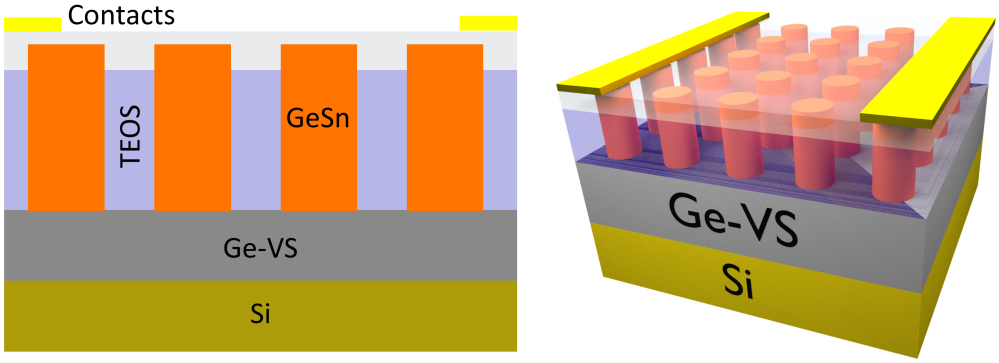

Figure 7.1 Suggested design of a photodetector based on GeSn nanopillars

It is worth pointing out that our work was limited to periodic nanopillar arrays. To maximize broadband absorption, arrays made of nanopillars of different diameters could be investigated. Furthermore, randomly distributed nanopillars have been suggested to outperform periodic structures for certain applications [173].

Following the achievement of 4 µm light emission from GeSn microdisks, the next obvious step would be the demonstration of lasing at this wavelength. The frequency of whispering gallery modes for which lasing occurs can be estimated analytically by solving the wave equations [174] or calculated numerically in an iterative solver. An example of these modes is depicted in figure 7.2. However, for microdisks to be used in devices, outcoupling is an important issue. While this could be achieved via evanescent coupling, the realization of waveguide lasers would facilitate the task. In this scenario, it is worth exploring the possibility to fabricate an underetched Fabry-Pérot cavity. In all cases, the metrology of suspended

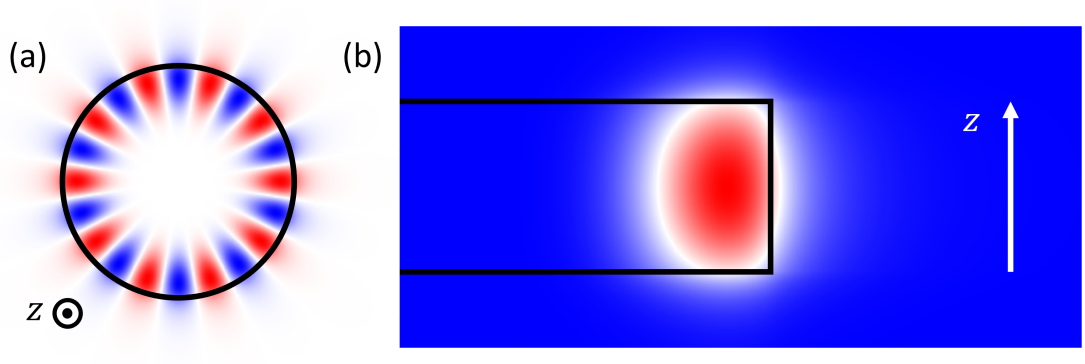

Figure 7.2 Transverse magnetic whispering gallery mode in a 5 µm-wide, 1.2 µm-thick GeSn microdisk ($\lambda = 4.42$ µm in air). (a-b) Top view (a) and side view (half) (b) of the electric field in the z direction.

structures can benefit from a Raman spectroscopy-based characterization technique such as the one developed in chapter 4.

GeSn membranes released by underetching (disk or other) are often completely relaxed. To take advantage of smaller band gaps associated with tensile strain, stressors such as silicon nitride [60] have to be used. A more complex, yet original alternative is to stretch the membranes via active systems like capacitive actuators. This would allow to tune the emission wavelength on demand.

The availability of a GeSn light source integrated on the Si platform is of the first importance to develop optical interconnections in telecommunications. However, it will serve many other purposes where an affordable SWIR and MIR light source (laser or LED) is required. For instance, a theoretical design for an on-chip detector of trace gases using a GeSn laser emitting between 3 µm and 5 µm was recently proposed [12].

In addition to GeSn alloys, group IV devices can also benefit from the additional degree of freedom provided by the introduction of Si in the lattice, allowing to independently tune the band gap energy and the lattice constant. This property can help to design heterostructures with the proper band alignment [67, 82]. Because of its higher gap, SiGeSn can be used as barriers to better confine the carriers in the active region. Ternary alloys are also envisioned to enhance the conversion efficiency of photovoltaic devices. The addition of a SiGeSn layer in state-of-the art solar cells, as depicted in figure 7.3, would allow to absorb a portion of the solar spectrum which is currently not exploited [13].

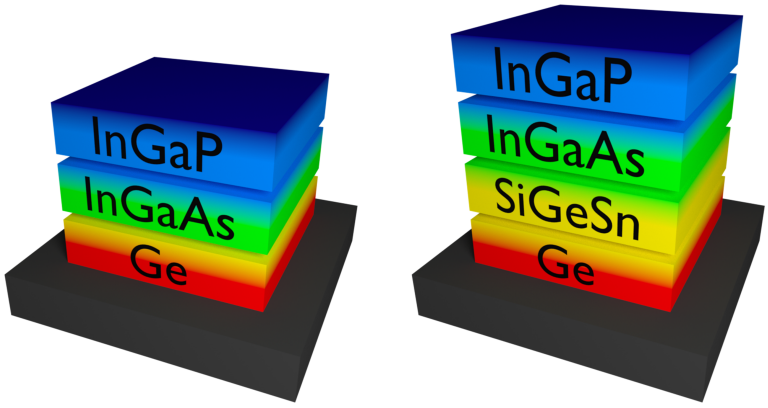

Figure 7.3 Suggested design for the addition of a SiGeSn layer in a multijunction solar cell

BIBLIOGRAPHY

[1] Cisco, "Cisco Visual Networking Index: Forecast and Trends, 2017-2022," 2018. [Online]. Available: https://www.cisco.com/c/en/us/solutions/collateral/service-provider/visual-networking-index-vni/white-paper-c11-741490.pdf

[2] The Boston Consulting Group, "SMARTer 2020: The role of ICT in driving a sustainable future," p. 243, 2012. [Online]. Available: https://www.telenor.com/wp-content/uploads/2014/04/SMARTer-2020-The-Role-of-ICT-in-Driving-a-Sustainable-Future-December-2012._2.pdf

[3] Natural Resources Defense Council, "Data Center Efficiency Assessment," 2014.

[4] Ministère de l'Énergie et des Ressources naturelles, "Gros plan sur l'énergie: Consommation d'électricité," 2013. [Online]. Available: https://mern.gouv.qc.ca/energie/statistiques/statistiques-consommation-electricite.jsp

[5] A. S. Andrae, "Total Consumer Power Consumption Forecast," 2017. [Online]. Available: https://www.researchgate.net/publication/320225452_Total_Consumer_Power_Consumption_Forecast

[6] International Energy Agency, "World Energy Outlook 2018," 2018.

[7] G. P. Agrawal, "Optical Communication: Its History and Recent Progress," in *Optics in Our Time*. Springer International Publishing, 2016, pp. 177–199. [Online]. Available: https://doi.org/10.1007/978-3-319-31903-2_8

[8] A. Alduino and M. Paniccia, "Wiring electronics with light," *Nature Photonics*, vol. 1, no. 3, pp. 153–155, mar 2007. [Online]. Available: http://www.nature.com/articles/nphoton.2007.17

[9] A. H. Atabaki, S. Moazeni, F. Pavanello, H. Gevorgyan, J. Notaros, L. Alloatti, M. T. Wade, C. Sun, S. A. Kruger, H. Meng, K. Al Qubaisi, I. Wang, B. Zhang, A. Khilo, C. V. Baiocco, M. A. Popović, V. M. Stojanović, and R. J. Ram, "Integrating photonics with silicon nanoelectronics for the next generation of systems on a chip," *Nature*, vol. 556, no. 7701, pp. 349–354, apr 2018. [Online]. Available: http://www.nature.com/articles/s41586-018-0028-z

[10] D. Thomson, A. Zilkie, J. E. Bowers, T. Komljenovic, G. T. Reed, L. Vivien, D. Marris-Morini, E. Cassan, L. Virot, J.-m. Fédéli, J.-m. Hartmann, J. H. Schmid, D.-X. Xu, F. Boeuf, P. O'Brien, G. Z. Mashanovich, and M. Nedeljkovic, "Roadmap on silicon photonics," *Journal of Optics*, vol. 18, no. 7, p. 073003, jul 2016. [Online]. Available: https://doi.org/10.1088/2040-8978/18/7/073003

[11] R. Soref, D. Buca, and S.-Q. Yu, "Group IV Photonics: Driving Integrated Optoelectronics," *Optics and Photonics News*, vol. 27, no. 1, p. 32, jan 2016. [Online]. Available: https://www.osapublishing.org/abstract.cfm?URI=opn-27-1-32

[12] R. A. Soref, F. De Leonardis, and V. M. N. Passaro, "On-Chip Detection of Trace Gases using Photonic Matched Filters," *Journal of Lightwave Technology*, vol. 37, no. 4, pp. 1388 – 1395, 2019. [Online]. Available: https://doi.org/10.1109/JLT.2019.2894035

[13] Y.-y. Fang, J. Xie, J. Tolle, R. Roucka, V. R. D'Costa, A. V. G. Chizmeshya, J. Menendez, and J. Kouvetakis, "Molecular-Based Synthetic Approach to New Group IV Materials for High-Efficiency, Low-Cost Solar Cells and Si-Based Optoelectronics," *Journal of the American Chemical Society*, vol. 130, no. 47, pp. 16 095–16 102, nov 2008. [Online]. Available: http://pubs.acs.org/doi/abs/10.1021/ja806636c

[14] B. Vincent, F. Gencarelli, H. Bender, C. Merckling, B. Douhard, D. H. Petersen, O. Hansen, H. H. Henrichsen, J. Meersschaut, W. Vandervorst, M. Heyns, R. Loo, and M. Caymax, "Undoped and in-situ B doped GeSn epitaxial growth on Ge by atmospheric pressure-chemical vapor deposition," *Applied Physics Letters*, vol. 99, no. 15, p. 152103, oct 2011. [Online]. Available: http://aip.scitation.org/doi/10.1063/1.3645620

[15] R. Loo, B. Vincent, F. Gencarelli, C. Merckling, A. Kumar, G. Eneman, L. Witters, W. Vandervorst, M. Caymax, M. Heyns, and A. Thean, "GeSn Materials: Challenges and Applications," *ECS Journal of Solid State Science and Technology*, vol. 2, no. 1, pp. N35–N40, dec 2013. [Online]. Available: http://jss.ecsdl.org/lookup/doi/10.1149/2.039301jss

[16] S. Gupta, B. Vincent, B. Yang, D. Lin, F. Gencarelli, J.-Y. J. Lin, R. Chen, O. Richard, H. Bender, B. Magyari-Kope, M. Caymax, J. Dekoster, Y. Nishi, and K. C. Saraswat, "Towards high mobility GeSn channel nMOSFETs: Improved surface passivation using novel ozone oxidation method," in *2012 International Electron Devices Meeting*. IEEE, dec 2012, pp. 16.2.1–16.2.4. [Online]. Available: http://ieeexplore.ieee.org/document/6479052/

[17] W. Wang, D. Lei, Y.-c. Huang, K. H. Lee, W.-k. Loke, Y. Dong, S. Xu, C. S. Tan, H. Wang, S.-f. Yoon, X. Gong, and Y.-c. Yeo, "High-performance GeSn photodetector and fin field-effect transistor (FinFET) on an advanced GeSn-on-insulator platform," *Optics Express*, vol. 26, no. 8, p. 10305, apr 2018. [Online]. Available: https://doi.org/10.1364/OE.26.010305

[18] P. Moontragoon, Z. Ikonić, and P. Harrison, "Band structure calculations of Si-Ge-Sn alloys: achieving direct band gap materials," *Semiconductor Science and Technology*, vol. 22, no. 7, pp. 742–748, jul 2007. [Online]. Available: https://doi.org/10.1088/0268-1242/22/7/012

[19] C. Goodman, "Direct-gap group IV semiconductors based on tin," *IEE Proceedings I Solid State and Electron Devices*, vol. 129, no. 5, p. 189, 1982. [Online]. Available: https://doi.org/10.1049/ip-i-1.1982.0043

[20] S. Gupta, B. Magyari-Köpe, Y. Nishi, and K. C. Saraswat, "Achieving direct band gap in germanium through integration of Sn alloying and external strain," *Journal of Applied Physics*, vol. 113, no. 7, p. 073707, feb 2013. [Online]. Available: https://doi.org/10.1063/1.4792649

[21] D. W. Jenkins and J. D. Dow, "Electronic properties of metastable GeSn alloys," *Physical Review B*, vol. 36, no. 15, pp. 7994–8000, nov 1987. [Online]. Available: https://link.aps.org/doi/10.1103/PhysRevB.36.7994

[22] K. Mäder, A. Baldereschi, and H. von Känel, "Band structure and instability of GeSn alloys," *Solid State Communications*, vol. 69, no. 12, pp. 1123–1126, mar 1989. [Online]. Available: https://doi.org/10.1016/0038-1098(89)91046-6

[23] W.-J. Yin, X.-G. Gong, and S.-H. Wei, "Origin of the unusually large band-gap bowing and the breakdown of the band-edge distribution rule in the SnGe alloys," *Physical Review B*, vol. 78, no. 16, p. 161203, oct 2008. [Online]. Available: https://doi.org/10.1103/PhysRevB.78.161203

[24] C. Xu, C. L. Senaratne, R. J. Culbertson, J. Kouvetakis, and J. Menéndez, "Deviations from Vegard's law in semiconductor thin films measured with X-ray diffraction and Rutherford backscattering: The GeSn and GeSi cases," *Journal of Applied Physics*, vol. 122, no. 12, p. 125702, sep 2017. [Online]. Available: http://aip.scitation.org/doi/10.1063/1.4996306

[25] M. J. Süess, R. Geiger, R. A. Minamisawa, G. Schiefler, J. Frigerio, D. Chrastina, G. Isella, R. Spolenak, J. Faist, and H. Sigg, "Analysis of enhanced light emission from highly strained germanium microbridges," *Nature Photonics*, vol. 7, no. 6, pp. 466–472, jun 2013. [Online]. Available: http://www.nature.com/articles/nphoton.2013.67

[26] M. El Kurdi, M. Prost, A. Ghrib, S. Sauvage, X. Checoury, G. Beaudoin, I. Sagnes, G. Picardi, R. Ossikovski, and P. Boucaud, "Direct Band Gap Germanium Microdisks Obtained with Silicon Nitride Stressor Layers," *ACS Photonics*, vol. 3, no. 3, pp. 443–448, mar 2016. [Online]. Available: https://doi.org/10.1021/acsphotonics.5b00632

[27] A. Attiaoui and O. Moutanabbir, "Indirect-to-direct band gap transition in relaxed and strained GeSiSn ternary alloys," *Journal of Applied Physics*, vol. 116, no. 6, p. 063712, aug 2014. [Online]. Available: https://doi.org/10.1063/1.4889926

[28] E. Kasper, M. Kittler, M. Oehme, and T. Arguirov, "Germanium tin: silicon photonics toward the mid-infrared [Invited]," *Photonics Research*, vol. 1, no. 2, p. 69, aug 2013. [Online]. Available: https://www.osapublishing.org/prj/abstract.cfm?uri=prj-1-2-69

[29] J. P. Fleurial, "Si-Ge-Metal Ternary Phase Diagram Calculations," *Journal of The Electrochemical Society*, vol. 137, no. 9, p. 2928, 1990. [Online]. Available: http://jes.ecsdl.org/cgi/doi/10.1149/1.2087101

[30] S. Takeuchi, A. Sakai, O. Nakatsuka, M. Ogawa, and S. Zaima, "Tensile strained Ge layers on strain-relaxed GeSn/virtual Ge substrates," *Thin Solid Films*, vol. 517, no. 1, pp. 159–162, nov 2008. [Online]. Available: https://doi.org/10.1016/j.tsf.2008.08.068

[31] S. Wirths, D. Buca, G. Mussler, A. T. Tiedemann, B. Holländer, P. Bernardy, T. Stoica, D. Grützmacher, and S. Mantl, "Reduced Pressure CVD Growth of Ge and GeSn Alloys," *ECS Journal of Solid State Science and Technology*, vol. 2, no. 5, pp. N99–N102, mar 2013. [Online]. Available: http://jss.ecsdl.org/lookup/doi/10.1149/2.006305jss

[32] S. Oguz, W. Paul, T. F. Deutsch, B.-Y. Tsaur, and D. V. Murphy, "Synthesis of metastable, semiconducting Ge-Sn alloys by pulsed UV laser crystallization," *Applied Physics Letters*, vol. 43, no. 9, pp. 848–850, nov 1983. [Online]. Available: http://aip.scitation.org/doi/10.1063/1.94524

[33] S. Shah, J. Greene, L. Abels, Q. Yao, and P. Raccah, "Growth of single-crystal metastable GeSn alloys on Ge(100) and GaAs(100) substrates," *Journal of Crystal Growth*, vol. 83, no. 1, pp. 3–10, may 1987. [Online]. Available: https://doi.org/10.1016/0022-0248(87)90495-7

[34] O. Gurdal, P. Desjardins, J. R. A. Carlsson, N. Taylor, H. H. Radamson, J.-E. Sundgren, and J. E. Greene, "Low-temperature growth and critical epitaxial thicknesses of fully strained metastable GeSn alloys on Ge(001)2x1," *Journal of Applied Physics*, vol. 83, no. 1, pp. 162–170, jan 1998. [Online]. Available: http://aip.scitation.org/doi/10.1063/1.366690

[35] V. D'Costa, J. Tolle, R. Roucka, C. Poweleit, J. Kouvetakis, and J. Menéndez, "Raman scattering in GeSn alloys," *Solid State Communications*, vol. 144, no. 5-6, pp. 240–244, nov 2007. [Online]. Available: https://doi.org/10.1016/j.ssc.2007.08.020

[36] S. Wirths, D. Buca, and S. Mantl, "Si-Ge-Sn alloys: From growth to applications," *Progress in Crystal Growth and Characterization of Materials*, vol. 62, no. 1, pp. 1–39, mar 2016. [Online]. Available: https://doi.org/10.1016/j.pcrysgrow.2015.11.001

[37] J. Taraci, J. Tolle, J. Kouvetakis, M. R. McCartney, D. J. Smith, J. Menendez, and M. A. Santana, "Simple chemical routes to diamond-cubic germanium-tin alloys," *Applied Physics Letters*, vol. 78, no. 23, pp. 3607–3609, jun 2001. [Online]. Available: http://aip.scitation.org/doi/10.1063/1.1376156

[38] S. A. Ghetmiri, W. Du, B. R. Conley, A. Mosleh, A. Nazzal, G. Sun, R. A. Soref, J. Margetis, J. Tolle, H. A. Naseem, and S.-Q. Yu, "Shortwave-infrared photoluminescence from GeSn thin films on silicon," *Journal of Vacuum Science & Technology B, Nanotechnology and Microelectronics: Materials, Processing, Measurement, and Phenomena*, vol. 32, no. 6, p. 060601, 2014. [Online]. Available: http://avs.scitation.org/doi/10.1116/1.4897917

[39] J. Margetis, A. Mosleh, S. A. Ghetmiri, S. Al-Kabi, W. Dou, W. Du, N. Bhargava, S.-Q. Yu, H. Profijt, D. Kohen, R. Loo, A. Vohra, and J. Tolle, "Fundamentals of GeSn and SiGeSn RPCVD epitaxy," *Materials Science in Semiconductor Processing*, vol. 70, pp. 38–43, 2017. [Online]. Available: https://doi.org/10.1016/j.mssp.2016.12.024

[40] S. Assali, J. Nicolas, S. Mukherjee, A. Dijkstra, and O. Moutanabbir, "Atomically uniform Sn-rich GeSn semiconductors with 3.0-3.5 μm room-temperature optical emission," *Applied Physics Letters*, vol. 112, no. 25, p. 251903, jun 2018. [Online]. Available: http://aip.scitation.org/doi/10.1063/1.5038644

[41] S. Assali, J. Nicolas, and O. Moutanabbir, "Enhanced Sn incorporation in GeSn epitaxial semiconductors via strain relaxation," *Journal of Applied Physics*, vol. 125, no. 2, p. 025304, jan 2019. [Online]. Available: http://aip.scitation.org/doi/10.1063/1.5050273

[42] M. Medikonda, G. R. Muthinti, R. Vasić, T. N. Adam, A. Reznicek, M. Wormington, G. Malladi, Y. Kim, Y.-C. Huang, and A. C. Diebold, "Optical properties of pseudomorphic GeSn alloys on Ge(001)," *Journal of Vacuum Science & Technology B, Nanotechnology and Microelectronics: Materials, Processing, Measurement, and Phenomena*, vol. 32, no. 6, p. 061805, nov 2014. [Online]. Available: http://avs.scitation.org/doi/10.1116/1.4901254

[43] J. Aubin, J. M. Hartmann, A. Gassenq, J. L. Rouviere, E. Robin, V. Delaye, D. Cooper, N. Mollard, V. Reboud, and V. Calvo, "Growth and structural properties of step-graded, high Sn content GeSn layers on Ge," *Semiconductor Science and Technology*, vol. 32, no. 9, p. 094006, sep 2017. [Online]. Available: https://doi.org/10.1088/1361-6641/aa8084

[44] J. Aubin and J. Hartmann, "GeSn growth kinetics in reduced pressure chemical vapor deposition from Ge2H6 and SnCl4," *Journal of Crystal Growth*, vol. 482, pp. 30–35, jan 2018. [Online]. Available: https://doi.org/10.1016/j.jcrysgro.2017.10.030

[45] Y. Chibane and M. Ferhat, "Electronic structure of SnGe alloys for small Sn compositions: Unusual structural and electronic properties," *Journal of Applied Physics*, vol. 107, no. 5, p. 053512, mar 2010. [Online]. Available: http://aip.scitation.org/doi/10.1063/1.3326162

[46] R. Beeler, R. Roucka, A. V. G. Chizmeshya, J. Kouvetakis, and J. Menéndez, "Nonlinear structure-composition relationships in the GeSn/Si(100) system," *Physical Review B*, vol. 84, no. 3, p. 035204, jul 2011. [Online]. Available: https://link.aps.org/doi/10.1103/PhysRevB.84.035204

[47] N. Bhargava, M. Coppinger, J. Prakash Gupta, L. Wielunski, and J. Kolodzey, "Lattice constant and substitutional composition of GeSn alloys grown by molecular beam epitaxy," *Applied Physics Letters*, vol. 103, no. 4, p. 041908, jul 2013. [Online]. Available: http://aip.scitation.org/doi/10.1063/1.4816660

[48] F. Gencarelli, B. Vincent, J. Demeulemeester, A. Vantomme, A. Moussa, A. Franquet, A. Kumar, H. Bender, J. Meersschaut, W. Vandervorst, R. Loo, M. Caymax, K. Temst, and M. Heyns, "Crystalline Properties and Strain Relaxation Mechanism of CVD Grown GeSn," *ECS Journal of Solid State Science and Technology*, vol. 2, no. 4, pp. P134–P137, jan 2013. [Online]. Available: https://doi.org/10.1149/2.011304jss

[49] J. Hartmann, A. Papon, V. Destefanis, and T. Billon, "Reduced pressure chemical vapor deposition of Ge thick layers on Si(001), Si(011) and Si(111)," *Journal of*

Crystal Growth, vol. 310, no. 24, pp. 5287–5296, dec 2008. [Online]. Available: https://doi.org/10.1016/j.jcrysgro.2008.08.062

[50] J. M. Hartmann, A. Abbadie, N. Cherkashin, H. Grampeix, and L. Clavelier, "Epitaxial growth of Ge thick layers on nominal and 6 degree off Si(0 0 1); Ge surface passivation by Si," *Semiconductor Science and Technology*, vol. 24, no. 5, p. 055002, may 2009. [Online]. Available: https://doi.org/10.1088/0268-1242/24/5/055002

[51] J. Hartmann, A. Abbadie, J. Barnes, J. Fédéli, T. Billon, and L. Vivien, "Impact of the H2 anneal on the structural and optical properties of thin and thick Ge layers on Si; Low temperature surface passivation of Ge by Si," *Journal of Crystal Growth*, vol. 312, no. 4, pp. 532–541, feb 2010. [Online]. Available: https://doi.org/10.1016/j.jcrysgro.2009.11.056

[52] J. Hartmann and J. Aubin, "Assessment of the growth/etch back technique for the production of Ge strain-relaxed buffers on Si," *Journal of Crystal Growth*, vol. 488, pp. 43–50, apr 2018. [Online]. Available: https://doi.org/10.1016/j.jcrysgro.2018.02.036

[53] J. Margetis, S.-Q. Yu, N. Bhargava, B. Li, W. Du, and J. Tolle, "Strain engineering in epitaxial GeSn: a path towards low-defect and high Sn-content layers," *Semiconductor Science and Technology*, vol. 32, no. 12, p. 124006, dec 2017. [Online]. Available: https://doi.org/10.1088/1361-6641/aa7fc7

[54] W. Dou, M. Benamara, A. Mosleh, J. Margetis, P. Grant, Y. Zhou, S. Al-Kabi, W. Du, J. Tolle, B. Li, M. Mortazavi, and S.-Q. Yu, "Investigation of GeSn Strain Relaxation and Spontaneous Composition Gradient for Low-Defect and High-Sn Alloy Growth," *Scientific Reports*, vol. 8, no. 1, p. 5640, dec 2018. [Online]. Available: https://doi.org/10.1038/s41598-018-24018-6

[55] J. Margetis, S. Al-Kabi, W. Du, W. Dou, Y. Zhou, T. Pham, P. Grant, S. Ghetmiri, A. Mosleh, B. Li, J. Liu, G. Sun, R. Soref, J. Tolle, M. Mortazavi, and S.-Q. Yu, "Si-Based GeSn Lasers with Wavelength Coverage of 2-3 μm and Operating Temperatures up to 180 K," *ACS Photonics*, vol. 5, no. 3, pp. 827–833, mar 2018. [Online]. Available: http://pubs.acs.org/doi/10.1021/acsphotonics.7b00938

[56] W. Dou, Y. Zhou, J. Margetis, S. A. Ghetmiri, S. Al-Kabi, W. Du, J. Liu, G. Sun, R. A. Soref, J. Tolle, B. Li, M. Mortazavi, and S.-Q. Yu, "Optically pumped lasing at 3 μm from compositionally graded GeSn with tin up to 22.3%," *Optics Letters*, vol. 43, no. 19, p. 4558, oct 2018. [Online]. Available: https://doi.org/10.1364/OL.43.004558

[57] A. Gassenq, L. Milord, J. Aubin, N. Pauc, K. Guilloy, J. Rothman, D. Rouchon, A. Chelnokov, J. M. Hartmann, V. Reboud, and V. Calvo, "Raman spectral shift versus strain and composition in GeSn layers with 6%-15% Sn content," *Applied Physics Letters*, vol. 110, no. 11, p. 112101, mar 2017. [Online]. Available: https://doi.org/10.1063/1.4978512

[58] S. Gupta, R. Chen, Y.-c. Huang, Y. Kim, E. Sanchez, J. S. Harris, and K. C. Saraswat, "Highly Selective Dry Etching of Germanium over Germanium-Tin (GeSn): A Novel Route for GeSn Nanostructure Fabrication," *Nano Letters*, vol. 13, no. 8, pp. 3783–3790, aug 2013. [Online]. Available: https://doi.org/10.1021/nl4017286

[59] L. Milord, J. Aubin, A. Gassenq, S. Tardif, K. Guilloy, N. Pauc, J. Rothman, A. Chelnokov, J. M. Hartmann, V. Calvo, and V. Reboud, "Inductively coupled plasma etching of germanium tin for the fabrication of photonic components," *Proc. SPIE, Silicon Photonics XII*, vol. 10108, pp. 101 080C–101 080C–7, 2017. [Online]. Available: https://doi.org/10.1117/12.2252280

[60] R. W. Millar, D. C. S. Dumas, K. F. Gallacher, P. Jahandar, C. MacGregor, M. Myronov, and D. J. Paul, "Mid-infrared light emission > 3um wavelength from tensile strained GeSn microdisks," *Optics Express*, vol. 25, no. 21, p. 25374, 2017. [Online]. Available: https://doi.org/10.1364/OE.25.025374

[61] S. Wirths, R. Geiger, N. von den Driesch, G. Mussler, T. Stoica, S. Mantl, Z. Ikonic, M. Luysberg, S. Chiussi, J. M. Hartmann, H. Sigg, J. Faist, D. Buca, and D. Grützmacher, "Lasing in direct-bandgap GeSn alloy grown on Si," *Nature Photonics*, vol. 9, no. 2, pp. 88–92, feb 2015. [Online]. Available: https://doi.org/10.1038/nphoton.2014.321

[62] N. Bhargava, J. Margetis, and J. Tolle, "As doping of Si-Ge-Sn epitaxial semiconductor materials on a commercial CVD reactor," *Semiconductor Science and Technology*, vol. 32, no. 9, p. 94003, 2017. [Online]. Available: http://dx.doi.org/10.1088/1361-6641/aa7e19

[63] D. Kohen, A. Vohra, R. Loo, W. Vandervorst, N. Bhargava, J. Margetis, and J. Tolle, "Enhanced B doping in CVD-grown GeSn:B using B δ-doping layers," *Journal of Crystal Growth*, vol. 483, pp. 285–290, 2018. [Online]. Available: https://doi.org/10.1016/j.jcrysgro.2017.12.018

[64] C. Schulte-Braucks, S. Glass, E. Hofmann, D. Stange, N. von den Driesch, J. M. Hartmann, Z. Ikonic, Q. T. Zhao, D. Buca, and S. Mantl, "Process modules for GeSn

nanoelectronics with high Sn-contents," *Solid-State Electronics*, vol. 128, pp. 54–59, 2017. [Online]. Available: http://dx.doi.org/10.1016/j.sse.2016.10.024

[65] G.-E. Chang, S.-W. Chang, and S. L. Chuang, "Strain-Balanced GeSn - SiGeSn Multiple-Quantum-Well Lasers," *IEEE Journal of Quantum Electronics*, vol. 46, no. 12, pp. 1813–1820, dec 2010. [Online]. Available: http://ieeexplore.ieee.org/document/5617350/

[66] B. Dutt, Hai Lin, D. S. Sukhdeo, B. M. Vulovic, S. Gupta, Donguk Nam, K. C. Saraswat, and J. S. Harris, "Theoretical Analysis of GeSn Alloys as a Gain Medium for a Si-Compatible Laser," *IEEE Journal of Selected Topics in Quantum Electronics*, vol. 19, no. 5, pp. 1 502 706–1 502 706, sep 2013. [Online]. Available: http://ieeexplore.ieee.org/document/6415974/

[67] G. Sun, R. A. Soref, and H. H. Cheng, "Design of an electrically pumped SiGeSn/GeSn/SiGeSn double-heterostructure midinfrared laser," *Journal of Applied Physics*, vol. 108, no. 3, p. 033107, aug 2010. [Online]. Available: http://aip.scitation.org/doi/10.1063/1.3467766

[68] G. Sun, R. A. Soref, and H. H. Cheng, "Design of a Si-based lattice-matched room-temperature GeSn/GeSiSn multi-quantum-well mid-infrared laser diode," *Optics Express*, vol. 18, no. 19, p. 19957, sep 2010. [Online]. Available: https://doi.org/10.1364/OE.18.019957

[69] D. Stange, S. Wirths, R. Geiger, C. Schulte-Braucks, B. Marzban, N. von den Driesch, G. Mussler, T. Zabel, T. Stoica, J.-M. Hartmann, S. Mantl, Z. Ikonic, D. Grützmacher, H. Sigg, J. Witzens, and D. Buca, "Optically Pumped GeSn Microdisk Lasers on Si," *ACS Photonics*, vol. 3, no. 7, pp. 1279–1285, jul 2016. [Online]. Available: http://pubs.acs.org/doi/10.1021/acsphotonics.6b00258

[70] S. Al-Kabi, S. A. Ghetmiri, J. Margetis, T. Pham, Y. Zhou, W. Dou, B. Collier, R. Quinde, W. Du, A. Mosleh, J. Liu, G. Sun, R. A. Soref, J. Tolle, B. Li, M. Mortazavi, H. A. Naseem, and S.-Q. Yu, "An optically pumped 2.5 μm GeSn laser on Si operating at 110 K," *Applied Physics Letters*, vol. 109, no. 17, p. 171105, oct 2016. [Online]. Available: http://aip.scitation.org/doi/10.1063/1.4966141

[71] Q. M. Thai, N. Pauc, J. Aubin, M. Bertrand, J. Chrétien, V. Delaye, A. Chelnokov, J.-M. Hartmann, V. Reboud, and V. Calvo, "GeSn heterostructure micro-disk laser operating at 230 K," *Optics Express*, vol. 26, no. 25, p. 32500, dec 2018. [Online]. Available: https://doi.org/10.1364/OE.26.032500

[72] Q. M. Thai, N. Pauc, J. Aubin, M. Bertrand, J. Chrétien, A. Chelnokov, J. M. Hartmann, V. Reboud, and V. Calvo, "2D hexagonal photonic crystal GeSn laser with 16% Sn content," *Applied Physics Letters*, vol. 113, no. 5, p. 051104, jul 2018. [Online]. Available: http://aip.scitation.org/doi/10.1063/1.5036739

[73] M. Oehme, J. Werner, M. Gollhofer, M. Schmid, M. Kaschel, E. Kasper, and J. Schulze, "Room-Temperature Electroluminescence From GeSn Light-Emitting Pin Diodes on Si," *IEEE Photonics Technology Letters*, vol. 23, no. 23, pp. 1751–1753, dec 2011. [Online]. Available: http://ieeexplore.ieee.org/document/6025261/

[74] R. Roucka, J. Mathews, R. T. Beeler, J. Tolle, J. Kouvetakis, and J. Menéndez, "Direct gap electroluminescence from Si/GeSn p-i-n heterostructure diodes," *Applied Physics Letters*, vol. 98, no. 6, p. 061109, feb 2011. [Online]. Available: http://aip.scitation.org/doi/10.1063/1.3554747

[75] M. Oehme, K. Kostecki, T. Arguirov, G. Mussler, K. Ye, M. Gollhofer, M. Schmid, M. Kaschel, R. A. Korner, M. Kittler, D. Buca, E. Kasper, and J. Schulze, "GeSn heterojunction LEDs on Si substrates," *IEEE Photonics Technology Letters*, vol. 26, no. 2, pp. 187–189, 2014. [Online]. Available: https://doi.org/10.1109/LPT.2013.2291571

[76] W. Du, Y. Zhou, S. A. Ghetmiri, A. Mosleh, B. R. Conley, A. Nazzal, R. A. Soref, G. Sun, J. Tolle, J. Margetis, H. A. Naseem, and S. Q. Yu, "Room-temperature electroluminescence from Ge/GeSn/Ge diodes on Si substrates," *Applied Physics Letters*, vol. 104, no. 24, pp. 4–8, 2014. [Online]. Available: http://dx.doi.org/10.1063/1.4884380

[77] J. D. Gallagher, C. L. Senaratne, P. M. Wallace, J. Menéndez, and J. Kouvetakis, "Electroluminescence from GeSn diodes with degenerate pn junctions," *Applied Physics Letters*, vol. 107, no. 12, p. 123507, sep 2015. [Online]. Available: http://aip.scitation.org/doi/10.1063/1.4931707

[78] S. Q. Yu, S. A. Ghetmiri, W. Du, J. Margetis, Y. Zhou, A. Mosleh, S. Al-Kabi, A. Nazzal, G. Sun, R. A. Soref, J. Tolle, B. Li, and H. A. Naseem, "Si based GeSn light emitter: mid-infrared devices in Si photonics," in *Silicon Photonics X*, feb 2015, p. 93670R. [Online]. Available: https://doi.org/10.1117/12.2077778

[79] C. Chang, T.-W. Chang, H. Li, H. H. Cheng, R. Soref, G. Sun, and J. R. Hendrickson, "Room-temperature 2- μm GeSn P-I-N homojunction light-emitting diode for inplane

coupling to group-IV waveguides," *Applied Physics Letters*, vol. 111, no. 14, p. 141105, oct 2017. [Online]. Available: http://aip.scitation.org/doi/10.1063/1.4999395

[80] D. Stange, N. von den Driesch, D. Rainko, C. Schulte-Braucks, S. Wirths, G. Mussler, A. T. Tiedemann, T. Stoica, J. M. Hartmann, Z. Ikonic, S. Mantl, D. Grützmacher, and D. Buca, "Study of GeSn based heterostructures: towards optimized group IV MQW LEDs," *Optics Express*, vol. 24, no. 2, p. 1358, 2016. [Online]. Available: https://doi.org/10.1364/OE.24.001358

[81] N. von den Driesch, D. Stange, S. Wirths, D. Rainko, I. Povstugar, A. Savenko, U. Breuer, R. Geiger, H. Sigg, Z. Ikonic, J. M. Hartmann, D. Grützmacher, S. Mantl, and D. Buca, "SiGeSn Ternaries for Efficient Group IV Heterostructure Light Emitters," *Small*, vol. 13, no. 16, p. 1603321, 2017. [Online]. Available: http://doi.wiley.com/10.1002/smll.201603321

[82] D. Stange, N. von den Driesch, D. Rainko, S. Roesgaard, I. Povstugar, J.-M. Hartmann, T. Stoica, Z. Ikonic, S. Mantl, D. Grützmacher, and D. Buca, "Short-wave infrared LEDs from GeSn/SiGeSn multiple quantum wells," *Optica*, vol. 4, no. 2, p. 185, feb 2017. [Online]. Available: https://doi.org/10.1364/OPTICA.4.000185

[83] D. Yuan, "Germanium-tin infrared photodetectors: Device design, process development, and technology demonstration," Ph.D. dissertation, National University of Singapore, 2016.

[84] J. Mathews, R. Roucka, J. Xie, S.-Q. Yu, J. Menéndéz, and J. Kouvetakis, "Extended performance GeSn/Si(100) p-i-n photodetectors for full spectral range telecommunication applications," *Applied Physics Letters*, vol. 95, no. 13, p. 133506, sep 2009. [Online]. Available: http://aip.scitation.org/doi/10.1063/1.3238327

[85] J. Mathews, R. Roucka, C. Weng, R. Beeler, J. Tolle, J. Menéndéz, and J. Kouvetakis, "Near IR Photodiodes with Tunable Absorption Edge Based on Ge," in *ECS Transactions*, 2010, pp. 765–773. [Online]. Available: https://doi.org/10.1149/1.3487607

[86] A. Gassenq, F. Gencarelli, J. Van Campenhout, Y. Shimura, R. Loo, G. Narcy, B. Vincent, and G. Roelkens, "GeSn/Ge heterostructure short-wave infrared photodetectors on silicon," *Optics Express*, vol. 20, no. 25, p. 27297, dec 2012. [Online]. Available: https://doi.org/10.1364/OE.20.027297

[87] B. R. Conley, J. Margetis, W. Du, H. Tran, A. Mosleh, S. A. Ghetmiri, J. Tolle, G. Sun, R. Soref, B. Li, H. A. Naseem, and S.-Q. Yu, "Si based GeSn photoconductors with a 1.63 A/W peak responsivity and a 2.4 μm long-wavelength cutoff," *Applied Physics Letters*, vol. 105, no. 22, p. 221117, dec 2014. [Online]. Available: https://doi.org/10.1063/1.4903540

[88] T. Pham, W. Du, B. Conley, J. Margetis, G. Sun, R. Soref, J. Tolle, B. Li, and S.-Q. Yu, "Si-based GeSn photodetector with peak responsivity of 2.85 A/W and longwave cutoff at 2.4 μm," *Electronics Letters*, vol. 51, no. 11, pp. 854–856, may 2015. [Online]. Available: https://doi.org/10.1049/el.2015.0331

[89] T. Pham, W. Du, H. Tran, J. Margetis, J. Tolle, G. Sun, R. A. Soref, H. A. Naseem, B. Li, and S.-Q. Yu, "Systematic study of Si-based GeSn photodiodes with 2.6 μm detector cutoff for short-wave infrared detection," *Optics Express*, vol. 24, no. 5, p. 4519, mar 2016. [Online]. Available: https://doi.org/10.1364/OE.24.004519

[90] Y. Dong, W. Wang, S. Xu, D. Lei, X. Gong, X. Guo, H. Wang, S.-Y. Lee, W.-K. Loke, S.-F. Yoon, and Y.-C. Yeo, "Two-micron-wavelength germanium-tin photodiodes with low dark current and gigahertz bandwidth," *Optics Express*, vol. 25, no. 14, p. 15818, 2017. [Online]. Available: https://doi.org/10.1364/OE.25.015818

[91] H. Tran, T. Pham, W. Du, Y. Zhang, P. C. Grant, J. M. Grant, G. Sun, R. A. Soref, J. Margetis, J. Tolle, B. Li, M. Mortazavi, and S.-Q. Yu, "High performance GeSn photodiodes for low-cost shortwave infrared imaging," *Journal of Applied Physics*, vol. 124, no. 1, p. 013101, jul 2018. [Online]. Available: https://doi.org/10.1063/1.5020510

[92] D. E. Aspnes and A. A. Studna, "Dielectric functions and optical parameters of Si, Ge, GaP, GaAs, GaSb, InP, InAs, and InSb from 1.5 to 6.0 eV," *Physical Review B*, vol. 27, no. 2, pp. 985–1009, 1983. [Online]. Available: https://doi.org/10.1103/PhysRevB.27.985

[93] H. Tran, W. Du, S. A. Ghetmiri, A. Mosleh, G. Sun, R. A. Soref, J. Margetis, J. Tolle, B. Li, H. A. Naseem, and S.-Q. Yu, "Systematic study of GeSn absorption coefficient and refractive index for the device applications of Si-based optoelectronics," *Journal of Applied Physics*, vol. 119, no. 10, p. 103106, 2016. [Online]. Available: https://doi.org/10.1063/1.4943652

[94] B. E. Saleh and M. C. Teich, *Fundamentals of Photonics*, 2nd ed. Wiley, 2007.

[95] G. Olsen, "Low-leakage, high-efficiency, reliable VPE InGaAs 1.0-1.7 μm photodiodes," *IEEE Electron Device Letters*, vol. 2, no. 9, pp. 217–219, sep 1981. [Online]. Available: https://doi.org/10.1109/EDL.1981.25409

[96] Y. Dong, W. Wang, D. Lei, X. Gong, Q. Zhou, S. Y. Lee, W. K. Loke, S.-F. Yoon, E. S. Tok, G. Liang, and Y.-C. Yeo, "Suppression of dark current in germanium-tin on silicon p-i-n photodiode by a silicon surface passivation technique," *Optics Express*, vol. 23, no. 14, p. 18611, jul 2015. [Online]. Available: https://doi.org/10.1364/OE.23.018611

[97] S. Biswas, J. Doherty, D. Saladukha, Q. Ramasse, D. Majumdar, M. Upmanyu, A. Singha, T. Ochalski, M. A. Morris, and J. D. Holmes, "Non-equilibrium induction of tin in germanium: towards direct bandgap GeSn nanowires," *Nature Communications*, vol. 7, no. 7, p. 11405, apr 2016. [Online]. Available: https://doi.org/10.1038/ncomms11405

[98] S. Assali, A. Dijkstra, A. Li, S. Koelling, M. A. Verheijen, L. Gagliano, N. von den Driesch, D. Buca, P. M. Koenraad, J. E. M. Haverkort, and E. P. A. M. Bakkers, "Growth and Optical Properties of Direct Band Gap Ge/GeSn Core/Shell Nanowire Arrays," *Nano Letters*, vol. 17, no. 3, pp. 1538–1544, mar 2017. [Online]. Available: https://doi.org/10.1021/acs.nanolett.6b04627

[99] T. Haffner, M. Zeghouane, F. Bassani, P. Gentile, A. Gassenq, F. Chouchane, N. Pauc, E. Martinez, E. Robin, S. David, T. Baron, and B. Salem, "Growth of GeSn Nanowires by Chemical Vapor Deposition via Vapor-Liquid-Solid Mechanism Using GeH 4 and SnCl 4," *physica status solidi (a)*, vol. 215, no. 1, p. 1700743, jan 2018. [Online]. Available: https://doi.org/10.1002/pssa.201700743

[100] A. C. Meng, C. S. Fenrich, M. R. Braun, J. P. McVittie, A. F. Marshall, J. S. Harris, and P. C. McIntyre, "Core-Shell Germanium/Germanium-Tin Nanowires Exhibiting Room-Temperature Direct- and Indirect-Gap Photoluminescence," *Nano Letters*, vol. 16, no. 12, pp. 7521–7529, 2016. [Online]. Available: https://doi.org/10.1021/acs.nanolett.6b03316

[101] L. Cao, J. S. White, J.-S. Park, J. A. Schuller, B. M. Clemens, and M. L. Brongersma, "Engineering light absorption in semiconductor nanowire devices," *Nature Materials*, vol. 8, no. 8, pp. 643–647, aug 2009. [Online]. Available: https://doi.org/10.1038/nmat2477

[102] A. Attiaoui, S. Wirth, A.-P. Blanchard-Dionne, M. Meunier, J. M. Hartmann, D. Buca, and O. Moutanabbir, "Extreme IR absorption in group IV-SiGeSn core-shell nanowires," *Journal of Applied Physics*, vol. 123, no. 22, p. 223102, jun 2018. [Online]. Available: https://doi.org/10.1063/1.5021393

[103] A. Attiaoui, "Non-equilibrium SiGeSn group IV heterostructures and nanowires for integrated mid-infrared photonics (MSc thesis)," p. 135, 2018.

[104] L. Cao, P. Fan, A. P. Vasudev, J. S. White, Z. Yu, W. Cai, J. A. Schuller, S. Fan, and M. L. Brongersma, "Semiconductor Nanowire Optical Antenna Solar Absorbers," *Nano Letters*, vol. 10, no. 2, pp. 439–445, feb 2010. [Online]. Available: https://doi.org/10.1021/nl9036627

[105] M. Albani, S. Assali, M. A. Verheijen, S. Koelling, R. Bergamaschini, F. Pezzoli, E. P. A. M. Bakkers, and L. Miglio, "Critical strain for Sn incorporation into spontaneously graded Ge/GeSn core/shell nanowires," *Nanoscale*, vol. 10, no. 15, pp. 7250–7256, 2018. [Online]. Available: https://doi.org/10.1039/C7NR09568F

[106] D. van Dam, N. J. J. van Hoof, Y. Cui, P. J. van Veldhoven, E. P. A. M. Bakkers, J. Gómez Rivas, and J. E. M. Haverkort, "High-Efficiency Nanowire Solar Cells with Omnidirectionally Enhanced Absorption Due to Self-Aligned Indium-Tin-Oxide Mie Scatterers," *ACS Nano*, vol. 10, no. 12, pp. 11 414–11 419, dec 2016. [Online]. Available: https://doi.org/10.1021/acsnano.6b06874

[107] P. Y. Yu and M. Cardona, *Fundamentals of Semiconductors*, 3rd ed. Berlin, Heidelberg: Springer, 2010. [Online]. Available: https://doi.org/10.1007/978-3-642-00710-1

[108] E. Haller, "Isotopically controlled semiconductors," *Solid State Communications*, vol. 133, no. 11, pp. 693–707, mar 2005. [Online]. Available: https://doi.org/10.1016/j.ssc.2004.12.021

[109] S. Mukherjee, U. Givan, S. Senz, M. de la Mata, J. Arbiol, and O. Moutanabbir, "Reduction of Thermal Conductivity in Nanowires by Combined Engineering of Crystal Phase and Isotope Disorder," *Nano Letters*, vol. 18, no. 5, pp. 3066–3075, may 2018. [Online]. Available: https://doi.org/10.1021/acs.nanolett.8b00612

[110] S. Ganesan, A. Maradudin, and J. Oitmaa, "A lattice theory of morphic effects in crystals of the diamond structure," *Annals of Physics*, vol. 56, no. 2, pp. 556–594, feb 1970. [Online]. Available: https://doi.org/10.1016/0003-4916(70)90029-1

[111] F. Cerdeira, C. J. Buchenauer, F. H. Pollak, and M. Cardona, "Stress-Induced Shifts of First-Order Raman Frequencies of Diamond- and Zinc-Blende-Type Semiconductors," *Physical Review B*, vol. 5, no. 2, pp. 580–593, jan 1972. [Online]. Available: https://doi.org/10.1103/PhysRevB.5.580

[112] I. D. Wolf, "Micro-Raman spectroscopy to study local mechanical stress in silicon integrated circuits," *Semiconductor Science and Technology*, vol. 11, no. 2, pp. 139–154, feb 1996. [Online]. Available: https://doi.org/10.1088/0268-1242/11/2/001

[113] F. Bianco, K. Fedus, F. Enrichi, R. Pierobon, M. Cazzanelli, M. Ghulinyan, G. Pucker, and L. Pavesi, "Two-dimensional micro-Raman mapping of stress and strain distributions in strained silicon waveguides," *Semiconductor Science and Technology*, vol. 27, no. 8, p. 085009, aug 2012. [Online]. Available: https://doi.org/10.1088/0268-1242/27/8/085009

[114] A. Tarun, N. Hayazawa, H. Ishitobi, S. Kawata, M. Reiche, and O. Moutanabbir, "Mapping the "Forbidden" Transverse-Optical Phonon in Single Strained Silicon (100) Nanowire," *Nano Letters*, vol. 11, no. 11, pp. 4780–4788, nov 2011. [Online]. Available: https://doi.org/10.1021/nl202599q

[115] J. R. Sanchez-Perez, C. Boztug, F. Chen, F. F. Sudradjat, D. M. Paskiewicz, R. Jacobson, M. G. Lagally, and R. Paiella, "Direct-bandgap light-emitting germanium in tensilely strained nanomembranes," *Proceedings of the National Academy of Sciences*, vol. 108, no. 47, pp. 18 893–18 898, nov 2011. [Online]. Available: https://doi.org/10.1073/pnas.1107968108

[116] D. Nam, D. Sukhdeo, A. Roy, K. Balram, S.-L. Cheng, K. C.-Y. Huang, Z. Yuan, M. Brongersma, Y. Nishi, D. Miller, and K. Saraswat, "Strained germanium thin film membrane on silicon substrate for optoelectronics," *Optics Express*, vol. 19, no. 27, p. 25866, dec 2011. [Online]. Available: https://doi.org/10.1364/OE.19.025866

[117] D. Jung, J. Faucher, S. Mukherjee, A. Akey, D. J. Ironside, M. Cabral, X. Sang, J. Lebeau, S. R. Bank, T. Buonassisi, O. Moutanabbir, and M. L. Lee, "Highly tensile-strained Ge/InAlAs nanocomposites," *Nature Communications*, vol. 8, p. 14204, jan 2017. [Online]. Available: http://www.nature.com/doifinder/10.1038/ncomms14204

[118] H. Chen, Y. K. Li, C. S. Peng, H. F. Liu, Y. L. Liu, Q. Huang, J. M. Zhou, and Q.-K. Xue, "Crosshatching on a SiGe film grown on a Si(001) substrate studied by Raman mapping and atomic force microscopy," *Physical Review B*, vol. 65, no. 23, p. 233303, may 2002. [Online]. Available: https://doi.org/10.1103/PhysRevB.65.233303

[119] O. Pagès, J. Souhabi, V. J. B. Torres, A. V. Postnikov, and K. C. Rustagi, "Re-examination of the SiGe Raman spectra: Percolation/one-dimensional-cluster scheme and ab initio calculations," *Physical Review B*, vol. 86, no. 4, p. 045201, jul 2012. [Online]. Available: https://doi.org/10.1103/PhysRevB.86.045201

[120] M. Mermoux, A. Crisci, F. Baillet, V. Destefanis, D. Rouchon, A. M. Papon, and J. M. Hartmann, "Strain in epitaxial Si/SiGe graded buffer structures grown on Si(100), Si(110), and Si(111) optically evaluated by polarized Raman spectroscopy and imaging," *Journal of Applied Physics*, vol. 107, no. 1, p. 013512, jan 2010. [Online]. Available: http://aip.scitation.org/doi/10.1063/1.3272824

[121] T. A. Langdo, M. T. Currie, A. Lochtefeld, R. Hammond, J. A. Carlin, M. Erdtmann, G. Braithwaite, V. K. Yang, C. J. Vineis, H. Badawi, and M. T. Bulsara, "SiGe-free strained Si on insulator by wafer bonding and layer transfer," *Applied Physics Letters*, vol. 82, no. 24, pp. 4256–4258, jun 2003. [Online]. Available: http://aip.scitation.org/doi/10.1063/1.1581371

[122] C. Chang, H. Li, T.-P. Chen, W.-K. Tseng, H. Cheng, C.-T. Ko, C.-Y. Hsieh, M.-J. Chen, and G. Sun, "The strain dependence of GeSn (x=0.083) Raman shift," *Thin Solid Films*, vol. 593, pp. 40–43, oct 2015. [Online]. Available: https://doi.org/10.1016/j.tsf.2015.09.040

[123] R. R. Lieten, C. Fleischmann, S. Peters, N. M. Santos, L. M. Amorim, Y. Shimura, N. Uchida, T. Maeda, S. Nikitenko, T. Conard, J.-P. Locquet, K. Temst, and A. Vantomme, "Structural and Optical Properties of Amorphous and Crystalline GeSn Layers on Si," *ECS Journal of Solid State Science and Technology*, vol. 3, no. 12, pp. P403–P408, oct 2014. [Online]. Available: https://doi.org/10.1149/2.0091412jss

[124] H. Lin, R. Chen, Y. Huo, T. I. Kamins, and J. S. Harris, "Raman study of strained GeSn alloys," *Applied Physics Letters*, vol. 98, no. 26, p. 261917, jun 2011. [Online]. Available: http://aip.scitation.org/doi/10.1063/1.3606384

[125] S. Bagchi, C. D. Poweleit, R. T. Beeler, J. Kouvetakis, and J. Menéndez, "Temperature dependance of the Raman spectrum in GeSn and GeSiSn alloys," *Physical Review B*, vol. 84, no. 19, p. 193201, nov 2011. [Online]. Available: https://link.aps.org/doi/10.1103/PhysRevB.84.193201

[126] R. Cheng, W. Wang, X. Gong, L. Sun, P. Guo, H. Hu, Z. Shen, G. Han, and Y.-C. Yeo, "Relaxed and Strained Patterned Germanium-Tin Structures: A Raman

Scattering Study," *ECS Journal of Solid State Science and Technology*, vol. 2, no. 4, pp. P138–P145, jan 2013. [Online]. Available: https://doi.org/10.1149/2.013304jss

[127] S. Su, W. Wang, B. Cheng, W. Hu, G. Zhang, C. Xue, Y. Zuo, and Q. Wang, "The contributions of composition and strain to the phonon shift in alloys," *Solid State Communications*, vol. 151, no. 8, pp. 647–650, apr 2011. [Online]. Available: https://doi.org/10.1016/j.ssc.2011.01.017

[128] D. Lei, K. H. Lee, S. Bao, W. Wang, B. Wang, X. Gong, C. S. Tan, and Y.-C. Yeo, "GeSn-on-insulator substrate formed by direct wafer bonding," *Applied Physics Letters*, vol. 109, no. 2, p. 022106, jul 2016. [Online]. Available: http://aip.scitation.org/doi/10.1063/1.4958844

[129] J. K. Dash, L. Chen, T.-M. Lu, G.-C. Wang, L. H. Zhang, and K. Kisslinger, "Metal-enhanced GeSn alloy film growth on glass substrates using a biaxial CaF 2 buffer layer," *CrystEngComm*, vol. 16, no. 37, pp. 8794–8804, 2014. [Online]. Available: https://doi.org/10.1039/C4CE01228C

[130] M. Oehme, D. Buca, K. Kostecki, S. Wirths, B. Holländer, E. Kasper, and J. Schulze, "Epitaxial growth of highly compressively strained GeSn alloys up to 12.5% Sn," *Journal of Crystal Growth*, vol. 384, pp. 71–76, dec 2013. [Online]. Available: https://doi.org/10.1016/j.jcrysgro.2013.09.018

[131] M. Bauer, C. Ritter, P. A. Crozier, J. Ren, J. Menendez, G. Wolf, and J. Kouvetakis, "Synthesis of ternary SiGeSn semiconductors on Si(100) via SnGe buffer layers," *Applied Physics Letters*, vol. 83, no. 11, pp. 2163–2165, sep 2003. [Online]. Available: http://aip.scitation.org/doi/10.1063/1.1606104

[132] V. R. D'Costa, J. Tolle, C. D. Poweleit, J. Kouvetakis, and J. Menéndez, "Compositional dependance of Raman frequencies in ternary GeSiSn alloys," *Physical Review B*, vol. 76, no. 3, p. 035211, jul 2007. [Online]. Available: https://doi.org/10.1103/PhysRevB.76.035211

[133] J. Xie, A. V. G. Chizmeshya, J. Tolle, V. R. D'Costa, J. Menendez, and J. Kouvetakis, "Synthesis, Stability Range, and Fundamental Properties of Si-Ge-Sn Semiconductors Grown Directly on Si(100) and Ge(100) Platforms," *Chemistry of Materials*, vol. 22, no. 12, pp. 3779–3789, jun 2010. [Online]. Available: https://doi.org/10.1021/cm100915q

[134] J.-H. Fournier-Lupien, S. Mukherjee, S. Wirths, E. Pippel, N. Hayazawa, G. Mussler, J. M. Hartmann, P. Desjardins, D. Buca, and O. Moutanabbir, "Strain and composition effects on Raman vibrational modes of silicon-germanium-tin ternary alloys," *Applied Physics Letters*, vol. 103, no. 26, p. 263103, dec 2013. [Online]. Available: http://aip.scitation.org/doi/10.1063/1.4855436

[135] M. A. Renucci, J. B. Renucci, R. Zeyher, and M. Cardona, "Second-order Raman scattering in germanium in the vinicity of the E1, E1+Delta1 edges," *Physical Review B*, vol. 10, no. 10, pp. 4309–4323, nov 1974. [Online]. Available: https://doi.org/10.1103/PhysRevB.10.4309

[136] S. Larouche and L. Martinu, "OpenFilters: open-source software for the design, optimization, and synthesis of optical filters," *Applied Optics*, vol. 47, no. 13, p. C219, 2008. [Online]. Available: https://doi.org/10.1364/AO.47.00C219

[137] H. A. Macleod, *Thin-Film Optical Filters*, 3rd ed. CRC Press, 2010.

[138] J. B. Schneider, "Understanding the Finite-Difference Time-Domain Method," p. 403, 2017.

[139] S. Johnson, "Notes on perfectly matched layers (PMLs)," pp. 1–18, 2008. [Online]. Available: http://www-math.mit.edu/~stevenj/18.369/spring09/pml.pdf

[140] B. Liang, M. Bai, H. Ma, N. Ou, and J. Miao, "Wideband Analysis of Periodic Structures at Oblique Incidence by Material Independent FDTD Algorithm," *IEEE Transactions on Antennas and Propagation*, vol. 62, no. 1, pp. 354–360, jan 2014. [Online]. Available: https://doi.org/10.1109/TAP.2013.2287896

[141] Lumerical, "Knowledge Base." [Online]. Available: https://kb.lumerical.com/layout_analysis_pabs_simple.html

[142] M. J. Madou, *Fundamentals of microfabrication: the science of miniaturization.* CRC Press, 2002.

[143] S. A. Ghetmiri, "Si-based Germanium-Tin (GeSn) Emitters for Short-Wave Infrared Optoelectronics," Ph.D. dissertation, University of Arkansas, Fayetteville, 2016.

[144] Y. Dong, B. L. Ong, W. Wang, Z. Zhang, J. Pan, X. Gong, E. S. Tok, G. Liang, and Y. C. Yeo, "Etching of germanium-tin using ammonia peroxide mixture," *Journal of Applied Physics*, vol. 118, no. 24, pp. 0–8, 2015. [Online]. Available: https://doi.org/10.1063/1.4938476

[145] Y. Dong, D. Lei, X. Xu, W. Wang, and Y. C. Yeo, "Chlorine- and fluorine-based dry etching of Germanium-Tin," *7th International Silicon-Germanium Technology and Device Meeting (ISTDM)*, pp. 99–100, 2014. [Online]. Available: https://doi.org/10.1109/ISTDM.2014.6874686

[146] H. G. Tompkins and E. A. Irene, *Handybook of Ellipsometry*, 2005.

[147] "Germanium (Ge) phonon dispersion relations, density of states," in *Group IV Elements, IV-IV and III-V Compounds. Part a - Lattice Properties*, ser. Landolt-Börnstein - Group III Condensed Matter, O. Madelung, U. Rössler, and M. Schulz, Eds. Berlin/Heidelberg: Springer-Verlag, 2001, vol. 41A1a, pp. 1–19. [Online]. Available: https://doi.org/10.1007/10551045_226

[148] J.-J. Rousseau and A. Gibaud, *Cristallographie géométrique et radiocristallographie*, 3rd ed. Paris: Dunod, 2007.

[149] A. Gassenq, L. Milord, J. Aubin, K. Guilloy, S. Tardif, N. Pauc, J. Rothman, A. Chelnokov, J. M. Hartmann, V. Reboud, and V. Calvo, "Gamma bandgap determination in pseudomorphic GeSn layers grown on Ge with up to 15% Sn content," *Applied Physics Letters*, vol. 109, no. 24, pp. 0–5, 2016. [Online]. Available: https://doi.org/10.1063/1.4971397

[150] V. Reboud, A. Gassenq, N. Pauc, J. Aubin, L. Milord, Q. M. Thai, M. Bertrand, K. Guilloy, D. Rouchon, J. Rothman, T. Zabel, F. Armand Pilon, H. Sigg, A. Chelnokov, J. M. Hartmann, and V. Calvo, "Optically pumped GeSn micro-disks with 16% Sn lasing at 3.1 μm up to 180 K," *Applied Physics Letters*, vol. 111, no. 9, p. 092101, aug 2017. [Online]. Available: https://doi.org/10.1063/1.5000353

[151] M. Fukuda, K. Watanabe, M. Sakashita, M. Kurosawa, O. Nakatsuka, and S. Zaima, "Control of GeSiSn layer lattice constant for energy band alignment in GeSn/GeSiSn heterostructures," *Semiconductor Science and Technology*, vol. 32, no. 10, p. 104008, oct 2017. [Online]. Available: https://doi.org/10.1088/1361-6641/aa80ce

[152] N. S. Fernando, R. A. Carrasco, R. Hickey, J. Hart, R. Hazbun, S. Schoeche, J. N. Hilfiker, J. Kolodzey, and S. Zollner, "Band gap and strain engineering of pseudomorphic GeSiSn alloys on Ge and GaAs for photonic applications," *Journal of Vacuum Science & Technology B, Nanotechnology and Microelectronics: Materials, Processing, Measurement, and Phenomena*, vol. 36, no. 2, p. 021202, mar 2018. [Online]. Available: https://doi.org/10.1116/1.5001948

[153] J. Margetis, A. Mosleh, S. Al-Kabi, S. Ghetmiri, W. Du, W. Dou, M. Benamara, B. Li, M. Mortazavi, H. Naseem, S.-Q. Yu, and J. Tolle, "Study of low-defect and strain-relaxed GeSn growth via reduced pressure CVD in H2 and N2 carrier gas," *Journal of Crystal Growth*, vol. 463, pp. 128–133, 2017. [Online]. Available: https://doi.org/10.1016/j.jcrysgro.2017.01.041

[154] G. Martínez-Criado, R. Tucoulou, P. Cloetens, P. Bleuet, S. Bohic, J. Cauzid, I. Kieffer, E. Kosior, S. Labouré, S. Petitgirard, A. Rack, J. A. Sans, J. Segura-Ruiz, H. Suhonen, J. Susini, and J. Villanova, "Status of the hard X-ray microprobe beamline ID22 of the European Synchrotron Radiation Facility," *Journal of Synchrotron Radiation*, vol. 19, no. 1, pp. 10–18, jan 2012. [Online]. Available: https://doi.org/10.1107/S090904951104249X

[155] S. F. Li, M. R. Bauer, J. Menéndez, and J. Kouvetakis, "Scaling law for the compositional dependence of Raman frequencies in SnGe and GeSi alloys," *Applied Physics Letters*, vol. 84, no. 6, pp. 867–869, feb 2004. [Online]. Available: http://aip.scitation.org/doi/10.1063/1.1645667

[156] P. Parayanthal and F. H. Pollak, "Raman Scattering in Alloy Semiconductors: "Spatial Correlation" Model," *Physical Review Letters*, vol. 52, no. 20, pp. 1822–1825, may 1984. [Online]. Available: https://doi.org/10.1103/PhysRevLett.52.1822

[157] D. J. Lockwood and Z. R. Wasilewski, "Optical phonons in AlGaAs: Raman spectroscopy," *Physical Review B*, vol. 70, no. 15, p. 155202, oct 2004. [Online]. Available: https://doi.org/10.1103/PhysRevB.70.155202

[158] S. Bagchi, "Raman Spectroscopy Characterization of Anharmonicity and Alloying Effects in Semiconductor Materials," Ph.D. dissertation, Arizona State University, Tempe, 2011.

[159] R. Schorer, "Raman scattering of α-Sn/Ge superlattices on Ge (001)," *Journal of Vacuum Science & Technology B: Microelectronics and Nanometer Structures*, vol. 11, no. 3, p. 1069, may 1993. [Online]. Available: https://doi.org/10.1116/1.587009

[160] B. A. Weinstein and M. Cardona, "Second-Order Raman Spectrum of Germanium," *Physical Review B*, vol. 7, no. 6, pp. 2545–2551, mar 1973. [Online]. Available: https://doi.org/10.1103/PhysRevB.7.2545

[161] H. D. Fuchs, C. H. Grein, C. Thomsen, M. Cardona, W. L. Hansen, E. E. Haller, and K. Itoh, "Comparison of the phonon spectra of 70Ge and natural Ge crystals: Effects

of isotopic disorder," *Physical Review B*, vol. 43, no. 6, pp. 4835–4842, feb 1991. [Online]. Available: https://doi.org/10.1103/PhysRevB.43.4835

[162] C. J. Buchenauer, M. Cardona, and F. H. Pollak, "Raman Scattering in Gray Tin," *Physical Review B*, vol. 3, pp. 1243–1244, feb 1971. [Online]. Available: https://doi.org/10.1103/PhysRevB.3.1243

[163] J. Menéndez and H. Höchst, "Study of the phase transition in heteroepitaxially grown films of α-Sn by Raman spectroscopy," *Thin Solid Films*, vol. 111, no. 4, pp. 375–379, jan 1984. [Online]. Available: https://doi.org/10.1016/0040-6090(84)90329-8

[164] G. Nelin and G. Nilsson, "Phonon Density of States in Germanium at 80 K Measured by Neutron Spectrometry," *Physical Review B*, vol. 5, no. 8, pp. 3151–3160, apr 1972. [Online]. Available: https://doi.org/10.1103/PhysRevB.5.3151

[165] J. Oh, H. C. Yuan, and H. M. Branz, "An 18.2%-efficient black-silicon solar cell achieved through control of carrier recombination in nanostructures," *Nature Nanotechnology*, vol. 7, no. 11, pp. 743–748, 2012. [Online]. Available: https://doi.org/10.1038/nnano.2012.166

[166] Z.-P. Yang, L. Ci, J. A. Bur, S.-Y. Lin, and P. M. Ajayan, "Experimental Observation of an Extremely Dark Material Made By a Low-Density Nanotube Array," *Nano Letters*, vol. 8, no. 2, pp. 446–451, feb 2008. [Online]. Available: https://doi.org/10.1021/nl072369t

[167] S. L. Diedenhofen, R. E. Algra, E. P. A. M. Bakkers, and J. Gómez Rivas, "Mimicking moth's eyes for photovoltaic applications with tapered GaP nanorods," in *Next Generation (Nano) Photonic and Cell Technologies for Solar Energy Conversion*, aug 2010, p. 77720M. [Online]. Available: https://doi.org/10.1117/12.862518

[168] E. D. Palik, Ed., *Handbook of Optical Constants of Solids*. Elsevier Inc., 1997.

[169] K. Tomioka, T. Tanaka, S. Hara, K. Hiruma, and T. Fukui, "III-V Nanowires on Si Substrate: Selective-Area Growth and Device Applications," *IEEE Journal of Selected Topics in Quantum Electronics*, vol. 17, no. 4, pp. 1112–1129, jul 2011. [Online]. Available: https://doi.org/10.1109/JSTQE.2010.2068280

[170] Y. Cui, J. Wang, S. R. Plissard, A. Cavalli, T. T. T. Vu, R. P. J. van Veldhoven, L. Gao, M. Trainor, M. A. Verheijen, J. E. M. Haverkort, and E. P. A. M. Bakkers, "Efficiency Enhancement of InP Nanowire Solar Cells by Surface

Cleaning," *Nano Letters*, vol. 13, no. 9, pp. 4113–4117, sep 2013. [Online]. Available: https://doi.org/10.1021/nl4016182

[171] S. Assali, A. Attiaoui, S. Mukherjee, J. Nicolas, and O. Moutanabbir, "TEOS layers for low temperature processing of group IV optoelectronic devices," *Journal of Vacuum Science & Technology B*, vol. 36, no. 6, p. 061204, nov 2018. [Online]. Available: http://avs.scitation.org/doi/10.1116/1.5047909

[172] T. K. N. Nguyen, A. Renaud, M. Wilmet, N. Dumait, S. Paofai, B. Dierre, W. Chen, N. Ohashi, S. Cordier, F. Grasset, and T. Uchikoshi, "New ultra-violet and near-infrared blocking filters for energy saving applications: fabrication of tantalum metal atom cluster-based nanocomposite thin films by electrophoretic deposition," *J. Mater. Chem. C*, vol. 5, no. 40, pp. 10 477–10 484, 2017. [Online]. Available: https://doi.org/10.1039/c7tc02454a

[173] C. Lin and M. L. Povinelli, "Optimal design of aperiodic, vertical silicon nanowire structures for photovoltaics," *Optics Express*, vol. 19, no. S5, p. A1148, sep 2011. [Online]. Available: https://doi.org/10.1364/OE.19.0A1148

[174] A. Ramier, *Intégration de guides d'onde et microrésonateurs à modes de galerie par assemblage à puce retournée (MSc thesis)*. Polytechnique Montréal, 2014. [Online]. Available: https://publications.polymtl.ca/1489/

APPENDIX A LIST OF CONTRIBUTIONS

Journal publication

É. Bouthillier, S. Assali, J. Nicolas, and O. Moutanabbir. (2019). Decoupling the effects of composition and strain on GeSn Raman vibrational modes (*submitted*).

Oral presentations

É. Bouthillier, S. Assali, J. Nicolas, and O. Moutanabbir. "Decoupling Strain and Composition Effects on GeSn Lattice Vibrations" at Americas International Meeting on Electrochemistry and Solid State Science (AiMES 2018), Cancún, Mexico, October 4$^{\text{th}}$ 2018.

É. Bouthillier, S. Assali, A. Attiaoui, S. Martí-Sánchez, J. Arbiol, and O. Moutanabbir. "Light Absorption Engineering in GeSn Nanowires" at ISTDM/ICSI 2018, Potsdam, Allemagne, May 28$^{\text{th}}$ 2018.

Poster presentation

É. Bouthillier, S. Assali, A. Attiaoui, and O. Moutanabbir. "Light Absorption Engineering in GeSn Nanowires" at Nanowire Week 2018, Hamilton (ON), Canada, June 14$^{\text{th}}$ 2018.

Additional journal publications (not part of this work)

M. Fortin-Deschênes, R. M. Jacobberger, C.-A. Deslauriers, O. Waller, É. Bouthillier, M. S. Arnold, and O. Moutanabbir. (2019). Dynamics of Antimonene-Graphene Van Der Waals Growth. Advanced Materials, 1900569. `https://doi.org/10.1002/adma.201900569`

S. Mukherjee, N. Nateghi, R. M. Jacobberger, É. Bouthillier, M. de la Mata, J. Arbiol, T. Coenen, D. Cardinal, P. Levesque, P. Desjardins, R. Martel, M. S. Arnold, and O. Moutanabbir. (2018). Growth and Luminescence of Polytypic InP on Epitaxial Graphene. Advanced Functional Materials, 28, 1705592. `https://doi.org/10.1002/adfm.201705592`